DEVELOPING METHODOLOGIES TO EXPLORE NEUROVASCULAR COUPLING ON A MICRON SCALE

Lindsay Reine Walton

A dissertation submitted to the faculty at the University of North Carolina at Chapel Hill in partial fulfillment of the requirements for the degree of Doctor of Philosophy in the Department of Chemistry.

Chapel Hill
2016

Approved by:

R. Mark Wightman

James Jorgenson

Royce Murray

Garret Stuber

Anne Taylor

ABSTRACT

Lindsay Reine Walton: Developing Methodologies to Explore Neurovascular Coupling on a Micron Scale
(Under the direction of R. Mark Wightman)

During brain activity, local oxygen and glucose is consumed and cerebral blood flow (CBF) increases in a process known as functional hyperemia or neurovascular coupling. Neurotransmission releases molecules that respond through post-synaptic neurons, astrocytes, and cerebral blood vessels to stringently regulate CBF supply according to local demand. If coupling between metabolic supply and demand is not met, energy deficits can lead to toxin accumulation, pathology, and even cell death. Functional magnetic resonance imaging (fMRI) is a popular method used to monitor neurovascular regulation and study brain functionality. However, recent studies show that the neurovascular heterogeneity can produce decoupled hyperemia at high spatial resolutions in healthy subjects, making interpreting fMRI data less certain and necessitating a better understanding of the underlying mechanisms behind neurovascular coupling.

Here, we developed additional tools with which to probe neurovascular coupling at highly localized environments. We adapted an existing CBF measuring technique to a microfabricated format and proved its functionality through mathematical modeling and *in vitro* verification. Next, we adapted a multimodal sensor to detect oxygen changes and neuronal activity resultant of local, chemically selective glutamate stimulation using iontophoresis. Comparing glutamate iontophoresis to electrically stimulated glutamate release revealed key differences between the local cerebrovascular responses to stimuli of different specificities and intensities. We extended the multimodal sensor to modulate local glutamatergic receptor pharmacology and discovered

that glutamate exerts influence on neurovascular coupling differentially between the somatosensory cortex and the nucleus accumbens.

These tools provide alternative ways to measure multiple physiological metrics related to neurovascular coupling simultaneously. Our multimodal sensors offer chemical and spatial selectivity, and can assess neurovascular changes throughout the brain with minimal invasiveness. Together, our work demonstrates the importance of considering brain heterogeneity at the local level in the interpretation of more broad brain functionality studies.

ACKNOWLEDGEMENTS

I would like to acknowledge and thank the persons that made this work possible, both professionally and personally. Firstly, I would first like to thank my thesis advisor Dr. R. Mark Wightman for his guidance, mentorship, and, strangely enough, recommendations for several great movies and television shows. I am grateful for the number of research opportunities and project ideas that he allowed me to pursue, and even more grateful for the tactful way that he curbed my enthusiasm to vastly more realistic levels.

A number of other academic professionals deserve thanks as well. My undergraduate advisor Dr. John Gilje taught me to set high goals, but also to accept that “oopsie-daisies” are a natural part of achieving those goals. I would like to thank my other undergraduate advisor Dr. Donna Amenta for keeping me humble and being a model woman scientist, bold and brassy. At UNC, my first laboratory mentor was Dr. Martin Edwards, who with endless patience taught me both the programming and maths behind Chapter 2, and to always be suspicious about data that looks “nice.” Dr. Susan Carroll and Nick Boustead contributed months of time and energy into Chapters 4 and 5. My labmate Doug Kirkpatrick made sense of iontophoresis behind the scenes and helped in experimental design. I cannot thank Collin McKinney and Matthew Verber enough for providing the technology used in every project, as well as their advice and frequent troubleshooting. Finally, I would like to acknowledge Dr. Greg McCarty of NC State University for his mentorship, ideas, and labor for both Chapters 2 and 3.

Additionally, I am indebted to a plethora of persons for their contributions to my sanity and growth as a scientific researcher. Thanks to Anna for leading me to choose UNC and her, Beth, Elyse, and Meg for introducing me to *in vivo* experiments with minimal emotional scarring.

I am especially indebted to Meg for running me through the writing-a-biological-journal-article gauntlet while simultaneously cheering me on. To my labmates Susan and Caddy, thank you for the endless baked goods and hilarious conversations. Justin and Nathan, thank you for providing the Wightman lab with your angelic singing voices. Thanks to Nick the "'Trode Master" for being an awesome undergrad and making me feel old on a regular basis. Thanks to Adam for teaching me the art of, "What Not to Do in a Cleanroom." I appreciate both his and Josh's company as fellow microfab bunnies. I feel extremely fortunate to have been part of a quirky and collaborative chemistry cohort: Steve, short Matt companion, Emilie, JB, and many others have truly enriched this experience. I miss you all. To Rob and Greg still stuck here with me, I hope it stays that way for a long time. To the entire Shih lab, I look forward to seeing you more!

Finally, there are still more people to thank outside of academia. I would like to thank my parents, brother, and sister for supporting me throughout this crazy adventure. Megan, Tori, Aimee, Na Shai, Luis, Gattuso… thanks to everyone back home for immediately picking up where we last left off during visits. Amy especially holds me accountable for Skyping and catching up, as we two introverts would otherwise never hear from each other. I would like to express my condolences to Tim and Brittany, who have dealt with near-constant science nerd banter throughout these years. Last but not least, to Billy: I underestimated how much patience one man could possess. Thank you for always believing in me, supporting me, and rescuing me from lab at ungodly hours. You have been my stable refuge throughout these tumultuous years.

TABLE OF CONTENTS

LIST OF TABLES

LIST OF FIGURES

LIST OF ABBREVIATIONS AND SYMBOLS

*	probability less than 0.05
**	probability less than 0.01
***	probability less than 0.001
****	probability less than 0.0001
°C	degrees Celsius
2D	two-dimensional
A	surface area
a	characteristic dimension
A-P	anterior-posterior
ACPD	(±)-1-aminocyclopenate-*trans*-1,3-dicarboxylic acid
Ag/AgCl	silver/silver chloride
AMPA	α-amino-3-hydroxy-5-methylisoxazole-4-propionic acid
AMPAR	AMPA receptor
ANOVA	analysis of variance
AP5	DL-2-amino-5-phosphonopentanoic acid sodium salt
ASL	arterial spin labeling
ATP	adenosine triphosphate
b	deviation function
BASS	Biomedical Analysis and Simulation Supercomputer
BBB	blood brain barrier
BOLD	blood oxygenation level dependent
C	concentration
c	normalized concentration
CBF	cerebral blood flow

CBV	cerebral blood volume
CE	collection efficiency
CHANL	Chapel Hill Analytical and Nanofabrication Laboratory
CMR_{glc}	cerebral metabolic rate of glucose
CNQX	1,2,3,4-tetrahydro-7-nitro-2,3-dioxoquinoxaline-6-carbonitrile disodium salt
D	diffusion coefficient
DC	direct current
DHK	dihydrokainic acid
D-V	dorsal-ventral
e^-	electrons
E_{app}	applied potential
e.g.	exempli gratia
EEG	electroencephalography
EHC	electrolytic hydrogen clearance
eNOS	endothelial nitric oxide synthase
F	Faraday's constant
$F_{(X,Y)}$	F-test with degrees of freedom numerator X and denominator Y
FDG	[^{18}F]fluorodeoxyglucose
fMRI	functional magnetic resonance imaging
FSCV	fast scan cyclic voltammetry
g	gram
G-G	Geisser-Greenhouse
GLT-1	glutamate transporter 1
^1H	proton
H^+	proton

H_2	molecular hydrogen
H_2O	water
H_2SO_4	sulfuric acid
HDCV	High-Definition Cyclic Voltammetry
HMDS	hexamethyldisilazane
hr	hour
Hz	hertz
i_{gen}	generator current
i_{coll}	collector current
$\tilde{I}_{coll}$	normalized collector current
I_0	clearance current without flow
i_F	clearance current with flow
i_{ss}	steady state current
i.e.	id est
iGluR	ionotropic glutamate receptor
i.p.	intraperitoneal
J	flux
K	degrees Kelvin
κ	first order exponential rate constant
k	normalized first order exponential rate constant
kg	kilogram
K_2HPO_4	dipotassium hydrogen phosphate
KCl	potassium chloride
L-ARG	N^{ω}-propyl-L-arginine hydrochloride
LDF	laser Doppler flowmetry

LFP	local field potential
ln	natural log
L-NAME	NG-nitro-L-arginine methyl ester hydrochloride
LPCVD	low-pressure chemical vapor deposition
M-L	medial-lateral
MΩ	megaohm
µm	micrometer
mm	millimeter
MEG	magnetoencephalography
mGluR	metabotropic glutamate receptor
M	molar
µM	micromolar
mM	millimolar
min	minute
ms	millisecond
MSN	medium spiny neuron
MTEP	3-[(2-methyl-1,3-thiazol-4-yl)ethynyl]pyridine hydrochloride
mV	millivolt
n	number of samples
$\underline{n}$	inward pointing unit normal
N_2	molecular nitrogen
nA	nanoamperes
NaCl	sodium chloride
NaH_2PO_4	monosodium dihydrogen phosphate
NaOH	sodium hydroxide

NAc	nucleus accumbens
NADH	nicotinamide adenine dinucleotide
NADPH	nicotinamide adenine dinucleotide phosphate
NE	DL-noradrenaline hydrochloride
NMDA	N-methyl-D-aspartic acid
NMDAR	NMDA receptor
nmol	nanomole
NNF	North Carolina State University Nanofabrication Facility
NO	nitric oxide
NOS	nitric oxide synthase
nNOS	neuronal NOS
O_2	molecular oxygen
P	probability
pA	picoamperes
PBS	phosphate buffered saline
PC	principal component
PCR	principal component regression
PECVD	plasma-enhanced chemical vapor deposition
PET	positron emission tomography
PFC	prefrontal cortex
pmol	picomole
PPF	pyrolyzed photoresist film
Pt	platinum
R^2	coefficient of determination
RF	radiofrequency

RIE	reactive ion etching
RuHex	hexaammineruthenium (III) trichloride
σ	standard deviation
s	second
SD	standard deviation
SEM	standard error of the mean
t	normalized time variable
T	time
t*	normalized pulse duration
T*	pulse duration
$t_{(2,Y)}$	two-tailed, unpaired Student's t-test with Y degrees of freedom
UNC	University of North Carolina
V	volt
Vs.	versus

CHAPTER 1: MUCH ADO ABOUT NEUROVASCULAR COUPLING

Introduction

Neurons are cells in the brain that communicate both electrically and chemically with other neurons, blood vessels, and a host of additional cell types. These signals propagate throughout the brain and periphery to accomplish tasks that range from recalling memories to kicking a ball. Neurotransmission and the upkeep of neuronal processes requires an astonishing amount of effort, consuming 20% of the body's total resting energy (Rolfe and Brown, 1997). This energy predominantly derives from oxygen and glucose, but these metabolic substrates are not stored within the brain for access during times of increased activity. This is essential for the continued ability to maintain healthy cognitive function. If neurons are deprived of metabolic fuel, they will be unable to maintain ionic gradients. This leads to extensive cellular depolarization, excitotoxic buildup of glutamate, and eventual cell death.

In 1890, scientists Roy and Sherrington published their seminal hypothesis that cerebral blood flow (CBF) renewed energy supplies to local brain regions with increased neuronal activity (Roy and Sherrington, 1890). This process was called functional hyperemia, also known also as neurovascular or cerebrovascular coupling. Since then, several breakthroughs in neurovascular coupling research have been made. Originally, CBF was proposed to respond to local decreases in oxygen or glucose in a negative feedback loop, until vasoactive species released from neurotransmission or downstream processes were found to communicate these needs (Attwell et al., 2010). Decades passed before astrocytic glial cells were found to influence vascular regulation, even forming a physical bridge between neurons and blood vessels to collectively form a "neurovascular unit" (Iadecola and Nedergaard, 2007). Astrocytic processes were found in close contact with presynaptic and postsynaptic neurons, together forming a hub

of neurovascular communication now known as the tripartite synapse (Araque et al., 1999). Even more recently, the spatial extent of neuronal activation was found to depend on stimulus intensity and revealed new insights into neurovascular decoupling at the local, cellular level (Thompson et al., 2004, O'Herron et al., 2016). However, many underlying factors of neurovascular coupling are still poorly understood.

Studying neurovascular coupling encompasses the study of neuronal and astrocytic activity, CBF, oxygen dynamics, and the rates of oxygen and glucose metabolism. Each aspect can be monitored using multiple techniques, and the spatiotemporal resolutions between techniques differ. This is important because different neurovascular environments that dictate responses at the local level can invalidate the assumption that coupling is uniform across different brain regions. In addition to differences in detection, the stimulus used to elicit a cerebrovascular response can vary from visual (e.g., viewing a moving checkerboard pattern), to tactile (e.g., tail pinch), or electrical (e.g., deep brain stimulation). Together, coalescing the disparities between the data collection techniques and stimuli used, as well as the brain region(s) explored makes it difficult to interpret the specifics of neurovascular studies. Regardless of these inherent difficulties, it is imperative that neurovascular coupling research continue to be studied so as to better understand the underlying factors behind implicated pathologies and hone in on prospective therapeutic targets.

This introduction serves to establish the importance of studying neurovascular coupling and to explain the techniques used to study this concept. First, we describe differences between healthy and pathological states of cerebrovascular decoupling. Next, we explore the main methods used to measure neurovascular coupling components at a large scale, and then their localized, spatially specific counterparts. Finally, we summarize what combinations have been performed between the differentially scaled technologies.

Neurovascular Decoupling and Pathology

For nearly a century after Roy and Sherrington first discussed functional hyperemia, it generally was accepted that healthy brains tightly coupled CBF and metabolism to neuronal activity. If this process decoupled, it was seen as an indication of pathology. These pathological neurovascular dysfunctions range in severity from a complete CBF occlusion via ischemic stroke to the far subtler cortical spreading depression indicated in migraine (Lauritzen et al., 2011). Indeed, numerous pathologies do exhibit signs of blood flow dysregulation or altered levels of metabolism. These include Alzheimer's disease and dementia, among others (Girouard and Iadecola, 2006, Attwell et al., 2010, Zlokovic, 2011).

Neurodegenerative diseases especially exhibit dysfunction in the form of impaired CBF delivery or glucose utilization, such that normal brain activity begins to run an energy deficit and accumulate harmful levels of carbon dioxide, reactive oxygen species, and other toxins (Zlokovic, 2011). Usually, vessels are protected by the blood brain barrier (BBB), a selectively permeable membrane of endothelial cells and pericytes that encompass and protect cerebral blood vessels from potentially harmful species. In addition to protecting these blood vessels, pericytes also modulate capillary diameters based on neuronal input (Peppiatt et al., 2006). Normally, these cells form tight junctions around the circumference of blood vessels that only allow passage of oxygen, carbon dioxide, and small, lipid soluble proteins into the brain parenchyma (Zlokovic, 2011). When this barrier is compromised, infectious agents may freely flow into the cerebral vasculature (Nelson et al., 2016). It is still unknown whether BBB injury is the starting point for neurodegenerative pathologies or a symptom resulting from changes elsewhere.

In addition to the importance of neurovascular regulation within the brain, it is crucial to maintain healthy vascular regulation across the entire body. Diabetes, hypertension (Iadecola and Davisson, 2008), drug use, and many other conditions have been linked to an increased risk of neurodegenerative disease, along with age and genetic factors (Zlokovic, 2011,

Daulatzai, 2016). Comorbidity between these factors brings greater risk of dysfunctional neurovascular regulation, especially late in life. However, the relationship between systemic blood regulation and cognitive functionality can be advantageous. As many drugs do not readily pass through the BBB to locally access cerebral vasculature, indirect treatments such as anti-hypertensive drugs (Hajjar et al., 2012) and even exercise (DeFina et al., 2013) have found success in ameliorating risk factors that contribute to neurodegenerative disease. The relation between systemic and cerebral circulation requires further study, necessitating the use of technology that can monitor blood flow dysregulation at both global and local resolutions.

Dichotomy between Coupled and Decoupled States in Healthy Subjects

Healthy human subjects were long assumed to couple CBF and metabolism increases with brain activity in support of the functional hyperemia dogma (Roy and Sherrington, 1890). In many cases, this is valid (Hoge et al., 1999, Uludağ et al., 2004), but technical challenges prevented anyone from proving otherwise until the advent of positron emission tomography (PET) imaging in the 1980s. Once PET paradigms were established, then CBF, cerebral blood volume (CBV) and oxygen extraction fractions (metrics comparing oxyhemoglobin conversion to deoxyhemoglobin) could be quantified using a series of three ^{15}O tracers (Mintun et al., 1984). This led to the seminal 1986 publication first describing an uncoupled neurovascular response in healthy human subjects, turning the world of functional neuroimaging on its head (Fox and Raichle, 1986). Specifically, finger pad stimulation was found to elicit regional CBF increases that far surpassed what would have been expected from the simultaneous increase in metabolism. Ever since then, researchers have been attempting to establish the rhyme and reason behind neurovascular decoupling to distinguish the neurotypical from the neuropathological.

Knowing the difference between normal and detrimental neurovascular decoupling is critical knowledge when interpreting brain functionality studies (Logothetis, 2003, Uğurbil et al., 2003). The most prolific technique used for these studies is functional magnetic resonance imaging (fMRI), which relies on the assumption that neurovascular coupling is conserved when attributing changes in blood flow or oxygen to brain activity. Without directly monitoring neuronal activity, this assumption may not be valid across brain regions with different metabolic behavior (Sloan et al., 2010). As detailed later in this chapter, to truly study functional hyperemia dynamics necessitates the use of several techniques in concert, each measuring a different change. Experimental design requires careful consideration not only of the techniques to be used, but the protocol to elicit a functional response. Advancements in technology have led to highly specific means of both stimulating and recording functional hyperemia, and we are only beginning to understand the differences behind localized and larger scale cerebral responses.

Population-Level Detection

To study neurovascular coupling is to study a simultaneous cascade of events that operate on different timescales and produce downstream effects. Unfortunately, many ways to detect the relevant metrics related to neurovascular coupling are also invasive. Thus, to ethically study neurovascular coupling in humans requires non-invasive methods. While these techniques are unable to determine specific underlying processes, they are able to collect measurements without compromising the brain tissue. Here, we briefly describe the most common techniques used to study neurovascular coupling at a large spatial scale.

Cellular Activity

Electroencephalography - Neurons fire when their ionic gradients sufficiently perturb membrane potentials towards a threshold value, past which the cell depolarizes and fires an

action potential. At a small scale, this excitatory firing temporarily establishes a charged dipole along the neuron. Electroencephalography (EEG) positions multiple electrodes across the scalp to monitor this electrical activity. Individually, these signals are too weak to detect through dura, skull, and skin. These physical barriers serve as insulation between the electrode charges and the charges accumulated through synaptic firing; effectively, this system acts as a capacitor (Jackson and Bolger, 2014). Eventually, these charges propagate through to the electrodes. EEG typically is used to diagnose pathologies that disrupt the natural oscillations of brain activity, such as epilepsy. Its spatial resolution is poor and it can neither detect subcortical brain activity nor target the source of the cortical signals that it does detect. Despite these disadvantages, the low cost, ready use with other techniques, and millisecond time resolution ensure that the technique is still widely used in both preclinical and clinical studies.

Magnetoencephalography - Magnetoencephalography (MEG) is a technique similar to EEG, but that takes advantage of the magnetic field generated from neuronal activity rather than the buildup of charge. The collective neuronal electrical currents from activity induce a weak magnetic field in accordance with Maxwell's equations. To detect these magnetic fields, which are ~10^{-9} gauss in comparison to the ~0.5 gauss exerted by the earth's magnetic field (Cohen, 1972), requires sensitive superconducting quantum interference devices to transduce magnetic signals into voltage. These sensors must be kept at 4.2 K temperatures and operate in a heavily shielded room to avoid environmental noise (Pizzella et al., 2014). Like EEG, its uses are mostly related to observing the oscillatory dynamics of brain activity at a millisecond scale to diagnose pathologies, but MEG boasts superior spatial resolution that can aid in the location of brain tumors prior to surgery (Pizzella et al., 2014).

Oxygen

BOLD fMRI – The gold standard of detecting global oxygen usage throughout the entire brain is blood oxygenation level dependent (BOLD) fMRI. This technique capitalizes on the different magnetic properties of diamagnetic oxyhemoglobin versus the paramagnetic deoxyhemoglobin to map hemodynamic responses (Ogawa et al., 1990). During a BOLD scan, radiofrequency (RF) pulses uniformly align the magnetic poles of ^{1}H nuclei (Plewes and Kucharczyk, 2012), which then relax in a predictable manner. As neuronal activity consumes energy, oxyhemoglobin becomes deoxyhemoglobin and thereby distorts these local magnetic fields (Harris et al., 2011). Greater neuronal activity presumably consumes more oxygen, resulting in a greater disturbance in the magnetic field and thus increased BOLD signals.

This technique is completely non-invasive, images the whole brain at once, and can be used to obtain as many scans per experiment as the subject allows. The spatial resolution typically is a 1-3 millimeter pixel cube, known as a voxel, and the temporal resolution is on the order of seconds (Harris et al., 2011). Studies range from monitoring the severity of a traumatic brain injury (Belanger et al., 2007) to tracking the effects of a psychotic stimulant (Carhart-Harris et al., 2012). The popularity of BOLD has ensured that its shortcomings are equally well known and accounted for regarding data interpretation (Ekstrom, 2010). Combining BOLD with other techniques will continue to provide additional physiological context to data interpretation as it relates to neurovascular coupling.

Metabolism

PET – As neurons fire, they consume glucose and oxygen to produce carbon dioxide and water. PET is the gold standard technique for measuring the cerebral metabolic rates of glucose (CMR_{glc}). A glucose analog labeled with a positron emitting radioisotope ([^{18}F]fluorodeoxyglucose, FDG) is intravenously administered. FDG is transported into brain

tissue through glucose transporters at the BBB, and is phosphorylated by hexokinase without being further metabolized to pyruvate. Thus, the radiolabel accumulates in areas of high glucose metabolism. Ultimately, the resulting gamma rays produced from positron and electron annihilation from the radiolabeled FDG are detected to quantify metabolic activity from glycolysis (Mosconi, 2013). Metabolism can be monitored anywhere in the body using this technique. The spatial resolution of PET is ~2-7 mm (Mosconi, 2013), and the scan times are slower than fMRI BOLD scans. As with fMRI, PET scanners and their upkeep are also costly. Nevertheless, the customization possible with PET makes it valuable for many purposes that range from detecting tumors to assessing neurotransmitter receptor activity (Volkow et al., 1996).

Blood Flow

ASL fMRI – Arterial spin labeling (ASL) fMRI is a truer CBF measurement than BOLD fMRI, and can be acquired simultaneously with BOLD to offer complementary information (Liu and Brown, 2007). Using RF pulses to magnetically label water within arterial blood, ASL detects the perfusion of labeled water from capillary blood into tissue. Subtracting data collected in absence of magnetic labeling from a labeled scan quantifies CBF changes. It localizes capillary blood flow without convoluting results from oxygen metabolism or blood volume changes, which makes it ideal to quantify CBF changes resulting from neuronal activity (Liu and Brown, 2007). Although ASL has lower signal-to-noise ratio and poorer temporal resolution than BOLD, there is lower inter-experimental and inter-subject variability with ASL use (Golay et al., 2004). Although combining BOLD and ASL fMRI provides information about oxygenation and CBF changes, it cannot discern the underlying causes (Bandettini, 2012).

Narrowing the Field of Detection

The global techniques described have provided invaluable data regarding neurovascular data between pathological and healthy human subjects. However, studies must be performed at a local level to understand the neurovascular influence of specific cell types, receptors, and neurotransmitters in a given brain region. Low spatial resolution also averages out the natural heterogeneity of the brain, where differences in neuronal architecture may have a profound impact on hemodynamic responses. Additionally, the preclinical animal models used to study neurovascular coupling require high resolution techniques, as areas of interest could be far less than 1 mm^2. Common methods capable of resolving neurometabolic components at high resolution, some even at the single cell level, are described below.

Cellular Activity

Electrophysiology – Microelectrodes detect extracellular neuronal activity at millisecond time resolutions through electrophysiological techniques: single-unit recording, multi-unit recording, and local field potentials (LFPs). These electrodes are placed within the brain and record action potentials as voltage changes, which are amplified and filtered. LFPs are analogous to spatially restrictive EEG recordings, but are acquired from electrodes placed within the brain that are not limited to the cortex. As with EEG, LPFs primarily monitor post-synaptic potential activity at 1-200 Hz frequencies and provide a more global view of brain waves. Filtering signals from 300-3,000 Hz instead isolates discrete action potentials or spikes from a single neuron, also known as single-unit activity (Reed et al., 2015). Single-unit recording requires high impedance (>2 MΩ) electrodes with low surface areas and precise positioning near a single neuron, whereas multi-unit recording electrodes are larger (often in array format), lower impedance, and collect information from multiple neurons (Coleman and Burger, 2015). As such, single-unit recordings are the ultimate high precision tool for monitoring neuronal

activity, but multi-unit recordings and LFPs sum multiple cells across hundreds of microns to address broader patterns of neuronal activity (Reed et al., 2015).

Oxygen

Amperometry – Oxygen electrochemically reduces at approximately -1.3 V (versus Ag/AgCl), a more cathodic potential than most other biologically-relevant molecules. Thus, microelectrodes can be inserted into the brain to selectively sense oxygen with minimal tissue damage. Constant potential amperometry holds an electrode at a sufficiently cathodic potential and measures the oxygen reduction current with millisecond time resolution. Absolute oxygen concentrations are quantified using a calibration plot. The common electrodes used are either platinum, Clark-type electrodes or carbon paste electrodes. Bare platinum fouls *in vivo*, and requires a membrane barrier between the tissue and the electrode surface. Meanwhile, carbon surfaces are resilient against biofouling and do not require any coatings. Carbon paste electrodes are >200 µm in diameter (Bolger et al., 2011) and platinum sensors are as small as 3-5 µm in diameter (Offenhauser et al., 2005), making amperometry a viable option for both locally averaged tissue oxygen and oxygen at spatial scales sufficient to resolve individual capillaries, respectively.

Fast-Scan Cyclic Voltammetry – Fast-scan cyclic voltammetry (FSCV) applies a waveform to a ~5-7 µm diameter carbon fiber. These waveforms scan across a voltage range at high scan rates (>100 V/s). Charging background current at the electrode scales with increasing scan rates, but its stability permits this nonfaradaic background current to be subtracted out to isolate the signal of interest. The most common oxygen sensing waveform begins at 0 V, scans anodically to +0.8 V, cathodically to -1.4 V, and finally returns to 0 V (Zimmerman and Wightman, 1991). Anodic limits as high as +1.45 V are used to detect adenosine also (Wang and Venton, 2016). As with amperometry, absolute oxygen concentrations can be calculated.

The unique advantage of FSCV over amperometry is the ability to simultaneously detect oxygen and other electrochemically active biological analytes. When FSCV currents are plotted against potential, the resulting cyclic voltammogram shape can confirm the identity of an analyte. Among them, adenosine (Phillis, 1988), norepinephrine (Bucher et al., 2014), and serotonin (Cohen et al., 1996) are known to exert vasomodulatory effects. Principle component regression analysis can separate current contributions from multiple co-presenting analytes, making it possible to accurately quantify concurrent changes between oxygen and vasoactive neuromodulators with high spatial resolution.

Metabolism

Two-Photon Fluorescence Microscopy – Nicotinamide adenine dinucleotide (NADH) serves as an electron carrier in glycolysis and oxidative metabolism processes, and nicotinamide adenine dinucleotide phosphate (NADPH) is a coenzyme regulated by glucose availability. These coenzymes are weakly autofluorescent, but the oxidized forms NAD^+ and NAD^+P are not. Utilizing the ~360 nm absorbance and ~460 nm emission wavelengths, metabolic changes at the cellular level are assessed through fluorescence measurements. Most often, two-photon fluorescence microscopy is used to avoid the harmful ultraviolet excitation wavelengths and instead excite NADH and NADPH with two infrared photons at ~720 nm (Piston and Knobel 1999). As local glucose concentrations rise, so too does the local fluorescence. This technique is used for acquiring immediate metabolic information at subcellular levels (Piston and Knobel, 1999, Kasischke et al., 2004), given the sub-micron spatial resolution and femtosecond laser excitation pulses (Murphy, 2013). Most importantly, two-photon fluorescence microscopy observes metabolism in fully intact tissue safely, even for minutes at a time without disrupting cell viability (Piston and Knobel, 1999).

Blood Flow

Laser Doppler Flowmetry – Laser Doppler flowmetry (LDF), also known as laser Doppler velocimetry, is the most common optical method used to monitor CBF changes. This method has commercially available tools (PeriFlux, Perimed AB, Sweden) that consist of two optical fibers: one fiber to direct a low powered laser beam at blood vessels, and the other to detect the reflected light. The motion of red blood cells flowing scatters the applied light such that the recorded light shifts in frequency according to the Doppler effect. The frequency shift is proportional to the CBF velocity. As such, this technique offers continuous, non-invasive CBF measurements. LDF cannot directly quantify CBF changes, but the relative changes measured correlate well with quantitative techniques (Hendel et al., 1983, Kvietys et al., 1985, Dirnagl et al., 1989). The depths assessed are on the order of millimeters (Nilsson et al., 1980), which permits superficial measurements only. The non-invasive, continuous flow measurements make this technique popular not only for cortical CBF measurements, but also cutaneous (Kastrup et al., 1989) and optical (Petrig et al., 1999) blood flow.

Hydrogen Clearance – Gas clearance is an inexpensive alternative to optical methods, and is used to assess subcortical CBF or CBF in freely behaving animals (Lowry et al., 1997). Hydrogen is an inert gas that otherwise does not exist endogenously, and that oxidizes to 2 H^+ (Young, 1980). Hydrogen gas is introduced into a subject through either an intravenous injection of hydrogen saturated saline, an extended hydrogen gas inhalation period, or *in situ* generation (Keller and Lübbers, 1972, Stosseck et al., 1974, Fellows and Boutelle, 1993). Once the tissue of interest is saturated, a platinum microelectrode held at +0.2 V (versus Ag/AgCl) detects amperometrically the exponential clearance of hydrogen from the tissue as a function of both CBF and diffusion. Flow is calculated by taking the ratio of a measurement without flow to a measurement with flow to eliminate the contribution of diffusion. The electrode size determines how local the measurements are, and range from 1-250 microns in diameter (Young, 1980).

Quantitative CBF changes are obtained, but these measurements are on the order of minutes apart (Young, 1980).

Multiplexed Detection of Neurovascular Coupling

With functional hyperemia involving so many biological domains, the ideal way to study it is by multiplexing techniques that measure different metrics to run concurrently. Unfortunately, a balance between electrical noise, strong magnetic fields, and physical equipment placement cannot always be achieved. Thus, many techniques run the same experimental paradigm twice using different techniques, which can have subtle or major flaws in reproducibility (Chen et al., 2008). Researchers continue to develop simultaneous detection with some success, as with PET/fMRI (Pichler et al., 2010), hydrogen clearance and amperometry (Lowry et al., 1997), ASL/BOLD fMRI (Liu and Brown, 2007), and even electrophysiology combined with simultaneous LDF and amperometric oxygen detection (Offenhauser et al., 2005), among many other combinations. These exemplify instances where techniques of similar spatial and/or temporal resolution are used together; however, combinations such as amperometry and BOLD fMRI can assess both global and localized oxygen changes to elucidate differences and similarities between the two (Lowry et al., 2010).

There are additional adaptations used to better understand neurovascular coupling mechanisms, but more is still needed. In lieu of observing neuronal activity, fMRI in particular has started to use optogenetic stimulations (Lee et al., 2010) to selectively activate known cellular populations as opposed to using less specific electrical or peripheral stimulations. Drugs are applied locally through iontophoresis to avoid systemic drug effects that could affect basal oxygen metabolism or vascular tone (Bucher et al., 2014). There are still gaps between technologies, such as the lack of a highly-resolved subcortical CBF measuring instrument and affordable, chemically selective neuronal excitation. To truly assess local versus global

neurovascular coupling and how it differs between specific and nonspecific stimuli, we address these gaps in this dissertation.

Overview of Dissertation

Understanding the underlying factors controlling neurovascular coupling is crucial with regards to interpreting a growing body of functional brain imaging studies. Technology has advanced both the number of techniques able to probe aspects of neurovascular coupling and the accuracy with which it can be done. While studies in humans normally are limited to non-invasive methods with more global scopes of detection, animal models have been studied to narrow in on neurovascular interactions as far down as the cellular level. The first two aims of this dissertation address the need for a subcortical CBF sensor with a miniaturized adaptation of electrolytic hydrogen clearance sensors. The third aim establishes the importance of evoked responses from different stimulation types by comparing electrical stimulation to chemically and spatially selective excitation with glutamate. The fourth aim takes local stimulation a step further to investigate a method of studying both local stimulation and local pharmacological manipulation in discrete microenvironments. As the spatial and temporal resolution brain functionality techniques used in man continue to improve, natural neurovascular heterogeneity must be characterized before pathologies can be interpreted correctly from brain functionality data.

REFERENCES

Araque A, Parpura V, Sanzgiri RP, Haydon PG (1999) Tripartite synapses: glia, the unacknowledged partner. *Trends Neurosci* **22**:208-215.

Attwell D, Buchan AM, Charpak S, Lauritzen M, MacVicar BA, Newman EA (2010) Glial and neuronal control of brain blood flow. *Nature* **468**:232-243.

Belanger HG, Vanderploeg RD, Curtiss G, Warden DL (2007) Recent neuroimaging techniques in mild traumatic brain injury. *J Neuropsychiatry Clin Neurosci* **19**:5-20.

Bolger FB, McHugh SB, Bennett R, Li J, Ishiwari K, Francois J, Conway MW, Gilmour G, Bannerman DM, Fillenz M (2011) Characterisation of carbon paste electrodes for real-time amperometric monitoring of brain tissue oxygen. *J Neurosci Methods* **195**:135-142.

Bucher ES, Fox ME, Kim L, Kirkpatrick DC, Rodeberg NT, Belle AM, Wightman RM (2014) Medullary norepinephrine neurons modulate local oxygen concentrations in the bed nucleus of the stria terminalis. *J Cereb Blood Flow Metab* **34**:1128-1137.

Carhart-Harris RL, Erritzoe D, Williams T, Stone JM, Reed LJ, Colasanti A, Tyacke RJ, Leech R, Malizia AL, Murphy K (2012) Neural correlates of the psychedelic state as determined by fMRI studies with psilocybin. *Proc Natl Acad Sci U S A* **109**:2138-2143.

Chen JJ, Wieckowska M, Meyer E, Pike GB (2008) Cerebral blood flow measurement using fMRI and PET: a cross-validation study. *Int J Biomed Imaging* **2008**.

Cohen D (1972) Magnetoencephalography: detection of the brain's electrical activity with a superconducting magnetometer. *Science* **175**:664-666.

Cohen Z, Bonvento G, Lacombe P, Hamel E (1996) Serotonin in the regulation of brain microcirculation. *Prog Neurobiol* **50**:335-362.

Coleman WL, Burger RM (2015) Extracellular Single-Unit Recording and Neuropharmacological Methods: Oxford University Press.

Daulatzai MA (2016) Cerebral hypoperfusion and glucose hypometabolism: Key pathophysiological modulators promote neurodegeneration, cognitive impairment, and Alzheimer's disease. *J Neurosci Res*.

DeFina LF, Willis BL, Radford NB, Gao A, Leonard D, Haskell WL, Weiner MF, Berry JD (2013) The association between midlife cardiorespiratory fitness levels and later-life dementia: a cohort study. *Ann Intern Med* **158**:162-168.

Dirnagl U, Kaplan B, Jacewicz M, Pulsinelli W (1989) Continuous measurement of cerebral cortical blood flow by laser—Doppler flowmetry in a rat stroke model. *J Cereb Blood Flow Metab* **9**:589-596.

Ekstrom A (2010) How and when the fMRI BOLD signal relates to underlying neural activity: the danger in dissociation. *Brain Res Rev* **62**:233-244.

Fellows LK, Boutelle MG (1993) Rapid changes in extracellular glucose levels and blood flow in the striatum of the freely moving rat. *Brain Res* **604**:225-231.

Fox PT, Raichle ME (1986) Focal physiological uncoupling of cerebral blood flow and oxidative metabolism during somatosensory stimulation in human subjects. *Proc Natl Acad Sci U S A* **83**:1140-1144.

Girouard H, Iadecola C (2006) Neurovascular coupling in the normal brain and in hypertension, stroke, and Alzheimer disease. *J Appl Physiol* **100**:328-335.

Golay X, Hendrikse J, Lim TC (2004) Perfusion imaging using arterial spin labeling. *Top Magn Reson Imaging* **15**:10-27.

Hajjar I, Brown L, Mack WJ, Chui H (2012) Impact of Angiotensin receptor blockers on Alzheimer disease neuropathology in a large brain autopsy series. *Arch Neurol* **69**:1632-1638.

Harris JJ, Reynell C, Attwell D (2011) The physiology of developmental changes in BOLD functional imaging signals. *Dev Cogn Neurosci* **1**:199-216.

Hendel PM, Lilien DL, Buncke HJ (1983) A study of the pharmacologic control of blood flow to delayed skin flaps using xenon washout. Part II. *Plast Reconstr Surg* **71**:399-407.

Hoge RD, Atkinson J, Gill B, Crelier GR, Marrett S, Pike GB (1999) Linear coupling between cerebral blood flow and oxygen consumption in activated human cortex. *Proc Natl Acad Sci U S A* **96**:9403-9408.

Iadecola C, Davisson RL (2008) Hypertension and cerebrovascular dysfunction. *Cell Metab* **7**:476-484.

Iadecola C, Nedergaard M (2007) Glial regulation of the cerebral microvasculature. *Nat Neurosci* **10**:1369-1376.

Jackson AF, Bolger DJ (2014) The neurophysiological bases of EEG and EEG measurement: A review for the rest of us. *Psychophysiology* **51**:1061-1071.

Kasischke KA, Vishwasrao HD, Fisher PJ, Zipfel WR, Webb WW (2004) Neural activity triggers neuronal oxidative metabolism followed by astrocytic glycolysis. *Science* **305**:99-103.

Kastrup J, Bülow J, Lassen N (1989) Vasomotion in human skin before and after local heating recorded with laser Doppler flowmetry. A method for induction of vasomotion. *Int J Microcirc Clin Exp* **8**:205-215.

Keller H, Lübbers D (1972) Flow measurement in the carotid body of the cat by the hydrogen clearance method. *Pflugers Arch* **336**:217-224.

Kvietys PR, Shepherd A, Granger DN (1985) Laser-Doppler, H_2 clearance, and microsphere estimates of mucosal blood flow. *Am J Physiol Gastrointest Liver Physiol* **249**:G221-G227.

Lauritzen M, Dreier JP, Fabricius M, Hartings JA, Graf R, Strong AJ (2011) Clinical relevance of cortical spreading depression in neurological disorders: migraine, malignant stroke, subarachnoid and intracranial hemorrhage, and traumatic brain injury. *J Cereb Blood Flow Metab* **31**:17-35.

Lee JH, Durand R, Gradinaru V, Zhang F, Goshen I, Kim D-S, Fenno LE, Ramakrishnan C, Deisseroth K (2010) Global and local fMRI signals driven by neurons defined optogenetically by type and wiring. *Nature* **465**:788-792.

Liu TT, Brown GG (2007) Measurement of cerebral perfusion with arterial spin labeling: Part 1. Methods. *J Int Neuropsychol Soc* **13**:517-525.

Logothetis NK (2003) The underpinnings of the BOLD functional magnetic resonance imaging signal. *J Neurosci* **23**:3963-3971.

Lowry JP, Boutelle MG, Fillenz M (1997) Measurement of brain tissue oxygen at a carbon paste electrode can serve as an index of increases in regional cerebral blood flow. *J Neurosci Methods* **71**:177-182.

Lowry JP, Griffin K, McHugh SB, Lowe AS, Tricklebank M, Sibson NR (2010) Real-time electrochemical monitoring of brain tissue oxygen: a surrogate for functional magnetic resonance imaging in rodents. *NeuroImage* **52**:549-555.

Mintun M, Raichle M, Martin W, Herscovitch P (1984) Brain oxygen utilization measured with O-15 radiotracers and positron emission tomography. *J Nucl Med* **25**:177-187.

Murphy DB (2013) Fundamentals of light microscopy and electronic imaging: John Wiley & Sons.

Nelson AR, Sweeney MD, Sagare AP, Zlokovic BV (2016) Neurovascular dysfunction and neurodegeneration in dementia and Alzheimer's disease. *Biochim Biophys Acta Biochim Biophys Acta* **1862**:887-900.

Nilsson GE, Tenland T, Oberg PA (1980) Evaluation of a laser Doppler flowmeter for measurement of tissue blood flow. *IEEE Trans Biomed Eng* 597-604.

O'Herron P, Chhatbar PY, Levy M, Shen Z, Schramm AE, Lu Z, Kara P (2016) Neural correlates of single-vessel haemodynamic responses in vivo. *Nature*.

Offenhauser N, Thomsen K, Caesar K, Lauritzen M (2005) Activity-induced tissue oxygenation changes in rat cerebellar cortex: interplay of postsynaptic activation and blood flow. *J Physiol* **565**:279-294.

Ogawa S, Lee T-M, Kay AR, Tank DW (1990) Brain magnetic resonance imaging with contrast dependent on blood oxygenation. *Proc Natl Acad Sci U S A* **87**:9868-9872.

Peppiatt CM, Howarth C, Mobbs P, Attwell D (2006) Bidirectional control of CNS capillary diameter by pericytes. *Nature* **443**:700-704.

Petrig BL, Riva CE, Hayreh SS (1999) Laser Doppler flowmetry and optic nerve head blood flow. *Am J Ophthalmol* **127**:413-425.

Phillis J (1988) Adenosine in the control of the cerebral circulation. *Cerebrovasc Brain Metab Rev* **1**:26-54.

Pichler BJ, Kolb A, Nägele T, Schlemmer H-P (2010) PET/MRI: paving the way for the next generation of clinical multimodality imaging applications. *J Nucl Med* **51**:333-336.

Piston DW, Knobel SM (1999) Real-time analysis of glucose metabolism by microscopy. *Trends Endocrinol Metab* **10**:413-417.

Pizzella V, Marzetti L, Della Penna S, de Pasquale F, Zappasodi F, Romani GL (2014) Magnetoencephalography in the study of brain dynamics. *Funct Neurol* **29**:241.

Plewes DB, Kucharczyk W (2012) Physics of MRI: a primer. *J Magn Reson Imaging* **35**:1038-1054.

Reed S, Jego S, Adamantidis A (2015) Electroencephalography and Local Field Potentials in Animals: Oxford University Press.

Rolfe D, Brown GC (1997) Cellular energy utilization and molecular origin of standard metabolic rate in mammals. *Physiol Rev* **77**:731-758.

Roy CS, Sherrington CS (1890) On the regulation of the blood-supply of the brain. *J Physiol* **11**:85.

Sloan H, Austin V, Blamire A, Schnupp JW, Lowe AS, Allers K, Matthews PM, Sibson NR (2010) Regional differences in neurovascular coupling in rat brain as determined by fMRI and electrophysiology. *NeuroImage* **53**:399-411.

Stosseck K, Lübbers DW, Cottin N (1974) Determination of local blood flow (microflow) by electrochemically generated hydrogen. *Pflugers Arch* **348**:225-238.

Thompson JK, Peterson MR, Freeman RD (2004) High-resolution neurometabolic coupling revealed by focal activation of visual neurons. *Nat Neurosci* **7**:919-920.

Uğurbil K, Toth L, Kim D-S (2003) How accurate is magnetic resonance imaging of brain function? *Trends Neurosci* **26**:108-114.

Uludağ K, Dubowitz DJ, Yoder EJ, Restom K, Liu TT, Buxton RB (2004) Coupling of cerebral blood flow and oxygen consumption during physiological activation and deactivation measured with fMRI. *NeuroImage* **23**:148-155.

Volkow ND, Fowler JS, Gatley SJ, Logan J (1996) PET evaluation of the dopamine system of the human brain. *J Nucl Med* **37**:1242.

Wang Y, Venton BJ (2016) Correlation of transient adenosine release and oxygen changes in the caudate-putamen. *J Neurochem*.

Young W (1980) H_2 clearance measurement of blood flow: a review of technique and polarographic principles. *Stroke* **11**:552-564.

Zimmerman JB, Wightman RM (1991) Simultaneous electrochemical measurements of oxygen and dopamine in vivo. *Anal Chem* **63**:24-28.

Zlokovic BV (2011) Neurovascular pathways to neurodegeneration in Alzheimer's disease and other disorders. *Nat Rev Neurosci* **12**:723-738.

CHAPTER 2: DESIGN AND CHARACTERIZATION OF A MICROFABRICATED HYDROGEN CLEARANCE BLOOD FLOW SENSOR[1]

Introduction

Cerebral blood flow (CBF) increases in activated brain regions to deliver energy in the forms of glucose and O_2 – a phenomenon known as functional hyperemia (Iadecola, 2004, Haydon and Carmignoto, 2006, Attwell et al., 2010). This increase also serves to maintain non-cytotoxic levels of metabolic products and conserve physiological pH following neuronal activity. Disease states such as ischemia can dysregulate hyperemia and generate or perpetuate brain damage, as neurons become both deprived of energy substrates and exposed to toxic levels of neurotransmitters and metabolic products (Hossmann, 1994, Iadecola, 2004, Haydon and Carmignoto, 2006). Beneath the cerebral cortex, densely packed capillaries fine-tune CBF activity to maintain homeostasis (Iadecola, 2004, Attwell et al., 2010). A broad literature exists studying cortical CBF (Harper and Glass, 1965, Dirnagl et al., 1989, Takano et al., 2006), but studying microvasculature control in the deep brain can provide new insight into pathologies hallmarked by CBF dysregulation, as well as flow activity in the behaving brain.

Numerous techniques have been used to measure CBF, including optical methods and tracer clearance approaches (Kety, 1951, Ter-Pogossian et al., 1970, Prinzen and Bassingthwaighte, 2000, Boas and Dunn, 2010, Shih et al., 2012). Laser Doppler flowmetry and laser speckle imaging are the most popular optical techniques, but the size of commercially

[1] This chapter previously appeared as an article in the Journal of Neuroscience Methods. The original citation is as follows: Walton LR, Edwards MA, McCarty GS, Wightman RM (2016) Design and characterization of a microfabricated hydrogen clearance blood flow sensor. *J Neurosci Methods* **267**:132-140.

available probes (500 μm or greater in diameter) risks extensive tissue damage to areas below the cortical surface (Dirnagl et al., 1989, Dunn et al., 2001, Shih et al., 2012). Clearance techniques, which rely on detecting the transport of an inert tracer to quantify flow, can measure CBF throughout the brain. However, these methods are costly (e.g. magnetic resonance imaging) and/or have a finite number of measurements per animal dictated by the number of unique labels available (e.g. fluorescent tags for microspheres) (Prinzen and Bassingthwaighte, 2000, Edvinsson and Krause, 2002). Sensitivity to motion artifacts further excludes the most commonly used techniques, optical and magnetic resonance imaging, from CBF measurements in behaving subjects. As an increasing number of common anesthetics (e.g. isofluorane) are known to have vasoactive effects (Ueki et al., 1992, Lindauer et al., 1993, Matta et al., 1999), development of a technique capable of exploring deep within the brain during conscious activity is highly desired.

Inert gases are attractive clearance tracers in biological subjects, as gas clearance can make an unlimited number of measurements per subject, detect CBF below the cortex, and perform in both anesthetized and freely-moving animals, all while quantifying CBF in ways that correlate highly with values obtained from competing techniques (Kety, 1951, Aukland et al., 1964, DiResta et al., 1987, Fellows and Boutelle, 1993, Machens et al., 1995, Lowry et al., 1997, Pell et al., 2003). The most affordable clearance gas is H_2, introduced through inhalation, injection of H_2-saturated saline, or electrolytic generation (Aukland et al., 1964, Stosseck et al., 1974, Young, 1980). The lattermost, electrolytic H_2 clearance (EHC), generates H_2 *in situ* and monitors its clearance to measure blood flow. Using a collector-generator electrode array, inert H_2 is generated galvanostatically from endogenous water and reoxidized at a potentiostatic collector electrode. Common biological interferents oxidize at higher potentials than H_2, so a low collector potential ensures specificity for *in vivo* use (Young, 1980). Inhalation and injection H_2 clearance methods have poor temporal resolution, as gas takes minutes to permeate through tissues and saturate the brain for a single measurement (Meyer et al., 1972, Lowry et al., 1997),

whereas EHC generates gas locally and reduces saturation time to seconds (Stosseck et al., 1974, Koshu et al., 1982). However, existing EHC electrodes are a millimeter or larger in diameter, too large for anything other than superficial CBF measurements (Stosseck et al., 1974, Koshu et al., 1982, DiResta et al., 1987). Despite its superior temporal resolution, EHC has not been used for CBF detection in subcortical, freely-moving experiments due to the technical limitations of probe size.

In this paper we use photolithography to fabricate a platinum electrode array capable of EHC that is an order of magnitude smaller than previous sensors (Stosseck et al., 1974, Koshu et al., 1982). Micron-scale dimensions improve spatial resolution and allow for sub-surface CBF measuring with minimal tissue damage. Microfabricated EHC fulfills the need for a tool capable of measuring CBF in the deep brain on a more physiological timescale than existing gas clearance methods, with the crucial benefit of applicability during freely-behaving experiments. Here, we characterize our EHC array, assess its suitability as a blood flow sensor, and present a theoretical framework for analyzing the data it produces.

Experimental

Chemicals and Solutions

Chemicals were received from Sigma Aldrich (St. Louis, MO) unless otherwise noted. Phosphate buffered saline (PBS, 140 mM NaCl, 3 mM KCl, 10 mM NaH_2PO_4) was diluted from a 10x stock and adjusted to pH = 7.4 with 5 M NaOH on the day of use. Hexaammineruthenium (III) trichloride (RuHex) was dissolved in 0.1 M KCl. McIlvaine buffers were made on the day of use from 0.1 M citric acid and 0.2 M K_2HPO_4, according to the pH value desired. DL-Noradrenaline hydrochloride (norepinephrine, NE) was added to buffer immediately prior to collecting rate data. All solutions were at 25 °C.

Platinum Electrode Array Fabrication

Platinum EHC arrays (Figure 2.1A) were fabricated using instruments at both the North Carolina State University Nanofabrication Facility (NNF) and the Chapel Hill Analytical and Nanofabrication Laboratory (CHANL) at UNC Chapel Hill. The process used was similar to arrays that we previously reported (Dengler and McCarty, 2013). Silicon wafers (University Wafer, Inc., Boston MA) were insulated with silicon nitride (3000 Å) using low-pressure chemical vapor deposition (LPCVD). Photolithography was performed using a negative tone photoresist (NFR 016 D2, JSR Corp., Tokyo, Japan) following dynamic application of hexamethyldisilazane (HMDS) as an adhesion promoter to obtain a thickness of approximately 3.7 µm. After exposure and development of the photoresist, the nitride was dry-etched using reactive ion etching (RIE) to pattern trenches of approximately 600 Å. Titanium metal was evaporated over the entire wafer (200 Å) to aid adhesion between the LPCVD nitride and subsequently evaporated platinum (400 Å). Lift-off was achieved with acetone, followed by a standard RCA-1 clean.

The arrays were insulated with silicon nitride (3000 Å) using plasma-enhanced chemical vapor deposition (PECVD). Photolithography using HMDS followed by S1813 positive tone photoresist (Shipley, Marlborough, MA) isolated areas of electrical exposure. The PECVD nitride was dry-etched through to the LPCVD nitride. A thick (>10 µm), protective layer of positive photoresist (AZ 4620, Shipley) was spun atop the wafer. Each wafer totaled 81 individual devices with different array dimensions, 26 of which were the geometry described in this paper. Devices were ultimately isolated using a dicing saw. Electrical connections to contact pads were made manually under a microscope using stainless steel wire and silver epoxy (MG Chemicals, Canada). Platinum devices were cleaned via voltammetric cycling in 0.5 M H_2SO_4 and were excluded from the study if the steady state current measured by slow-scan voltammetry in quiescent RuHex solution was not in agreement with that predicted by theory (finite element simulations). Platinum black coatings were applied to 3 devices, as previously described (Shin et al., 2008), to increase electrochemically active surface area. Carbon arrays

used for cyclization experiments were previously fabricated in the laboratory and had the same dimensions as the platinum devices used in this paper (Dengler and McCarty, 2013).

Data Acquisition

Custom hardware was assembled (UNC Chemistry Electronics Shop, Chapel Hill, NC) for galvanostatic control of the generator electrode. Voltammetry data was collected with a Chem-Clamp potentiostat (Dagan Corporation, Minneapolis, MN) and filtered at 100 Hz. Carbon disk measurements were made using an EI-400 potentiostat (Ensman Instruments, Bloomington, IN). All data were acquired using custom, locally written LabVIEW (National Instruments, Austin, TX) programs with 60 Hz collection frequency. A Ag/AgCl wire reference was used and potentials reported herein are relative to this electrode. Galvanostatic generation was used to ensure consistent H_2 production regardless of electrode fouling or surface changes that could affect the voltage response. Generator currents were -100 nA unless otherwise noted. The collector potential was held at +0.25 V. Between each galvanostatic pulse, the collector electrode was cycled briefly (2-4 s, 20 V s^{-1}, from -0.5 V to +1.0 V) to maintain platinum surface integrity and collector current reproducibility.

Norepinephrine Cyclization Experiments

The rate of the cyclization of NE-orthoquinone (the oxidation product of NE) to leuco-noradrenochrome was used to assess the suitability of the devices for detecting flow rates, using an experimental paradigm akin to that used in clearance data. Electrode arrays of identical geometry to the platinum electrode array, but with carbon electrodes, were used. The collector was held at 0.0 V, and the generator used 10 s, +100 nA pulses to oxidize NE to NE-orthoquinone. Data were acquired in McIlvaine buffers of varying pH (7.40 - 8.05) before and after the addition of 100 μM NE.

The rate of cyclization in solutions of the same pH range was independently measured using potential step chronoamperometry at a glassy carbon disk (r = 1.5 mm) collected at 60 Hz. The electrode was polished for 30 s with a 0.05 µm alumina slurry, rinsed with methanol and deionized H_2O, and sonicated for 1 minute between each data collection to maintain consistency (Hu et al., 1985). Rates of cyclization for each pH were calculated as previously described (Hawley et al., 1967).

Modeling

Finite element modeling was used to calculate the spatially varying H_2 concentration over time. At time *T*=0 the current at the generator was stepped from zero, i.e., no electrochemical reaction occurring, to a cathodic current, i_{gen} (taken to be negative in the following discussion), achieving the reduction reaction in Equation 1. The current returns to zero at time *T**.

$$2\,H^+ + 2\,e^- \rightarrow H_2 \tag{1}$$

The initial concentration of H_2 was taken to be to be zero throughout the simulation domain. Mass transport was described by the time-dependent version of the reaction-diffusion Equation 2, which is solved in the three dimensions; X, Y and Z.

$$\frac{\partial C}{\partial T} = D\nabla^2 C - \kappa C \tag{2}$$

C represents the concentration of H_2, *D* = 5x10^{-5} cm^{2}s^{-1} its diffusion coefficient (Macpherson and Unwin, 1997), *T* the time (s), and κ (s^{-1}) the first order rate constant H_2 clearance, as proposed by Stosseck et al. (Stosseck et al., 1974, Young, 1980).

The boundary condition for the generator electrode is

$$D\nabla C \cdot \underline{n} = \frac{i_{gen}(T)}{2AF} \tag{3}$$

where

$$i_{gen}(T) = \begin{cases} i_{gen} & \forall\ 0 \le T \le T^* \\ 0 & \forall\ T<0 \ and \ T>T^* \end{cases} \tag{4}$$

In these equations, $\underline{n}$ is the inward pointing unit normal, *F* is Faraday's constant and *A* is the generator electrode area. The factor of 2 arises from Equation 1 stoichiometry. Uniform surface flux is assumed, as the reaction is kinetically limited within the current range investigated. Implicit in this description is the assumption that all of the current is consumed by the evolution of H_2 (Equation 1) and that generated H_2 adsorption to the surface is negligible (Macpherson and Unwin, 1997).

The insulating parts of the array are described by

$$\nabla C \cdot \underline{n} = 0 \tag{5}$$

and the exterior of the domain is taken to have zero concentration of H_2, that is

$$C = 0 \tag{6}$$

The collector electrode potential is set such that the reverse reaction of Equation 1 occurs at a diffusion-limited rate and is also described by Equation 6. The current at the collector, i_{coll}, is an integral of the flux computed over the surface of the electrode,

$$i_{coll} = 2D \int \nabla C \cdot \underline{n} \tag{7}$$

where the 2 comes from the stoichiometry in Equation 1.

To reduce the number of degrees of freedom we normalized the equations in time, length and concentration by making the following substitutions

$$t = \frac{T}{\tau} \quad \text{where} \quad \tau = \frac{a^2}{D} \tag{8}$$

$$x = \frac{X}{a}; y = \frac{Y}{a}; z = \frac{Z}{a} \tag{9}$$

$$c = C/\chi \quad \text{where} \quad \chi = -i_{gen}\frac{a}{2AFD} \tag{10}$$

Where *a* is a characteristic length from the geometry, which in our case was taken to be the width of the collector electrode. This leads to the normalized version of Equation 2:

$$\frac{\partial c}{\partial t} = \nabla^2 c - kc \tag{11}$$

with the normalized rate constant *k* defined as

$$k = \kappa\tau \tag{12}$$

and a modified set of boundary conditions

$$\begin{array}{ll} \nabla c\cdot\underline{n} = -1 & \forall\ 0 \le t \le t^* \\ \nabla c\cdot\underline{n} = 0 & \forall\ t<0\ and\ t > t^* \end{array} \tag{13}$$

$$\nabla c \cdot \underline{n} = 0 \tag{14}$$

$$c = 0 \tag{15}$$

that are the normalized equivalents of Equations 3, 5, and 6 respectively, applying to the same boundaries in the transformed geometry, and $t^* = T^*/\tau$. Note, $\underline{n}$ is used here to represent the inward pointing unit normal in the transformed coordinates.

The i_{coll} in non-normalized coordinates is related to the normalized form, $\tilde{\imath}_{coll}$, by

$$\begin{array}{l} i_{coll}(T) = Da\chi\tilde{\imath}_{coll}(t) \\ \tilde{\imath}_{coll}(t) = \int \nabla c(t)\cdot\underline{n} \end{array} \tag{16}$$

where the integration is taken over the electrode in the normalized coordinates.

We made the useful observation that Equation 11 displays linearity; that is, if both $c_1(t)$ and $c_2(t)$ are linear then $c_3(t) = d_1c_1(t) + d_2c_2(t)$ will also be linear for any values d_1 and d_2. This property arises from the first order clearance rate description and is not true for general clearance expressions. We also observe that Equation 11 is time invariant, meaning that another solution for any value of t_0 is $c_4(t) = c_1(t + t_0)$.

If we define $c_\infty(t)$ as the solution for an infinitely long current pulse, initiated at $t = 0$, then we can derive the solution for a pulse of duration t^*, also initiated at $t = 0$, is described by

$$c_{t^*}(t) = c_\infty(t) - c_\infty(t - t^*) \tag{17}$$

Equation 11 is satisfied by the linearity relation ($d_1 = 1$, $d_2 = -1$) and time invariance ($t_0 = t^*$). Boundary conditions 14 and 15 are trivially satisfied and 13 is satisfied by the summation of the fluxes, which cancel out for $t > t^*$. The current is similarly given by

$$\tilde{\imath}_{coll,t^*}(t) = \tilde{\imath}_{coll,\infty}(t) - \tilde{\imath}_{coll,\infty}(t - t^*) \tag{18}$$

Where $\tilde{\imath}_{coll,t}$ and $\tilde{\imath}_{coll,\infty}$ represent the normalized collector current for a current pulse of duration t^* and infinite length, respectively. Thus we can restrict ourselves to solving these equations for an

infinite pulse length, in practice until a (quasi) steady-state behavior is reached, for a range of geometries in the normalized space.

Computational Details

The solution to the equations was calculated using the commercial finite element modeling package COMSOL Multiphysics 4.3a (COMSOL AB) and was performed on the Biomedical Analysis and Simulation Supercomputer (BASS) at UNC Chapel Hill. The equations were discretized using a mesh which was chosen to be finest around the edge of the electrodes where flux is greatest. The mesh was determined to be sufficiently fine when further refinements did not perturb the solution. Similarly, the extent of the domain was made sufficiently large such that it did not affect the derived solution.

Simulated Flow Rate Analysis

Noise (0.02 – 0.4 nA) was added to simulated data at all flow rates, including 0 s^{-1}, in the form of normally distributed, random numbers with a zero mean. This process was repeated 5 times for each noise amplitude to determine the variation of the observed response. When performing analysis, data from 0 – 8 s was disregarded to exclude the generating pulse time and the first second of clearance and analyzed according to Stosseck et al (*vide infra*) (Stosseck et al., 1974). Statistical work was performed in GraphPad Prism 6 (GraphPad Software, San Diego, CA, USA). Student's *t*-tests were used to determine significance, defined as $P < 0.05$.

Results

EHC arrays consisting of two individually addressable platinum electrodes were microfabricated (Figure 2.1A). The platinum is electrically insulated beneath silicon nitride, with

the exception of two pads at the top that connect to either the potentiostat or galvanostat, and a window at the tapered tip that exposes band electrodes where EHC is performed (Figure 2.1A, inset). The total probe width at the active electrode window is 100 µm, an order of magnitude smaller than existing EHC probes and more similar to existing microfabricated arrays used *in vivo* (Stosseck et al., 1974, Chen et al., 2009). The electrically insulated region between each electrode is approximately 5 µm wide. We used the two outer bands, each 100 x 20 µm, as the generator and the center electrode, 100 x 10 µm, as the collector. While exchanging the choice of the generator and collector would result in a higher overall collection efficiency (CE), defined as the percentage of the generator current measured at the collector electrode, the smaller generator area decreases the maximum current that could be applied and offers no signal enhancement. Higher current densities risk limiting the electrode lifespan or generating H_2 bubbles (Stosseck et al., 1974, Fernández et al., 2014). Of the isolated, diced devices from two separately processed wafers, 42 / 52 (80.8%) were functional, 6 / 52 (11.5%) were excluded (criteria for exclusion *vide supra*), and 4 / 52 (7.7%) could not have functionality assessed due to human error.

Characterizing Platinum Arrays

The one-electron reduction of RuHex (III) to RuHex (II) is an outer-sphere redox system with fast electron transfer kinetics that is ideal for characterizing microelectrodes. To validate that the electrodes had been correctly produced, cyclic voltammetry was performed at 5 mV s^{-1} in degassed 2.5 mM RuHex (III) solutions to obtain steady state currents (i_{ss}). Background subtracted voltammogram currents show excellent agreement with simulation-calculated i_{ss} values (D = 9x10^{-6} cm^2s^{-1}, Figure 2.1B, dashed lines) (Macpherson et al., 1997).

RuHex (III) reduction at the generator served as a model system to compare experimental clearance curves to those calculated. A current pulse (i_{gen} = -100 nA) reduced RuHex (III) to RuHex (II). This current is within the kinetically controlled current regime of a

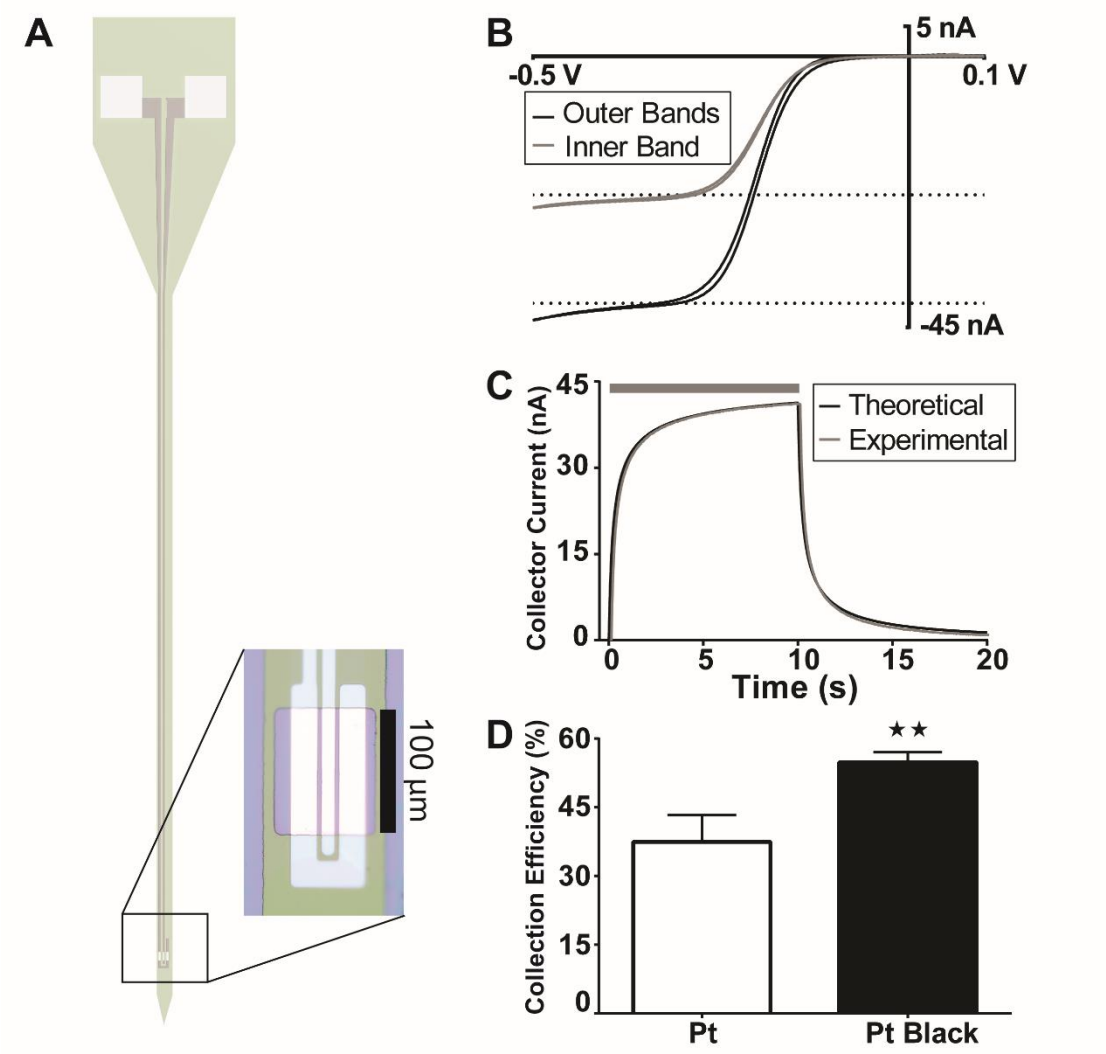

Figure 2.1. Microfabricated platinum arrays are characterized by voltammetry and amperometry. (A) Model (to scale) of the full device shows two separately addressed, 100 µm long electrodes (inset: micrograph) selectively exposed at the tip. Inset color key: Purple is exposed silicon, green is silicon nitride, grey is insulated platinum beneath the nitride and white is bare platinum. (B) Cyclic voltammogram (5 mV s-1) in degassed solution containing 2.5 mM RuHex and 0.1 M KCl. Theoretical steady state currents, indicated as dashed lines, were used to confirm active electrode surface areas. (C) Clearance curves obtained from generating RuHex (II) (35 mM) in the period indicated by the grey bar, and collecting RuHex (III). Outer electrodes used -100 nA pulses to reduce RuHex (III). The inner electrode, held at +0.25 V, detects RuHex (II) oxidation as faradaic current. Experimental RuHex clearance shows excellent agreement with simulations of the same system. (D) The collection efficiencies, taken at the plateau current, significantly increases when all electrodes are electroplated in platinum black (Student's t-test: $t_{(2,6)} = 4.804$, P = 0.003).

35 mM solution (i_{ss} = -578.5 nA at the generator) to eliminate the possibility of reducing other species (e.g. O_2). The current at the collector, held at +0.25 V to re-oxidize Ru(II), shows excellent agreement with the response calculated from simulations matching the experimental conditions (Figure 2.1C).

The theoretical response was calculated with varying pulse durations. Simulations determined that a 10 s generator current pulse was sufficient to reach locally saturated current with an expected 41.3% CE. Experimental results were in good agreement with CEs of 37.4 ± 5.9% ($t_{(2,4)}$ = 1.478, P >0.05, Figure 2.1D). If greater CE were required, coating all electrodes with platinum black was shown to increase electroactive surface area significantly as compared to bare platinum, enhancing experimental CE to 54.8 ± 2.2% ($t_{(2,6)}$ = 4.804, P = 0.003) (Shin et al., 2008).

Hydrogen Generation and Clearance

EHC at bare platinum electrodes was first tested in an acidic solution, 0.5 M H_2SO_4, both because of its ability to clean platinum surfaces and for its availability of free protons. The electrodes were initially cycled between -0.5 and +1.0 V at 20 mV s^{-1} and verified as clean when the cyclic voltammograms at 20 V s^{-1} produced the classic peaks indicative of H_2 and O_2 adsorption and desorption (Figure 2.2A). The pulse time necessary to achieve steady-state CE could be decreased to 7 s (Figure 2.2B), as H_2 has a larger diffusion coefficient than RuHex.

Table 2.1 summarizes CE values obtained from EHC experiments in various solutions. Solutions left open to air had 25.2 ± 3.0% CE (n = 5 devices, dashed line, Figure 2.2B), significantly poorer than theoretical predictions of 43.6% CE ($t_{(2,4)}$ = 13.71, P = 0.0001, n = 5). When the solution was degassed, the decrease in O_2 was seen in the steady-state cyclic voltammograms as increased area beneath the H_2 adsorption-desorption peaks and diminished area beneath those of O_2 (Figure 2.2A). This is consistent with the idea that degassed solutions have less O_2 capable of adsorbing to, and thus partially passivating, the active area of a bare

platinum surface (Bard et al., 1980). The clearance response in degassed acid closely matched that predicted by simulation (black line vs. gray line, Figure 2.2B) and achieved 34.6 ± 5.9% CE ($t_{(2,3)}$ = 3.05, P > 0.05, n = 4). Similarly, in solutions of aerated PBS, no collection current was obtained using i_{gen} = -100 nA, and i_{gen} = -700 nA pulse yielded only 0.49 ± 0.18% CE ($t_{(2,3)}$ = 479.0, P < 0.0001, n = 4). Once degassed, 30.4 ± 7.4% CE could be achieved in PBS using i_{gen} = -100 nA ($t_{(2,2)}$ = 3.09, P > 0.05, n = 3 devices).

The decrease in CE is due to an O_2-dependent competing reduction that consumes a large fraction of the generator current and produces one or more species that are undetectable amperometrically at +0.25 V. While this is problematic for *in vitro* studies in air-saturated solutions, O_2 concentrations in the deep brain are approximately 5 times lower (~50 µM vs. ~250 µM at pH 7.4, 25 °C (Robinson and Cooper, 1970)), thus it is expected that a majority of the current would go into producing H_2 *in vivo* (Feng et al., 1988, Ndubuizu and LaManna, 2007). It is important to note that the +0.25 V holding potential is sufficiently higher than the reduction potential of O_2 itself, in addition to being lower than the oxidation potentials of common biological interferents (e.g. H_2O_2, ascorbic acid), ensuring that *in vivo* measurements will be insensitive to fluctuations in these analytes and specific for H_2 (Aukland et al., 1964, Young, 1980).

Another operational problem *in vitro* was a decrease in CE with consecutive pulses (Figure 2.2C). Cycling the collector between pulses (20 V s^{-1}, 2-4 s, -0.5 to +1.0 V) regained optimal CE and maintained reproducibility. We attribute this passivation to oxygen atom adsorption to the positively-polarized collector surface, which strips off with cycling (Sugawara et al., 2012).

Modeled Flow

Localized flow, termed microflow, can be determined from clearance curves following the procedures of Stosseck et al. (Stosseck et al., 1974). After reaching saturated values of H_2 as

Table 2.1. EHC collection efficiencies measured at bare platinum microarrays. The center electrode served as the collector and two outer bands as generators. Collection efficiency reported at the end of a 7 s generation of H_2.

Solution	Pulse Amplitude (nA)	Collection Efficiency (%)[a]
Modeled Prediction	-100	43.6
Aerated H_2SO_4	-100	25.2 ± 3.0***
Degassed H_2SO_4	-100	34.6 ± 5.9
	-100	n/a[b]
Aerated PBS	-700	0.49 ± 0.18****
Degassed PBS	-100	30.4 ± 7.4

[a]Presented as averages ± SD. Significance calculated using Student's *t*-test and Welch's correction against theoretical values: ***$P < 0.001$, ****$P < 0.0001$.
[b]Generating current used was insufficient to produce a collector response above baseline.

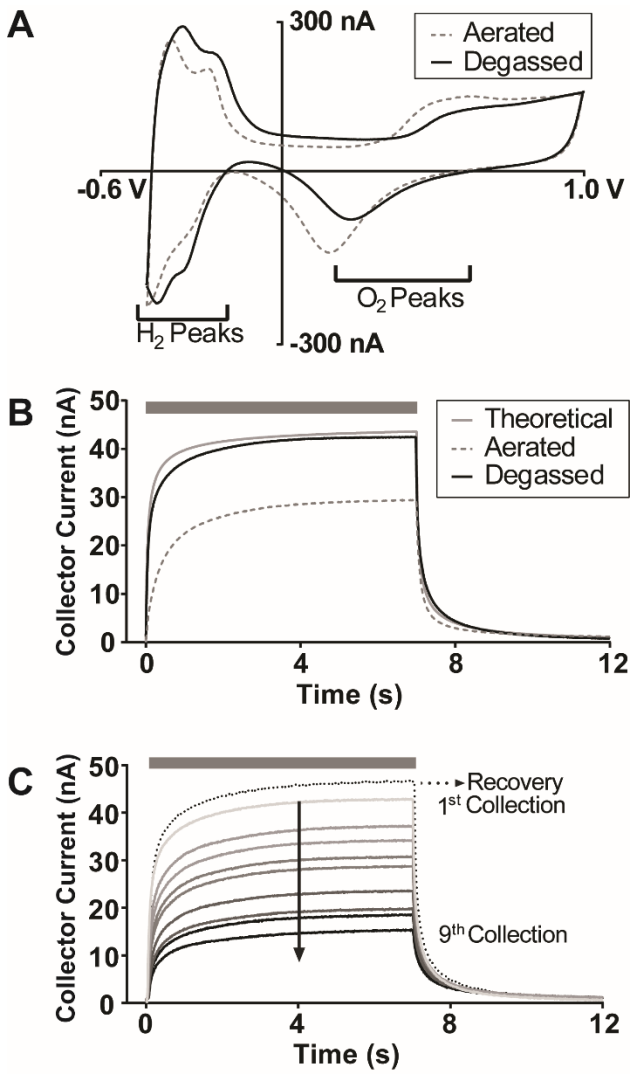

Figure 2.2. O_2 reduction reactions compete with EHC in 0.5 M H_2SO_4 at bare Pt electrodes. (A) Steady-state cyclic voltammograms (inner electrode shown, 20 V s^{-1}) indicate augmented H_2-adsorption peaks at a platinum surface in degassed acid versus air-saturated acid. In degassed solution, the decreased area beneath the O_2 adsorption-desorption peaks also presents with a potential shift of the cathodic peak, indicative of fewer oxides present at the surface. (B) EHC curves in 0.5 M H_2SO_4 indicate that CE decreases in air-saturated solutions, but can be restored to theoretical levels after N_2 bubbling. (C) Even EHC in degassed H_2SO_4 is subject to CE deterioration between subsequent pulses. Cycling the collector between pulses recovers CE (clearance curve indicated by dotted arrow) and ensures a maximized, consistent response. Generator pulses used were -100 nA. Collector potentials were held at +0.25 V.

assessed by a stable collection current plateau, galvanostatic generation ceases and H_2 clearance through diffusion and microflow begins. Note that, as total electroactive array area is 100 μm x 60 μm and the average spacing between blood vessels is ~50 μm, clearance from a H_2-saturated tissue volume will incorporate flow from multiple blood vessels (Klein et al., 1986).

Previous works have shown that the clearance curve, the monoexponential current decay following the cessation of the generator pulse, provides a more reliable prediction of microflow than absolute current values achieved at saturation (Fellows and Boutelle, 1993). Current during clearance is expected to obey the following relation from Stosseck et al.

$$\ln\left(\frac{i_0}{i_F}\right) = \kappa T + b \tag{19}$$

where i_0 (nA) and i_F (nA) represent clearance currents in the absence and presence of flow, respectively, κ (s^{-1}) is the microflow included in our model as a first-order rate (Equation 2), and b a constant deviation function (Stosseck et al., 1974). For convenience, we take T = 0 in Equation 19 to be the time when the generator pulse ends. Note, inhalation clearance experiments using millimeter-scale electrodes have reported polyexponential clearance rates because diffusion between grey and white matters differ, but our probe is small enough that we expect to avoid this issue (Fieschi et al., 1965).

Modeled clearance data were analyzed according to Equation 19 and plotted as $\ln(i_0/i_F)$ vs. t (Figure 2.3A). The first second of clearance data was disregarded as the current ratio was constant, ~1, and contains no microflow information. The linear regressions were fit to the data from t = 1-8 s (Figure 2.3A) to obtain κ values as slopes, making the time of one full CBF measurement total ~15 s and vastly improving temporal resolution compared to the multiple minutes per measurement seen in inhalation H_2 clearance (Fellows and Boutelle, 1993, Lowry et al., 1997). Ideally, these slope values would match the microflow rates input into the simulations, but fitting the data during this time range overestimates the input rates by ~15%, seen as a deviation from unity of the slope comparing the input microflow rates to those

obtained from the slope fit (Figure 2.3B). This deviation highlights the importance of theoretical validation and indicates that the assumptions within Equation 19 are not strictly true, especially for shorter times (Stosseck et al., 1974). We conjecture that this deviation arises due to the strong concentration gradients between the two electrodes, which are an order of magnitude closer than those originally used (Stosseck et al., 1974). Fitting clearance data to longer time lengths decreases the magnitude of microflow overestimation, however it lowers temporal resolution. Since the relationship between the theoretically predicted and actual flows is linear, actual microflow can be calculated using a conversion factor obtained from simulations that match experimental parameters. This clearance protocol and analysis outline was optimized to establish balance between temporal resolution and flow rate accuracy for our specific geometry. Different protocols can be used with similar analysis to achieve desired metrics.

As the *ln* ratio used in this simple EHC data analysis exaggerates current differences, one must also consider the magnitude of these differences and the impact of noise on their calculation. Randomly generated Gaussian noise was added to the simulated currents and the data were reanalyzed according to Equation 19 (Figure 2.3C). Simulations were calculated at ~60 Hz to match experimental protocol. As expected, data analyzed with greater noise gave less reliable microflow values (Figure 2.3D). However, with experimentally achievable low noise levels (<0.05 nA in this case), calculated microflows show close agreement with expected values. The exact noise amplitude that ensures accuracy is a function of the array geometry and acquisition protocol (data not shown). In conclusion, finite element modeling faithfully reproduces the experimental phenomena and can be used to optimize and assess the suitability of novel geometries, quantify the robustness to noise, and calculate calibration factors.

Detecting “Flow” with Microarrays

A first-order chemical reaction was used as an *in vitro* model amenable to use with our arrays, as clearance currents exhibit first-order exponential decay (Stosseck et al., 1974). The

conversion of NE-orthoquinone, the oxidized product of NE, to its cyclized form, leuco-noradrenochrome, was chosen, as the products are voltammetrically distinguishable and the reaction rate has been characterized. The rate of 0.98 ± 0.52 s^{-1} at pH 7.40 (Ciolkowski et al., 1992) can be slowed by increasing the pH, necessary to better mimic the microflow rates expected for *in vivo* EHC (i.e. 0.005-0.030 s^{-1}) (Sakurada et al., 1978).

We initially assessed the cyclization rate at a range of pH values by stepping the potential at a polished glassy carbon electrode from -0.4 V to +0.5 V. The current-time response for each pH value was analyzed according to the time-dependent equation for an ECE process (Hawley and Feldberg, 1966). The cyclization rates obtained were plotted against their corresponding pH values to verify the expected linear relationship (Figure 2.4A, R^2 = 0.79). Calculated rates were between 0.37 s^{-1} at pH 8.13 and 0.70 s^{-1} at pH 7.40.

Carbon pyrolyzed photoresist film (PPF) collector-generator arrays were used to monitor the cyclization rate because their surfaces can be stripped of the cyclized product, known to foul electrodes, by scanning to high voltages (Takmakov et al., 2010). Electrodes were assessed using cyclic voltammetry in solutions of 100 µM NE (Figure 2.4B). With 50 mV s^{-1} scan rates, NE is oxidized and reaches a diffusion-limited plateau at ~0.1 V. No reduction peak is observed on the reverse scan as there is sufficient time for the NE-orthoquinone to diffuse away. At 500 mV s^{-1}, two reduction peaks are observed relating to NE-orthoquinone (Peak 1) and its cyclized form (leuco-noradrenochrome, Peak 2) (Hawley et al., 1967).

For clearance measurements, generator electrodes oxidized NE (i_{gen} = +100 nA, 10 s) while the collector held 0.0 V; a potential sufficient to detect NE, but not the cyclized product (Figure 2.4B). In buffer, the collector current changes were negligible (-0.04 ± 0.02 nA), which confirmed collection currents as being solely NE-orthoquinone. The 50 mV s^{-1} voltammogram i_{ss} shows that the complete oxidation of NE to NE-orthoquinone will consume 2-3 nA, thus we are confident that the same diffusion-limited quantity is generated in all experiments. Voltage at the generator exceeded that required to completely oxidize NE in our solutions (Figure 2.4C).

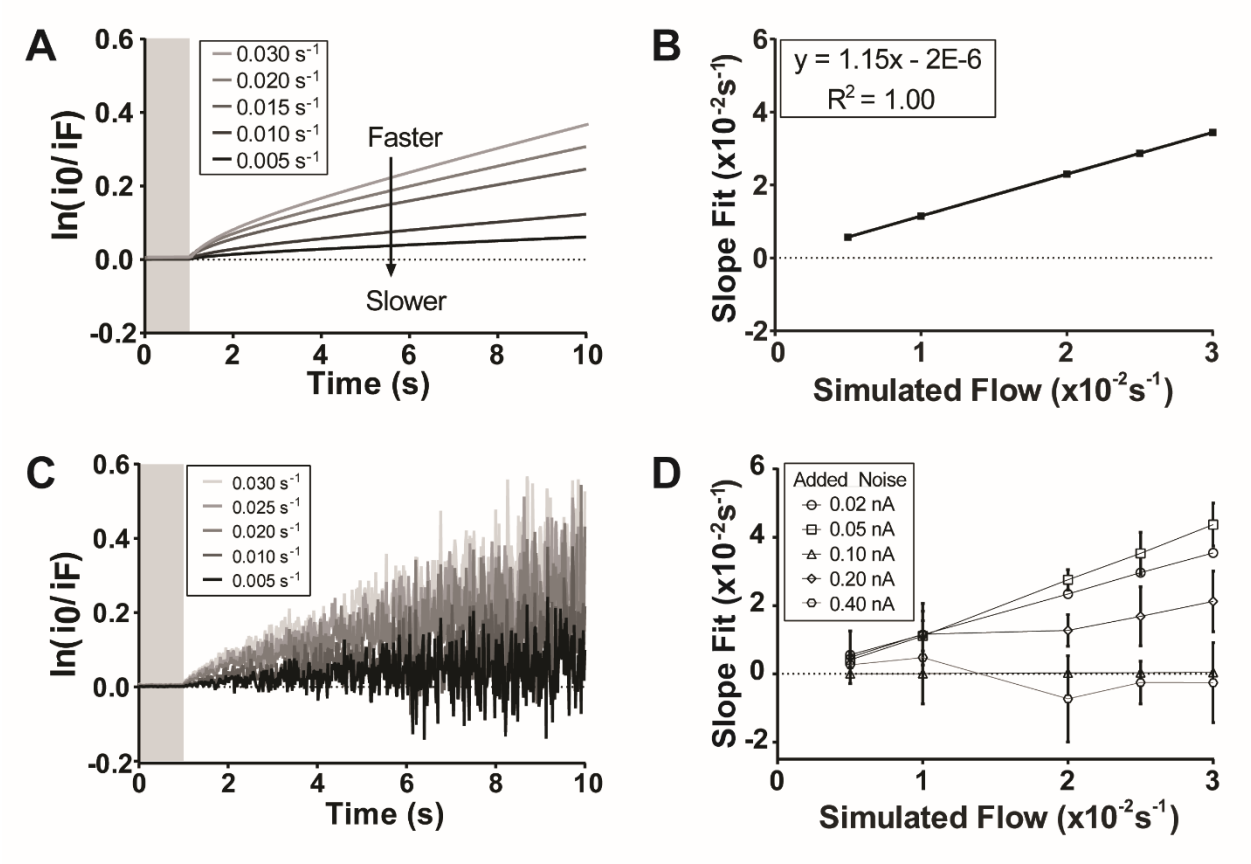

Figure 2.3. Computer modeling predicted experimental inaccuracies in flow rate calculations from EHC data. (A) Simulated clearance curves for a range of physiologically expected flow rates were calculated and plotted following analysis with Equation 19. Time = 0 indicates the cessation of the generating pulse. The first second of clearance (shaded box) is excluded from the linear regression fit. (B) The linear fit slopes from plot A were compared to the actual rates used in the model. The calculated fits overestimated the true rate, but in a highly predictable manner amenable to correction. (C) The data from A with added Gaussian noise (0.02 nA). (D) Linear fits from C data with greater noise amplitudes can be less accurate at predicting the true microflow values. N = 4 replicates per noise value, per flow. Error bars ± SD.

In solutions within the pH range studied, a non-zero i_{ss} was achieved within 5 s (-0.54 ± 0.05 nA, -0.74 ± 0.08 nA, -1.00 ± 0.13 nA, for pH 7.62, 7.83, 8.05, respectively), indicating that a portion of the oxidized product was not cyclized (Figure 2.4D). Higher collector currents at higher pH values are consistent with cyclization rates slowing under increasingly basic conditions. It is impossible to slow the reaction rate to zero to perform a $\ln(i_0/i_F)$ analysis, however, the current variability indicates that the array can sense reduced NE-orthoquinone before an intracyclization process that occurs at rates between 0.37 - 0.70 s^{-1}. This experimental demonstration coupled with the previous theoretical results demonstrate the feasibility of measuring a wide range of microflow rates, including those expected for CBF.

An important observation from these data is that the noise in the current collector is 0.02 ± 0.009 nA, below the 0.05 nA maximum noise for accurate determination of CBF (*vide supra*). This justifies the previously made assertion that we may use these devices to measure CBF. We conclude that our chosen geometry is capable of discerning microflow for rates at least as low as 0.005 s^{-1} and as high as 0.70 s^{-1}, which is well above what is to be expected *in vivo*.

Conclusions

We report microfabricated EHC electrodes that are capable of detecting and reliably quantifying changes in CBF expected *in vivo*. Finite element modeling accurately reproduces the experimental current and allows us to calculate calibration factors, quantify the effect of noise, and choose optimized geometries and protocols. Microfabrication, which allows batch fabrication of implantable sensors in reproducible yields of >80%, enables EHC arrays to be a more affordable alternative to existing CBF detection techniques. These devices have high temporal and spatial resolution, and implanting an electrode ensures its insensitivity to subject motion. These advantages over both traditional EHC sensors and other CBF measuring techniques importantly present opportunities for future experiments where *in vivo* CBF quantification can take place in freely-moving subjects beneath the cortex.

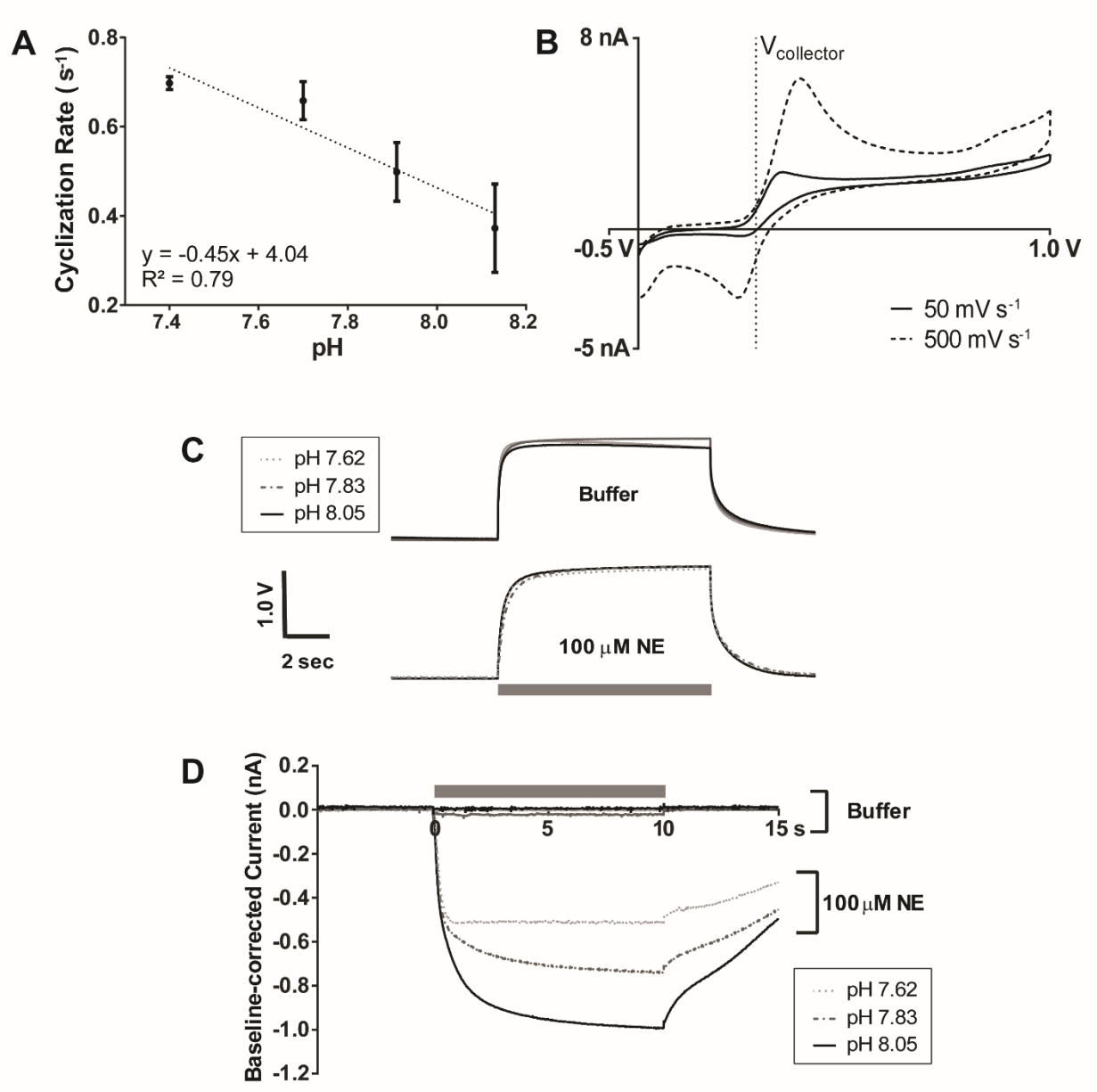

Figure 2.4. The intracyclization rate of NE-orthoquinone modeled a first order reaction decay in lieu of perfusion flow experiments. (A) The rate of the reaction was determined in solutions of varying pH using potential-step amperometry at a glassy carbon disk electrode (n = 4 replicates). (B) Cyclic voltammetry performed in 100 µM NE solutions was used to select a collector potential, $V_{Collector}$ = 0.0 V, to detect Peak 1, NE, and exclude faradaic currents from Peak 2, leuco-noradrenochrome. (C) Representative voltage vs. time traces at the generator electrode producing a 10 s, +100 nA pulse. NE oxidation significantly raised the voltages necessary to produce a generating pulse against buffer alone (1.59 ± 0.002 from 1.45 ± 0.01 V, $t_{(2,4)}$ = 9.262, P = 0.0008). (D) Representative current vs. time plots with the collector held at 0.0 V during a 10 s, +100 nA pulse. In solutions with NE, the collector was capable of detecting Peak 1 from B across all pH values tested (n = 11 replicates). Grey bars indicate pulse time. Error bars indicate ± SD.

REFERENCES

Attwell D, Buchan AM, Charpak S, Lauritzen M, MacVicar BA, Newman EA (2010) Glial and neuronal control of brain blood flow. *Nature* **468**:232-243.

Aukland K, Bower BF, Berliner RW (1964) Measurement of local blood flow with hydrogen gas. *Circul Res* **14**:164-187.

Bard AJ, Faulkner LR, Leddy J, Zoski CG (1980) Electrochemical Methods: Fundamentals and Applications: Wiley New York.

Boas DA, Dunn AK (2010) Laser speckle contrast imaging in biomedical optics. *J Biomed Opt* **15**:011109-011109-011112.

Chen Y-Y, Lai H-Y, Lin S-H, Cho C-W, Chao W-H, Liao C-H, Tsang S, Chen Y-F, Lin S-Y (2009) Design and fabrication of a polyimide-based microelectrode array: application in neural recording and repeatable electrolytic lesion in rat brain. *J Neurosci Methods* **182**:6-16.

Ciolkowski EL, Cooper BR, Jankowski JA, Jorgenson JW, Wightman RM (1992) Direct observation of epinephrine and norepinephrine cosecretion from individual adrenal medullary chromaffin cells. *J Am Chem Soc* **114**:2815-2821.

Dengler AK, McCarty GS (2013) Microfabricated microelectrode sensor for measuring background and slowly changing dopamine concentrations. *J Electroanal Chem* **693**:28-33.

DiResta G, Kiel J, Riedel G, Kaplan P, Shepherd A (1987) Hybrid blood flow probe for simultaneous H_2 clearance and laser-Doppler velocimetry. *Am J Physiol Gastrointest Liver Physiol* **253**:G573-G581.

Dirnagl U, Kaplan B, Jacewicz M, Pulsinelli W (1989) Continuous measurement of cerebral cortical blood flow by laser-Doppler flowmetry in a rat stroke model. *J Cereb Blood Flow Metab* **9**:589-596.

Dunn AK, Bolay H, Moskowitz MA, Boas DA (2001) Dynamic imaging of cerebral blood flow using laser speckle. *J Cereb Blood Flow Metab* **21**:195-201.

Edvinsson L, Krause DN (2002) Cerebral Blood Flow and Metabolism: Lippincott Williams & Wilkins.

Fellows LK, Boutelle MG (1993) Rapid changes in extracellular glucose levels and blood flow in the striatum of the freely moving rat. *Brain Res* **604**:225-231.

Feng Z-C, Roberts EL, Sick TJ, Rosenthal M (1988) Depth profile of local oxygen tension and blood flow in rat cerebral cortex, white matter and hippocampus. *Brain Res* **445**:280-288.

Fernández D, Maurer P, Martine M, Coey J, Möbius ME (2014) Bubble formation at a gas-evolving microelectrode. *Langmuir* **30**:13065-13074.

Fieschi C, Bozzao L, Agnoli A (1965) Regional clearance of hydrogen as a measure of cerebral blood flow. *Acta Neurol Scand* **41**:46-52.

Harper AM, Glass H (1965) Effect of alterations in the arterial carbon dioxide tension on the blood flow through the cerebral cortex at normal and low arterial blood pressures. *J Neurol Neurosurg Psychiatry* **28**:449.

Hawley M, Tatawawadi S, Piekarski S, Adams R (1967) Electrochemical studies of the oxidation pathways of catecholamines. *J Am Chem Soc* **89**:447-450.

Hawley MD, Feldberg SW (1966) Nuances of the ECE Mechanism. I. Development of the Theoretical Relationships for Chronoamperometry1a. *J Phys Chem* **70**:3459-3464.

Haydon PG, Carmignoto G (2006) Astrocyte control of synaptic transmission and neurovascular coupling. *Physiol Rev* **86**:1009-1031.

Hossmann K (1994) Viability thresholds and the penumbra of focal ischemia. *Ann Neurol* **36**:557-565.

Hu F, Karweik DH, Kuwana T (1985) Activation and deactivation of glassy carbon electrodes. *J Electroanal Chem* **188**:59-72.

Iadecola C (2004) Neurovascular regulation in the normal brain and in Alzheimer's disease. *Nat Rev Neurosci* **5**:347-360.

Kety SS (1951) The theory and applications of the exchange of inert gas at the lungs and tissues. *Pharmacol Rev* **3**:1-41.

Klein B, Kuschinsky W, Schrock H, Vetterlein F (1986) Interdependency of local capillary density, blood flow, and metabolism in rat brains. *Am J Physiol Heart Circ Physiol* **251**:H1333-H1340.

Koshu K, Kamiyama K, Oka N, Endo S, Takaku A, Saito T (1982) Measurement of regional blood flow using hydrogen gas generated by electrolysis. *Stroke* **13**:483-487.

Lindauer U, Villringer A, Dirnagl U (1993) Characterization of CBF response to somatosensory stimulation: model and influence of anesthetics. *Am J Physiol Heart Circ Physiol* **264**:H1223-H1228.

Lowry JP, Boutelle MG, Fillenz M (1997) Measurement of brain tissue oxygen at a carbon paste electrode can serve as an index of increases in regional cerebral blood flow. *J Neurosci Methods* **71**:177-182.

Machens HG, Pallua N, Mailaender P, Pasel J, Frank KH, Reimer R, Berger A (1995) Measurements of tissue blood flow by the hydrogen clearance technique (HCT): A comparative study including laser Doppler flowmetry (LDF) and the erlangen micro-lightguide spectrophotometer (EMPHO). *Microsurgery* **16**:808-817.

Macpherson JV, O'Hare D, Unwin PR, Winlove CP (1997) Quantitative spatially resolved measurements of mass transfer through laryngeal cartilage. *Biophys J* **73**:2771.

Macpherson JV, Unwin PR (1997) Determination of the diffusion coefficient of hydrogen in aqueous solution using single and double potential step chronoamperometry at a disk ultramicroelectrode. *Anal Chem* **69**:2063-2069.

Matta BF, Heath KJ, Tipping K, Summors AC (1999) Direct cerebral vasodilatory effects of sevoflurane and isoflurane. *Anesthesiology* **91**:677-677.

Meyer JS, Fukuuchi Y, Kanda T, Shimazu K, Hashi K (1972) Regional cerebral blood flow measured by intracarotid injection of hydrogen Comparison of regional vasomotor capacitance from cerebral infarction versus compression. *Neurology* **22**:571-571.

Ndubuizu O, LaManna JC (2007) Brain tissue oxygen concentration measurements. *Antioxid Redox Signal* **9**:1207-1220.

Pell GS, King MD, Proctor E, Thomas DL, Lythgoe MF, Gadian DG, Ordidge RJ (2003) Comparative study of the FAIR technique of perfusion quantification with the hydrogen clearance method. *J Cereb Blood Flow Metab* **23**:689-699.

Prinzen FW, Bassingthwaighte JB (2000) Blood flow distributions by microsphere deposition methods. *Cardiovasc Res* **45**:13-21.

Robinson J, Cooper JM (1970) Method of determining oxygen concentrations in biological media, suitable for calibration of the oxygen electrode. *Anal Biochem* **33**:390-399.

Sakurada O, Kennedy C, Jehle J, Brown J, Carbin GL, Sokoloff L (1978) Measurement of local cerebral blood flow with iodo [14C] antipyrine. *Am J Physiol Heart Circ Physiol* **234**:H59-H66.

Shih AY, Driscoll JD, Drew PJ, Nishimura N, Schaffer CB, Kleinfeld D (2012) Two-photon microscopy as a tool to study blood flow and neurovascular coupling in the rodent brain. *J Cereb Blood Flow Metab* **32**:1277-1309.

Shin JH, Privett BJ, Kita JM, Wightman RM, Schoenfisch MH (2008) Fluorinated xerogel-derived microelectrodes for amperometric nitric oxide sensing. *Anal Chem* **80**:6850-6859.

Stosseck K, Lübbers DW, Cottin N (1974) Determination of local blood flow (microflow) by electrochemically generated hydrogen. *Pflugers Arch* **348**:225-238.

Sugawara Y, Okayasu T, Yadav AP, Nishikata A, Tsuru T (2012) Dissolution mechanism of platinum in sulfuric acid solution. *J Electrochem Soc* **159**:F779-F786.

Takano T, Tian G-F, Peng W, Lou N, Libionka W, Han X, Nedergaard M (2006) Astrocyte-mediated control of cerebral blood flow. *Nat Neurosci* **9**:260-267.

Takmakov P, Zachek MK, Keithley RB, Walsh PL, Donley C, McCarty GS, Wightman RM (2010) Carbon microelectrodes with a renewable surface. *Anal Chem* **82**:2020-2028.

Ter-Pogossian MM, Eichling JO, Davis DO, Welch MJ (1970) The measure in vivo of regional cerebral oxygen utilization by means of oxyhemoglobin labeled with radioactive oxygen-15. *J Clin Invest* **49**:381.

Ueki M, Mies G, Hossmann K (1992) Effect of alpha-chloralose, halothane, pentobarbital and nitrous oxide anesthesia on metabolic coupling in somatosensory cortex of rat. *Acta Anaesthesiol Scand* **36**:318-322.

Young W (1980) H_2 clearance measurement of blood flow: a review of technique and polarographic principles. *Stroke* **11**:552-564.

CHAPTER 3: OPTIMIZING THE DESIGN AND FABRICATION OF MICROFABRICATED HYDROGEN CLEARANCE SENSOR FOR *IN VIVO* USE

Introduction

Cerebral blood flow (CBF) is a tightly regulated physiological process that replenishes glucose and oxygen (O_2) concentrations to brain tissue following neuronal activity. Glucose and O_2 are the key metabolic substrates consumed to maintain ion gradients in the brain, and when CBF becomes dysregulated, the collapse of these gradients can lead to cell death (Dirnagl et al., 1999, Zauner et al., 2002, Harris et al., 2012). To date, most CBF studies have been conducted in cortical locations, where optical techniques, such as laser Doppler flowmetry (Dirnagl et al., 1989) and two-photon microscopy (Helmchen et al., 2001), can obtain accurate and precise CBF measurements. However, both neuronal and vascular differences exist between the cortex and deeper brain regions (Iadecola and Nedergaard, 2007). To investigate CBF in subcortical regions, researchers have turned to either expensive magnetic resonance imaging (Calamante et al., 1999) or clearance techniques (Lacombe et al., 1980). Existing clearance methods are limited in that they either rely on highly-invasive electrodes, or are dependent upon a finite availability of unique fluorophores or radiolabels (Lacombe et al., 1980, Prinzen and Bassingthwaighte, 2000). To address these technical challenges and permit further subcortical CBF studies, we have sought to improve upon an existing clearance technique.

Hydrogen clearance is a well-established gas clearance method used to quantify CBF that correlates well with other accepted CBF-measuring techniques (Aukland et al., 1964, Young, 1980, Larsen et al., 2008). This method introduces inert H_2 into a biological system until it reaches a saturated level in the area of interest. The supply of H_2 is then ceased, and subsequent clearance of the gas is then measured through amperometric H_2 oxidation at a

polarized electrode. The current generated by H_2 oxidation decays exponentially as H_2 clears the tissue via diffusion and blood flow, and can be used to calculate CBF (Aukland et al., 1964). *In situ* electrolytic H_2 clearance (EHC) is the fastest of the H_2 clearance methods, and requires a platinum electrode array (Aukland et al., 1964, Stosseck et al., 1974, Young, 1980, Larsen et al., 2008). In EHC, a galvanostatic pulse from a generator electrode produces H_2, which is sensed at the second collector electrode (Stosseck et al., 1974). This electrochemical time-of-flight technique has been used in both animals and human studies, but the electrode sizes have historically limited brain applications (Koshu et al., 1982, Shima et al., 1985, DiResta et al., 1987, Kawasuji et al., 1988), as existing EHC sensors exceed a millimeter in diameter (Stosseck et al., 1974, DiResta et al., 1987). To limit tissue damage, smaller arrays are needed to perform EHC measurements in subcortical regions.

Recently, we miniaturized EHC arrays to a micron-scale using microlithography to both minimize tissue damage and improve spatial and temporal resolution for sub-cortical blood flow measurements (Walton et al., 2016). However, the accuracy of our previous approach relied on noise levels ≤50 pA. Though our *in vitro* measurements routinely had background noise of ~20 pA, greater noise levels are expected *in vivo*. Here, we take further advantage of computational modeling to optimize device geometries for both improving collection efficiencies (CEs), defined as the percent of generated H_2 that is oxidized and thereby sensed at the collector(s), and expanding the range of experimental background noises under which the devices can operate. Following the improved design of our arrays, we modified the microfabrication process to yield devices sufficiently thin to be used *in vivo*, as opposed to the thicker, diced prototype devices of our previous work (Walton et al., 2016). Together, these improvements will better serve the intended use of measuring localized CBF changes in subcortical brain regions.

Experimental

Chemicals and Solutions

KOH was obtained from Fisher Scientific (Pittsburgh, PA) and its solutions were made fresh immediately prior to wet etches. AZ1518 positive tone photoresist was obtained from AZ Electric Materials (Branchburg, NJ) and NFR 016 D2 negative tone photoresist was from JSR Corp. (Tokyo, Japan). All other photolithographic chemicals were purchased from Shipley (Marlborough, MA) unless otherwise noted.

Platinum Electrode Array Fabrication

Platinum EHC arrays were fabricated, in a process similar to previously-reported arrays (Walton et al., 2016), using instruments at both the North Carolina State University Nanofabrication Facility (NNF) and the Chapel Hill Analytical and Nanofabrication Laboratory (CHANL) at UNC Chapel Hill. All uses of photoresist were preceded by a dynamic acetone-methanol-isopropyl alcohol clean followed by dynamic application of hexamethyldisilazane (HMDS) as an adhesion promoter.

Backside. Silicon wafers (University Wafer, Inc., Boston MA), 200 µm thick, were insulated with silicon nitride (3400 Å) using low-pressure chemical vapor deposition (LPCVD). Photolithography began on the backside of the wafer. First, AZ1518 positive photoresist was spun on the wafer at 2750 rpm for 60 s and soft-baked at 95 °C for 60 s. The wafers were exposed to ultraviolet (UV) light for 4.8 s at a mask aligner (Karl Suss MA6), developed in MF319, and then hard-baked at 115 °C for 5 min. Reactive ion etching (RIE) was used to etch the backside nitride through to the silicon.

Level 1. The front of the wafer was spun with a negative photoresist (NFR 016 D2) at 3000 rpm for 40 s, followed by a 60 s soft-bake at 95 °C. After the Level 1 mask was aligned to the backside etches, the patterns were exposed to UV light for 3.5 s and baked at 95 °C for an

additional 90 s. After the wafers were developed, the nitride was dry-etched with RIE to pattern trenches of approximately 600 Å. Titanium metal was evaporated over the entire wafer (200 Å) to aid adhesion between the LPCVD nitride and subsequently evaporated platinum (400 Å). Lift-off was achieved with acetone, followed by a standard RCA-1 clean. Level 1 geometries were insulated with silicon nitride (15 kÅ) using plasma-enhanced chemical vapor deposition (PECVD).

Level 2. Photolithography using HMDS followed by S1813 positive photoresist isolated areas of electrical exposure on the front side of the wafer. Approximately half (6.5 kÅ) of the PECVD nitride was dry-etched through, leaving the other half to protect the front devices. Approximately 160 µm of silicon was wet-etched from the backside of the wafer in a solution of 30% KOH by weight, heated to 70-80 °C.

Level 3. S1813 positive resist was spun on the front side of the etched wafer at 2000 rpm for 60 s, soft-baked at 115 °C for 60 s, aligned to the Level 3 mask, UV-exposed for 12 s, developed in MF319, and finally hard-baked at 115 °C for an additional 5 min. The remainder of the PECVD and LPCVD nitrides was RIE etched through using the Level 3 pattern, the residual photoresist of which was plasma cleaned off prior to the releasing KOH step.

Release. The remaining 40 µm of silicon were wet-etched in hot KOH from both front- and backsides of the wafer until the silicon surrounding the devices was fully etched away, leaving devices to be removed manually from patterned “bridges” with a scalpel and tweezers (Figure 3.1A-B). Each wafer totaled 72 individual devices with one of the following four array dimensions described in Table 3.1: 20 of Device B, 21 of Device D, 14 of Device E, and 17 of Device F.

Modeling

EHC operates on the basis of applying a cathodic current i_{gen}, sufficient to reduce endogenous H^+, at a generator electrode to produce a discrete bolus of H_2 (Equation 1).

Table 3.1. Modeled geometries for platinum EHC microarrays. Inter-electrode spacing refers to the space between the central generator and each of the two collector electrodes.

Device	Generator Length (µm)	Generator Width (µm)	Collector Length (µm)	Collector Width (µm)	Inter-Electrode Spacing (µm)
A	100	20	100	30	10
B		20		30	25
C	200	20	200	30	25
D		20		30	35
E		30		30	25
F		50		25	25

Elsewise, the generator is held at 0 V to neither produce additional H_2, consume H^+, nor electrochemically affect other biological analytes (Young, 1980). The collector is held at +0.25 V throughout the duration of the experiments to amperometrically oxidize the H_2 delivered by diffusion and flow.

$$2\,H^+ + 2\,e^- \rightarrow H_2 \tag{1}$$

We used finite element modeling to calculate the H_2 concentrations as they varied spatially over time, as previously reported (Walton et al., 2016). Briefly, mass transport was modeled using a three-dimensional solution of the reaction-diffusion Equation 2, where *C* is the H_2 concentration, $D = 5\text{x}10^{-5}$ cm^2s^{-1} its diffusion coefficient (Macpherson and Unwin, 1997), *T* the time (s), and κ (s^{-1}) the first order rate constant for H_2 clearance, as proposed by Stosseck et al. (Stosseck et al., 1974, Young, 1980).

$$\frac{\partial C}{\partial T} = D\nabla^2 C - \kappa C \tag{2}$$

The generator electrode is bound by the following initial condition

$$D\nabla C \cdot \underline{n} = \frac{i_{gen}(T)}{2AF} \tag{3}$$

where

$$i_{gen}(T) = \begin{cases} i_{gen} & \forall\ 0 \le T \le T^* \\ 0 & \forall\ T<0\ and\ T>T^* \end{cases} \tag{4}$$

In these equations, $\underline{n}$ is the inward pointing unit normal, *F* is Faraday's constant, *A* is the generator electrode area, and 2 is from Equation 1 stoichiometry. Meanwhile, the concentration of H_2 at the collector is set to zero, as we assume that the reduction of H_2 at the applied potential is diffusion limited. This current, i_{coll}, is obtained by integrating the flux normal to the electrode surface as follows, taking into account the 2 from Equation 1 stoichiometry.

$$i_{coll} = 2D \int \nabla C \cdot \underline{n} \tag{5}$$

All data were normalized, and discrete pulses were modeled utilizing linear algebraic relationships shown in Equation 6, where $\tilde{i}_{coll,t}$ and $\tilde{i}_{coll,\infty}$ represent the normalized collector current for a current pulse of duration T^* and infinite length, respectively. We used T^* = 8 s.

$$\tilde{\imath}_{coll,t^*}(t) = \tilde{\imath}_{coll,\infty}(t) - \tilde{\imath}_{coll,\infty}(t - t^*) \quad (6)$$

Computational Details

The solution to the equations was calculated using the commercial finite element modeling package COMSOL Multiphysics 4.3a (COMSOL AB) and was performed on the Biomedical Analysis and Simulation Supercomputer (BASS) at UNC Chapel Hill. The domain over which calculations took place extended an order of magnitude past expected diffusion limits, such that it did not affect solutions at the electrode surfaces. A mesh was used to discretize solutions, and was made finest at the electrode edges where flux was greatest. Elsewhere, meshes were coarser to minimize simulation times while maintaining accuracy. Meshes were optimized to the point where further refinements did not alter solutions.

Calculating Noise Tolerance for Accurate Flow Analysis

Flow rates were calculated as described in detail previously (Walton et al., 2016), according to the following relation

$$\ln\left(\frac{i_0}{i_F}\right) = \kappa T + b \quad (7)$$

where i_0 (nA) and i_F (nA) represent clearance currents in the absence and presence of flow, respectively, κ (s^{-1}) is the microflow, and b is a constant deviation function (Stosseck et al., 1974). Briefly, modeled clearance data were plotted as $\ln(i_0/i_F)$ vs. T, excluding the first second of clearance data. With T=0 in Equation 7 defined as the end of the generator pulse current, post-pulse data T = 1-8 s were fit with linear regressions to obtain slope values, κ, that overestimated flow in a calculable, correctable manner dependent upon the array geometry. Fitting clearance data to longer time lengths decreased the magnitude of this microflow overestimation, but at the expense of temporal resolution.

Noise (0.02 – 0.4 nA) was added to simulated data at all flow rates, including 0 s^{-1}, in the form of normally distributed, random numbers with a zero mean. This process was repeated 5 times for each noise amplitude to simulate a variety of random environmental noise. The flow rates used in the modeling and the slopes obtained from the analyzed data were plotted on the abscissa and ordinate, respectively, and fit to a linear regression. The stronger the linear fit, the more reliable the accuracy of a CBF measurement under different experimental noise amplitudes.

Results and Discussion

We fabricated released devices in four different geometries (Figure 3.1A-B), each approximately 10 mm in length. The three EHC electrodes forming our array were located at the probe tip and exposed through a window in electrically-insulating silicon nitride. The dimensions of these geometries were chosen based on computer modeling where the central electrode was designated as the generator and the two adjacent electrodes to either side, being electrically connected, served as a single collector (Figure 3.1C). The average spacing between blood vessels is approximately 50 µm, and the electroactive array areas used here range from 20 x 100 µm to 50 x 200 µm, ensuring that the tissue affected by EHC will average flow values obtained from multiple blood vessels (Klein et al., 1986). The average thickness of these devices was 210 ± 24 µm at the base (n=6) and 15 ± 6 µm at the tip (n=4), compared to the uniform 450 ± 36 µm (n=9) of the diced devices published previously (Walton et al., 2016). We know from previous work (Walton et al., 2016) that utilizing a three-electrode array geometry maximizes collection efficiency when the central electrode is used as the generator and the adjacent electrodes serve as collectors. Data were modeled using this convention.

Optimizing our sensor geometry focused on mostly maximizing both the tolerated noise level and collection currents, while limiting the overall size of the electrode areas to physiologically reasonable dimensions. Tolerated noise refers to the amount of random

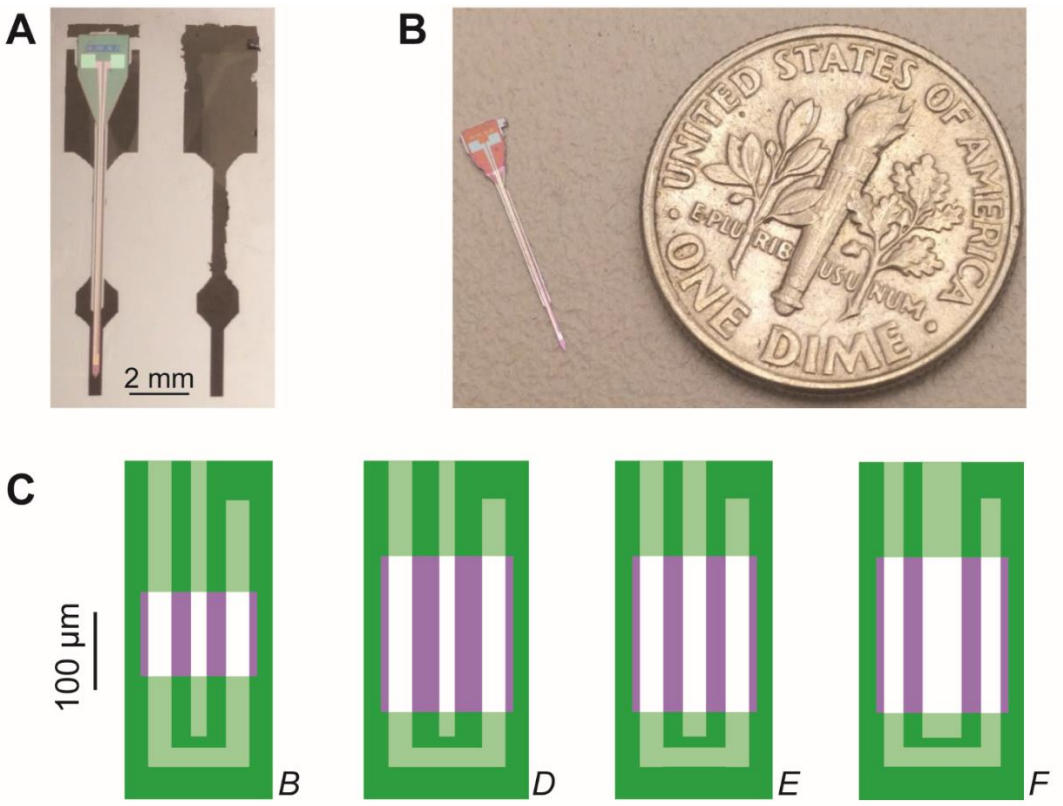

Figure 3.1. Platinum hydrogen clearance arrays were microfabricated in a modified workflow to produce devices thin enough for *in vivo* use with optimized dimensions. (A) A photograph of a wafer fragment shows how individual probes anchor to the wafer scaffold throughout the fabrication process through silicon “bridges” at their base (left). Bridges were broken to release the probes (right). (B) Optical image of a fully-released probe compared to a United States dime. Both the thickness and width tapered to a fine tip. (C) Expanded representations, to scale, of the four different array geometries fabricated in this work. The central platinum electrode was modeled as the generator, while the two electrodes to either side jointly served as a collector electrode. Letters in italics correspond to the devices in Table 3.1. Green represents PECVD silicon nitride, purple is exposed LPCVD silicon nitride, and white is bare platinum.

environmental noise that the sensor can be subjected to and still linearly correlate to actual CBF values used to model collector current, as described previously in detail (Walton et al., 2016). Briefly, clearance data were plotted according to Equation 7 for multiple, physiologically-relevant flow rates (0.005-0.03 s^{-1}). Flow rates were obtained from fitting these data to linear regressions, then plotted against the modeled ideal flow rates. Each geometry slightly overestimates the true flow value used to calculate clearance data, necessitating that this be done first in the absence of any environmental noise to obtain the device's flow correction factor (Walton et al., 2016). We artificially introduced random noise to the theoretical data and performed the analysis again to gauge the accuracy of the linear fits for a given noise amplitude. For the purposes of this study, we defined maximum tolerated noise to be the highest artificially-added noise amplitude that, when fit to a linear regression against true flow values, results in an $R^2 \geq 0.99$.

We modeled a variety of electrode geometries, summarized in Table 3.1. The collection efficiencies between the modeled devices were within 20% of one another (Figure 3.2A), though the fabricated devices (Devices B, D-F, Table 3.1) were within 10% of one another. The maximum tolerated noise thresholds for the devices varied from 23 – 180 pA (Figure 3.2B). Overall, the best balance struck between CE, total electrode width, and ability to more accurately quantify CBF came from modeling Device E.

We modeled Device A to resemble our previous device (Walton et al., 2016), using small electrode surface areas and narrow inter-electrode spacing, that is, the spacing between the generator and each collector electrode (Table 3.1). Models of this geometry had 72.0% CE and a 23 pA noise limit (Figure 3.2). The latter metric led us to omit this geometry from fabrication, as it approached the 20 pA background noise levels of our instrumentation. To investigate the effect of inter-electrode spacing, we increased this variable from 10 to 25 µm (Device B, Table 3.1). This decreased CE but roughly doubled the maximum tolerated noise limit (56.2% and 42 pA, respectively, Figure 3.2). To see if further increasing inter-electrode spacing would improve the tolerated noise limit more, we modeled a device with 35 µm inter-electrode spacing

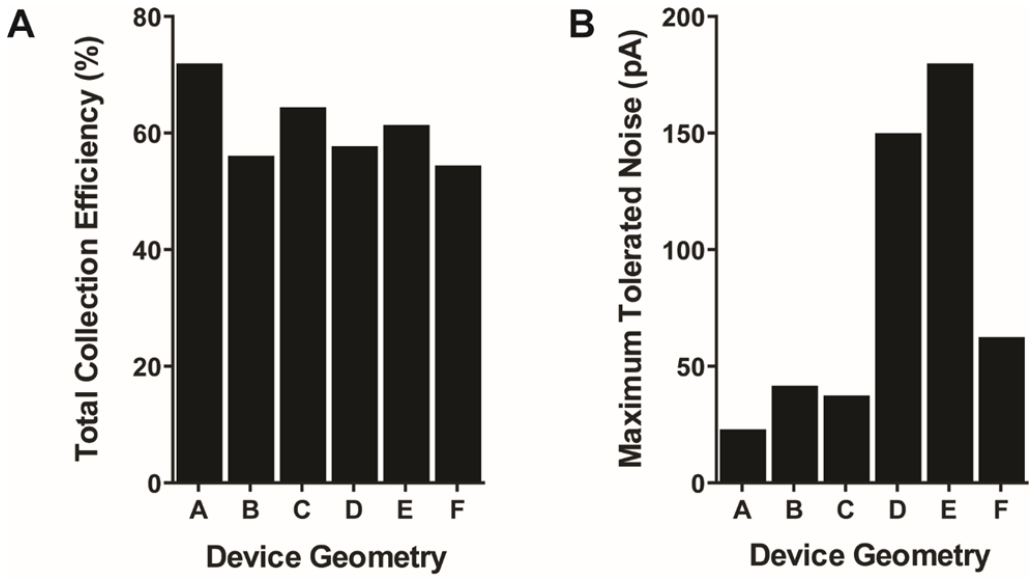

Figure 3.2. Optimizing device geometries affected both the collection efficiency and the tolerated electrical noise of hydrogen clearance microarrays. (A) Collection efficiency is defined as the combined, maximum collection efficiency from both collector electrodes during an 8 s modeled H_2 pulse (i.e., not fully steady-state) under conditions of no additional flow. The values with physiologically-relevant flow rates present (up to 0.030 s^{-1}) were still within 1% of these maximum values for all geometries. (B) Maximum tolerated noise is defined as the highest amplitude of background noise where a linear fit of experimentally-modeled data to true flow values is in agreement such that $R^2 \geq 0.99$, to provide confidence in the accuracy of obtained measurements.

(Device D, Table 3.1). This substantially improved noise limitations as predicted, with a modest decrease in CE (150 pA and 57.8%, respectively, Figure 3.2). Thus, inter-electrode spacing greatly impacted the maximum tolerated noise limit of our EHC arrays.

Collection current can be simplified from Equation 5 as being the product of flux (J), Faraday's constant (F), and the number of electrons involved (e^- = 2 for H_2 oxidation). As the latter two are constants, it became advantageous to maximize the flux integrated across the collectors, most easily achieved through increasing the electrode surface area. We investigated whether CE improved with greater surface areas. Devices B-C kept the same generator-to-collector surface area ratio (1:3), but the total surface area of Device B electrodes was half that of Device C electrodes. As such, the CE of Device B (56.2%, Figure 3.2A) was inferior to that of Device C (64.6%, Figure 3.2A) and the tolerated noise threshold rose slightly (42 to 38 pA from Device B and C, respectively, Figure 3.2B). Interestingly, Devices A-D had 1:3 ratios of generator-to-collector surface area ratios, but CEs for these devices ranged from 56.2 to 72.0% (Figure 3.2A) and tolerated noise from 23 to 150 pA (Figure 3.2B). Thus, both the absolute and relative electrode dimensions contribute to CE and maximum tolerated noise.

To change the surface area ratios while keeping the inter-electrode spacing consistent between models had detrimental effects on both explored metrics. The respective generator-to-collector surface area ratios for Device E and Device F were 1:2 and 1:1, with the same inter-electrode spacing, but Device E both had superior CE and tolerated more noise than Device F (61.6% versus 54.6% and 180 versus 63 pA, respectively, Table 3.1). With spacing kept constant, this contradicted the idea that larger generators would improve CE and suggested that the ratio of electrode surface areas has influence on both CE and tolerated noise.

Using the central electrode as a generator instead of the larger combined surface area of the two outer electrodes, as was done in our previous work (Walton et al., 2016), runs the risk of generating potentially-disruptive H_2 microbubbles with sufficient current densities applied (Fernández et al., 2014). We increased the surface areas of the central generator electrode to

provide more of a buffer against this risk. Device D was therefore compared to a device model that duplicated its dimensions with the exception of having a wider generator (Device E, Table 3.1). Both the CE and the maximum tolerated noise improved (57.8% to 61.6% and 150 to 180 pA from Device D to E, Table 3.1, Figure 3.2) with a wider generator dimension, though the inter-electrode spacing was decreased to compensate for the additional width and may have contributed to these effects. Device F further increased the generator width (and decreased the collector widths to compensate), yet this had detrimental effects on both CE and noise limitations (61.6% to 54.6% and 180 to 63 pA from Device E to F, Table 3.1, Figure 3.2). We concluded that, while a larger generator may reduce the risk of generating microbubbles, the relative size of the collectors and the spacing between the electrodes must adjust accordingly to maintain optimal CE and noise tolerance.

The maximum tolerated noise was greatly affected by both changing the inter-electrode spacing and modifying electrode surface areas between two sets of otherwise identical devices. Devices C and D had matching electrode surface areas, but the 10 µm wider inter-electrode spacing of Device D produced a nearly 4-fold difference between their maximum tolerated noise thresholds (180 versus 63 pA for Device C and D, respectively, Table 3.1). Meanwhile, Devices C and E were identical save for a 10 µm difference in generator widths. Device E, with the greater generator surface area, had nearly a 5-fold improvement in the maximum tolerated noise as compared to Device C (180 versus 38 pA, respectively, Table 3.1) with negligible effects on CE (61.6% versus 64.6%, respectively, Table 3.1). Future work is needed to fully investigate these relationships at a quantitative level.

Future Directions

Through a series of progressive geometry manipulations, we were able to customize electrode arrays using computational modeling to improve desirable qualities such as greater

CE or confidence in measurements taken in electrically-noisy environments. Further modeling could be used to explore more deeply the relationships between these metrics and device dimensions, or to tailor a device to cover larger tissue areas. The devices have been fabricated and released successfully, but require further testing to determine whether the electrodes are functional and agree with theoretical modeling as closely as previous devices (Walton et al., 2016).

Ultimately, these devices will be used to explore CBF changes *in vivo*. To reliably position these devices perpendicular to the brain's surface will require mounting the devices to a circuit board, as performed previously (Zachek et al., 2010). The 10 mm length of the device enables exploration throughout the entirety of the rat brain. The tapered thickness, which starts from approximately 15 μm at the tip to over 200 μm at the base where the electrical connections are made, will generate minimal tissue damage compared to existing EHC devices (Stosseck et al., 1974, DiResta et al., 1987). To confirm the utility of these devices in monitoring CBF, future work should investigate scenarios where CBF changes are reliably provoked, such as measurements in the cortex following whisker stimulation or cortical spreading depression (Dunn et al., 2001, Wang et al., 2003).

REFERENCES

Aukland K, Bower BF, Berliner RW (1964) Measurement of local blood flow with hydrogen gas. *Circul Res* **14**:164-187.

Calamante F, Thomas DL, Pell GS, Wiersma J, Turner R (1999) Measuring cerebral blood flow using magnetic resonance imaging techniques. *J Cereb Blood Flow Metab* **19**:701-735.

DiResta G, Arbit E, Lau N, Galicich J (1987) Measurement of regional cerebral blood flow using a combination laser Doppler-hydrogen clearance probe. *J Cereb Blood Flow Metab* **7**:S570.

Dirnagl U, Iadecola C, Moskowitz MA (1999) Pathobiology of ischaemic stroke: an integrated view. *Trends Neurosci* **22**:391-397.

Dirnagl U, Kaplan B, Jacewicz M, Pulsinelli W (1989) Continuous measurement of cerebral cortical blood flow by laser—Doppler flowmetry in a rat stroke model. *J Cereb Blood Flow Metab* **9**:589-596.

Dunn AK, Bolay H, Moskowitz MA, Boas DA (2001) Dynamic imaging of cerebral blood flow using laser speckle. *J Cereb Blood Flow Metab* **21**:195-201.

Fernández D, Maurer P, Martine M, Coey J, Möbius ME (2014) Bubble formation at a gas-evolving microelectrode. *Langmuir* **30**:13065-13074.

Harris JJ, Jolivet R, Attwell D (2012) Synaptic energy use and supply. *Neuron* **75**:762-777.

Helmchen F, Fee MS, Tank DW, Denk W (2001) A miniature head-mounted two-photon microscope: high-resolution brain imaging in freely moving animals. *Neuron* **31**:903-912.

Iadecola C, Nedergaard M (2007) Glial regulation of the cerebral microvasculature. *Nat Neurosci* **10**:1369-1376.

Kawasuji M, Kawajiri F, Iwa T (1988) Measurement of regional myocardial blood flow. Application of the electrolytic hydrogen clearance method in man. *J Thorac Cardiovasc Surg* **96**:775-781.

Klein B, Kuschinsky W, Schrock H, Vetterlein F (1986) Interdependency of local capillary density, blood flow, and metabolism in rat brains. *Am J Physiol Heart Circ Physiol* **251**:H1333-H1340.

Koshu K, Kamiyama K, Oka N, Endo S, Takaku A, Saito T (1982) Measurement of regional blood flow using hydrogen gas generated by electrolysis. *Stroke* **13**:483-487.

Lacombe P, Meric P, Seylaz J (1980) Validity of cerebral blood flow measurements obtained with quantitative tracer techniques. *Brain Res Rev* **2**:105-169.

Larsen M, Pelzer M, Friedrich PF, Bishop AT (2008) Measurement of bone blood flow using the hydrogen washout technique—Part II: Validation by comparison to microsphere entrapment. *J Orth Res* **26**:746-752.

Macpherson JV, Unwin PR (1997) Determination of the diffusion coefficient of hydrogen in aqueous solution using single and double potential step chronoamperometry at a disk ultramicroelectrode. *Anal Chem* **69**:2063-2069.

Prinzen FW, Bassingthwaighte JB (2000) Blood flow distributions by microsphere deposition methods. *Cardiovasc Res* **45**:13-21.

Shima I, Yamauchi S, Matsumoto T, Kunishita M, Shinoda K, Yoshimizu N, Nomura S, Yoshimura M (1985) A new method for monitoring circulation of grafted bone by use of electrochemically generated hydrogen. *Clin Orthop Relat Res* **198**:244-249.

Stosseck K, Lübbers DW, Cottin N (1974) Determination of local blood flow (microflow) by electrochemically generated hydrogen. *Pflugers Arch* **348**:225-238.

Walton LR, Edwards MA, McCarty GS, Wightman RM (2016) Design and characterization of a microfabricated hydrogen clearance blood flow sensor. *J Neurosci Methods* **267**:132-140.

Wang X, Pang Y, Ku G, Xie X, Stoica G, Wang LV (2003) Noninvasive laser-induced photoacoustic tomography for structural and functional in vivo imaging of the brain. *Nat Biotechnol* **21**:803-806.

Young W (1980) H_2 clearance measurement of blood flow: a review of technique and polarographic principles. *Stroke* **11**:552-564.

Zachek MK, Park J, Takmakov P, Wightman RM, McCarty GS (2010) Microfabricated FSCV-compatible microelectrode array for real-time monitoring of heterogeneous dopamine release. *Analyst* **135**:1556-1563.

Zauner A, Daugherty WP, Bullock MR, Warner DS (2002) Brain oxygenation and energy metabolism: part I—biological function and pathophysiology. *Neurosurgery* **51**:289-302.

CHAPTER 4: CHEMICALLY SELECTIVE, LOCAL GLUTAMATE STIMULATION USING IONTOPHORESIS

Introduction

Despite accounting for a small portion of total body mass, the brain uses a disproportionately large percentage of the body's resting energy. This discrepancy arises from the energetically expensive demands of neuronal communication and the maintenance of ionic gradients (Sokoloff, 1989). Metabolic substrates in the form of glucose and O_2 are replenished after neuronal activity via increased regional cerebral blood flow (CBF), where they are consumed to generate adenosine triphosphate (ATP) and reestablish ion gradients. To maintain energetic homeostasis, neuronal activity is typically coupled with increased CBF in a process termed functional hyperemia (Roy and Sherrington, 1890). However, when neuronal activity and CBF decouple, blood flow cannot replenish the energy consumed during neurotransmission. Energy deficits result in the collapse of ionic gradients, and often lead to neuronal death (Drake and Iadecola, 2007). CBF increases are not exclusively controlled by metabolic deficiencies however, as CBF changes in response to a task are unaltered by induced hypoglycemia and hypoxia (Powers et al., 1996, Mintun et al., 2000). Further, although CBF delivers excess O_2 to overcompensate for energy loss, the concentrations delivered vary depending on stimulus type and intensity (Nielsen and Lauritzen, 2001, Thompson et al., 2003, Offenhauser et al., 2005). Together, these suggest that neuronal activity and metabolic deficits play complex roles in the regulation of energy throughout the brain.

CBF is often measured by monitoring extracellular O_2 concentrations, where increases in O_2 can be attributed to increases in blood flow. This is the basis for blood oxygenation level-dependent (BOLD) functional magnetic resonance imaging (fMRI) (Ogawa et al., 1990);

however, positive BOLD fMRI signals (i.e., increases in oxygenated blood) only infer the presence of increased neural activity (Hillman, 2014). Fast-scan cyclic voltammetry (FSCV) is also used to measure O_2 concentration changes at high spatial resolution (Zimmerman and Wightman, 1991, Bucher et al., 2014), but electrochemical measurements offer no information about neuronal activity. Previously, we used a multimodal sensor to perform simultaneous voltammetric and single-unit electrophysiology measurements (Takmakov et al., 2011). Here, we expand the capabilities of our sensor to study both O_2 dynamics in conjunction with cell firing. This approach uses a single, minimally invasive carbon fiber microelectrode, and enables simultaneous detection of both neuronal activity and oxygen consumption in localized environments. Further, we coupled iontophoresis, a local drug delivery method, to FSCV and electrophysiology to form a comprehensive suite of techniques to study functional hyperemia. Through iontophoresis, we locally stimulated neurons by ejecting glutamate, an excitatory neurotransmitter (Krnjević and Phillis, 1963, Lamour et al., 1988, Nicola et al., 2000). Together, this multimodal method allowed us to investigate the link between glutamate-elicited neuronal excitation and coupled O_2 responses in localized microdomains.

In this study, we compared the effects of electrically stimulated glutamate versus local glutamate iontophoresis on O_2 dynamics between the dorsal striatum and somatosensory cortex. We first elicited endogenous glutamate release via electrically stimulating the prefrontal cortex (PFC), and found that striatal O_2 concentrations both increased and decreased in a manner dependent on stimulation intensity and the availability of ionotropic glutamate receptors (iGluRs). In contrast, glutamate iontophoresis in the striatum either responded with O_2 decreases or were unresponsive to glutamate. Finally, we compared the effects of locally-ejected glutamate on O_2 concentrations and cell firing between cortical and striatal locations. The majority of recording locations responded to glutamate iontophoresis with increased cell firing and subsequent O_2 decreases. Together, these data show that O_2 responds differently to electrically evoked glutamate release than to targeted, chemically-specific

glutamatergic excitation, and that neuronal firing does not always couple to O_2 throughout the cortex and striatum.

Experimental

Animal Care

All animal protocols were approved by the Institutional Animal Care and Use Committee of the University of North Carolina at Chapel Hill (UNC). Male Sprague-Dawley rats (300-450 g, Charles River, Wilmington, MA, USA) were pair-housed at UNC animal facilities, given food and water *ad libitum*, and kept on a 12 hour light/dark cycle. Care was taken to reduce the number of animals used and minimize their suffering. A total of 6 animals were used for stimulation experiments, and data were pooled and analyzed from 70 animals originally used for other protocols.

Surgery

Animals were anesthetized with urethane (1.5 g/kg i.p.) and placed in a stereotaxic frame (Kopf, Tujunga, CA, USA). Holes were drilled in the dorsal striatum (+0.7 or +2.0 mm A-P, +3.2 mm M-L, -2.5 to -3.5 mm D-V) for the carbon-fiber electrode, and the PFC (+3.0 mm A-P, +0.8 mm M-L, -3.0 mm D-V) for the stimulating electrode. Coordinates are relative to bregma from the Paxinos and Watson (2007) atlas. Depths were from dura mater. A Ag/AgCl reference electrode wire was placed in the contralateral hemisphere and served as an iontophoresis ground. Holes were drilled for glutamate iontophoresis studies in the striatum (+2.2 mm A-P, +1.7 mm M-L, -6.4 to -7.8 mm D-V) and somatosensory cortex (+0.6 mm A-P, +2.8 mm M-L and +2.0 mm A-P, +2.6 mm M-L, -0.9 to -2.0 mm D-V for each).

Drugs and Solutions

DL-2-amino-5-phosphonopentanoic acid sodium salt (AP5, NMDA receptor antagonist), and 1,2,3,4-Tetrahydro-7-nitro-2,3-dioxoquinoxaline-6-carbonitrile disodium salt (CNQX, AMPA receptor/kainate antagonist) were obtained from Abcam (Cambridge, MA, USA). All other chemicals were obtained from Sigma Aldrich (St. Louis, MO, USA). Drugs were dissolved in 5 mM NaCl and ejected iontophoretically using cathodic currents (-25 to -400 nA).

Voltammetric O_2 Measurements and Iontophoresis

Mutimodal sensors were fabricated as described previously from four-barrelled glass capillaries (Belle et al., 2013). Briefly, a ~5 µm diameter carbon fiber, pulled into a glass capillary, was inserted into a 4-barrel capillary and cut under a light microscope to an exposed length between 80 - 120 µm. The remaining barrels were filled with drug solutions.

Fast-scan cyclic voltammetry (FSCV) measurements were obtained and analyzed with a High-Definition Cyclic Voltammetry (HDCV) computer program (Bucher et al., 2014). The cyclic voltammetric waveform was 11 ms in duration, first scanned from a holding potential of 0.0 V to +0.8 V, then to -1.4 V, and finally back to the holding potential (vs. Ag/AgCl reference electrode) at a scan rate of 400 V s^{-1}. Carbon-fiber surfaces were conditioned in the brain by scanning the waveform at 60 Hz, followed by 10 Hz, each for 15 minutes. A repetition rate of 5 Hz was used for simultaneous electrochemical and elecrophysiological measurements as described previously (Takmakov et al., 2011). Locally-designed instrumentation controlled the connection of the carbon fiber alternately to a current transducer (for cyclic voltammetry) and a voltage follower (electrophysiology measurements) (Takmakov et al., 2011).

Iontophoretic ejections were performed by applying constant current (NeuroPhore BH-2 System, Harvard Apparatus, Holliston, MA, USA). Ejection timing was controlled by HDCV.

Iontophoretic barrels were primed at least 400 µm dorsal to the measurement region to ensure reproducible ejections.

Single-Unit Activity Electrophysiology

Single-unit activity was measured for 179 ms between each cyclic voltammetric scan. The data were amplified (x5,000), fed through a bandpass filter (300 – 3,000 Hz, Krohn-Hite Corp., Brockton, MA), and digitized using commercially-available software (Digitizer, Plexon, Dallas, TX, USA).

Electrically-Stimulated, Endogenous Glutamate Release

Two optically-isolated stimulators (NL, 800 A, Neurolog, Digitimer, Hertfordshire, UK) were used to generate electrical stimulations at a bipolar stainless steel electrode (Plastics One, West Lafayette, IN, USA) in the PFC glutamatergic cell bodies. A multimodal sensor was placed in the ipsilateral dorsal striatum. One drug barrel contained glutamate (200 mM) (Lamour et al., 1988), while another contained an AP5 (50 mM) and CNQX (10 mM) cocktail to antagonize iGluRs. Recordings were taken at locations where cells were present, defined as locations where single-unit activity accompanied a 2 s glutamate ejection using currents <-100 nA. The electrode depth was optimized for the strongest biphasic response while maintaining sensitivity to iontophoresed glutamate. One location was used per animal.

First, baseline files were collected without stimulation. Then, stimulations were optimized for biphasic O_2 responses while maintaining physiologically-relevant stimulus lengths. Stimulation frequencies from 5 to 60 Hz; all stimulations were comprised of 120 biphasic pulses of 0.2 ms width and 300 µA amplitude. To measure the effect of stimulation duration, we held stimulation frequency and current amplitude constant (20 Hz and 300 µA, respectively) and varied pulse numbers from 10-100.

Pharmacological studies investigated the role of local iGluRs on O_2 events in the striatum following PFC stimulation. A drug cocktail (50 mM AP5 and 10 mM CNQX) to antagonize NMDA, AMPA, and kainate receptors iontophoretically ejected into the dorsal striatum recording location for 60 s using cathodic current. After drug ejections ended, 10-30 s elapsed before PFC stimulation (20 Hz, 80 pulses) to measure O_2 changes under local iGluR antagonism.

Probing Local Glutamatergic Mechanisms with Iontophoresis

A multimodal sensor was placed in either the cortex or the striatum, with one barrel containing glutamate. Each probe was used for multiple locations, if background currents remained stable, both to avoid damaging tissue and minimize the number of rats. Recording locations were at least 300 µm apart (Belle et al., 2013).

Glutamate was ejected (2 s) while lowering the sensor. Locations were designated as cell locations if they produced reproducible single-unit firing that was time-locked to the glutamate ejection. We optimized the depth of cell recording locations to maximize single-unit activity in response to glutamate. Data sets were also taken at locations that were insensitive to glutamate. Each recording location data set consisted of 3-6 replicates each of baseline O_2 activity (nothing ejected) and 2 s glutamate ejections. Time between subsequent glutamate ejections was 120 s.

Histology

Following data collection, the probe location was lesioned by cyclically applying a ramp of 0 – 10 V DC potential manually three times over 20 s. Animals were sacrificed with urethane cardiac puncture. Brains were removed and fixed in 10% formalin for >7 days. Brains were then cryoprotected in 30% sucrose for >48 hrs, before coronal sections (50 µm) were taken with a

freezing microtome (Leica, Germany). Slices were mounted on microscope slides and viewed under a light microscope to confirm electrode placements.

Statistical Analyses

Statistical analysis was performed using GraphPad Prism 6 (GraphPad Software, San Diego, CA, USA). Repeated measures one-way analysis of variance (ANOVA) with post-hoc Bonferroni's test was used to evaluate significance. A Student's t-test was used to determine significance between pre- and post-drug O_2 events elicited by electrical stimulation. Differences were significant when $*P<0.05$ and $**P<0.01$.

Results

Electrical Stimulations at Glutamate Cell Bodies Evoke O_2 Response at Striatal Terminals

Glutamatergic neurons project from the PFC to medium spiny neurons (MSNs) in the striatum (Murase et al., 1993, Parent and Hazrati, 1995). We recorded O_2 changes at locations where glutamate iontophoresis elicited single-unit activity, that is, at glutamate-sensitive cells. Unit activity was evoked during the glutamate ejection and ceased upon stimulation termination. These cells were classified as MSNs, the most common neuron type in the striatum (Zhou et al., 2002), due to their high prevalence within the striatum and based on their waveform shapes. Next, we electrically stimulated the PFC to evoke glutamate release in the striatum, and recorded subsequent O_2 changes. Electrical stimulations interfered with electrophysiology, so we were unable to record cellular activity during PFC stimulations. We observed robust, reproducible O_2 responses that consisted of two distinct phases: the first, Event 1, was a decrease in O_2, followed by an overcompensating O_2 increase to above baseline, termed Event 2 (examples in Figure 4.1A-B). These biphasic responses were consistent with post-stimulus O_2 changes observed locally using amperometry at microelectrodes (Ances et al.,

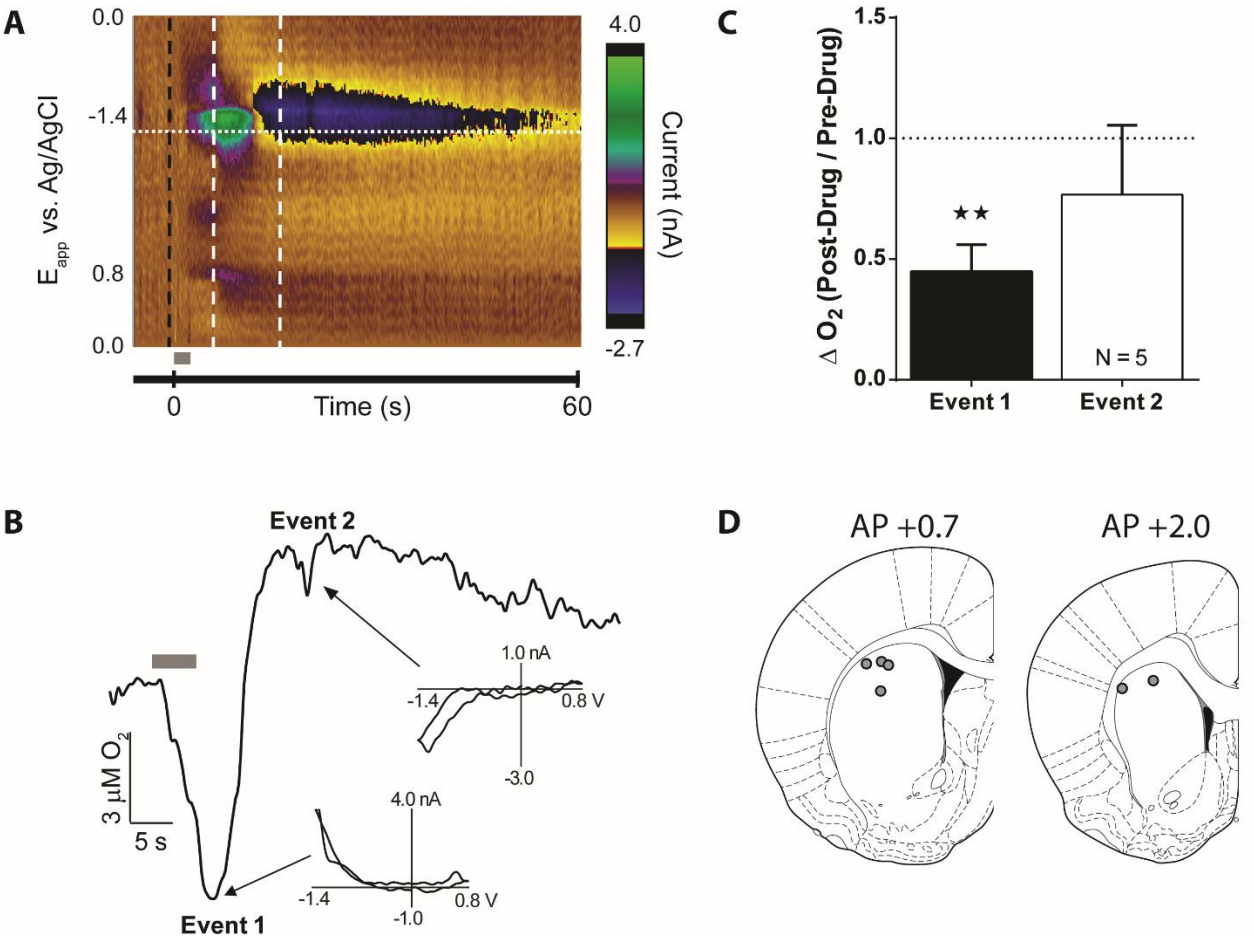

Figure 4.1. Electrically-stimulated glutamatergic cell bodies in the PFC elicit biphasic O_2 changes in the striatum. (A) Color plot representation of cyclic voltammetry data recorded around a 100 pulse, 20 Hz, 300 µA electrical stimulation as indicated by the grey bar. Abscissa: applied voltage; ordinate: acquisition time of the cyclic voltammograms. Background-subtracted currents are color coded. (B) Current taken at the reduction potential of O_2 (-1.3 V, horizontal dotted line) from A was used to determine the time course of [O_2] changes. O_2 decreases (Event 1) during the stimulation and subsequently increases above baseline (Event 2) followed electrical stimulation. Cyclic voltammograms from each event (insets) confirmed the identity of O_2, with background subtraction taken at the black dashed line in A. Slight hysteresis was attributed to concomitant endogenous ion fluctuations. (C) PFC glutamatergic cell bodies were electrically stimulated after a cocktail of AP5 (50 mM) and CNQX (10 mM) was applied at striatal terminals for 60 s. Event 1 was significantly attenuated (*P*=0.001, Student's *t*-test) under iGluR blockade. (D) Recording locations in the dorsal striatum were verified histologically (n = 6).

2001, Offenhauser et al., 2005) and globally with BOLD fMRI (Ances et al., 2001, Offenhauser et al., 2005, Hillman, 2014).

To confirm that glutamate was responsible for the biphasic O_2 response, we next iontophoresed iGluR antagonists to saturate the recording area prior to electrical stimulations. We chose a constant stimulation parameter of 80 pulses delivered at 20 Hz (Figure 4.2). After collecting a pre-drug stimulation response, we delivered both the NMDA receptor antagonist AP5 (50 mM) and the AMPA receptor antagonist CNQX (10 mM) for 60 s from a single iontophoresis barrel attached to the carbon-fiber electrode. After drug delivery, we stimulated the PFC again and compared the striatal O_2 changes before and after iGluR antagonism. In all cases, the post-stimulus O_2 decrease (Event 1) significantly diminished under local iGluR blockade ($t_{(2,8)}$=5.0, P=0.001, n=5) to 44.8 ± 11.1% of pre-drug values, while Event 2 was unaffected (Figure 4.1C). This confirmed that endogenous glutamate release evoked by PFC stimulation in the striatum resulted in post-stimulation O_2 decreases that were partially due to iGluR activation.

Biphasic O_2 Responses Depend on Electrical Stimulation Parameters

We next investigated the dependence of the observed O_2 events on the stimulation parameters to explore what stimulus was sufficient to elicit a biphasic response. First, we kept stimulation frequencies and amplitudes constant at 20 Hz and 300 µA, respectively, and changed the number of stimulation pulses from 10 – 100 pulses (Figure 4.2A). The number of locations that responded with biphasic O_2 changes increased with the number of stimulus pulses (Figure 4.2B). Furthermore, the relationship was linear between both biphasic event amplitudes and the corresponding number of stimulation pulses (Event 1: R^2=0.990; Event 2: R^2=0.975, Figure 4.2C). All O_2 responses from 10 pulse stimulations were monophasic, so we omitted these data from the linear fit. This both confirmed that both mono- and biphasic O_2

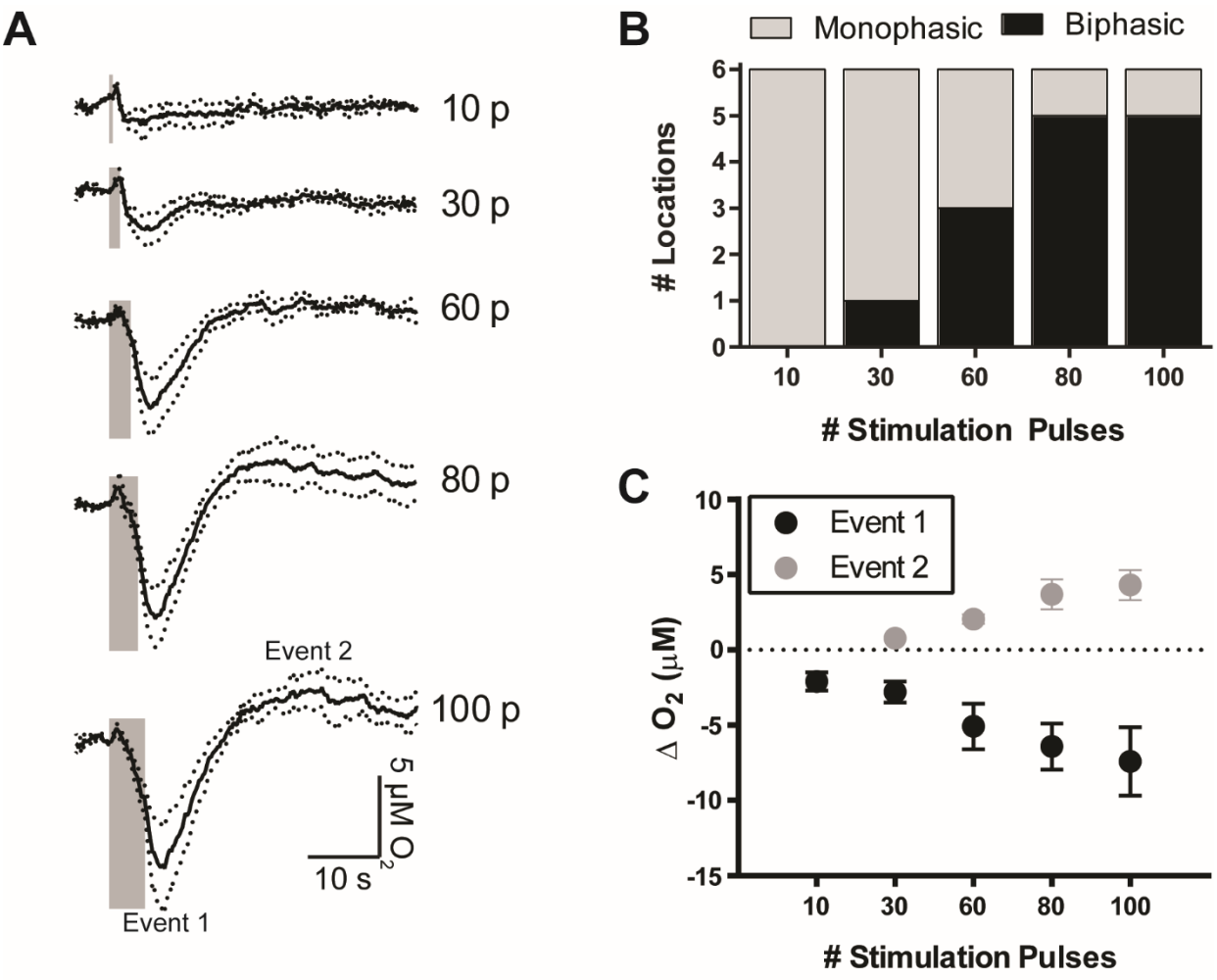

Figure 4.2. PFC electrical stimulations controlled the biphasic O_2 response in the striatum through the number of applied stimulation pulses. (A) Current traces taken at the O_2 reduction potential were averaged (n=6). The number of electrical stimulation pulses (p) used are indicated to the right of the traces. Stimulation frequency and amplitude were held constant at 20 Hz, and 300 μA, respectively. Grey bars indicate stimulation durations. Dotted lines indicate ± SEM. (B) The relative occurrence of biphasic O_2 responses to electrical stim increased with the number of stimulus pulses. (C) Post-stimulus minima (Event 1) and maxima (Event 2) increased linearly (Event 1: R^2=0.990; Event 2: R^2=0.975) with the number of stimulus pulses. Monophasic data (i.e., decreased O_2 responses that did not return to baseline within 60 s) were excluded from plotted Event 2 points. Error bars indicate ± SEM.

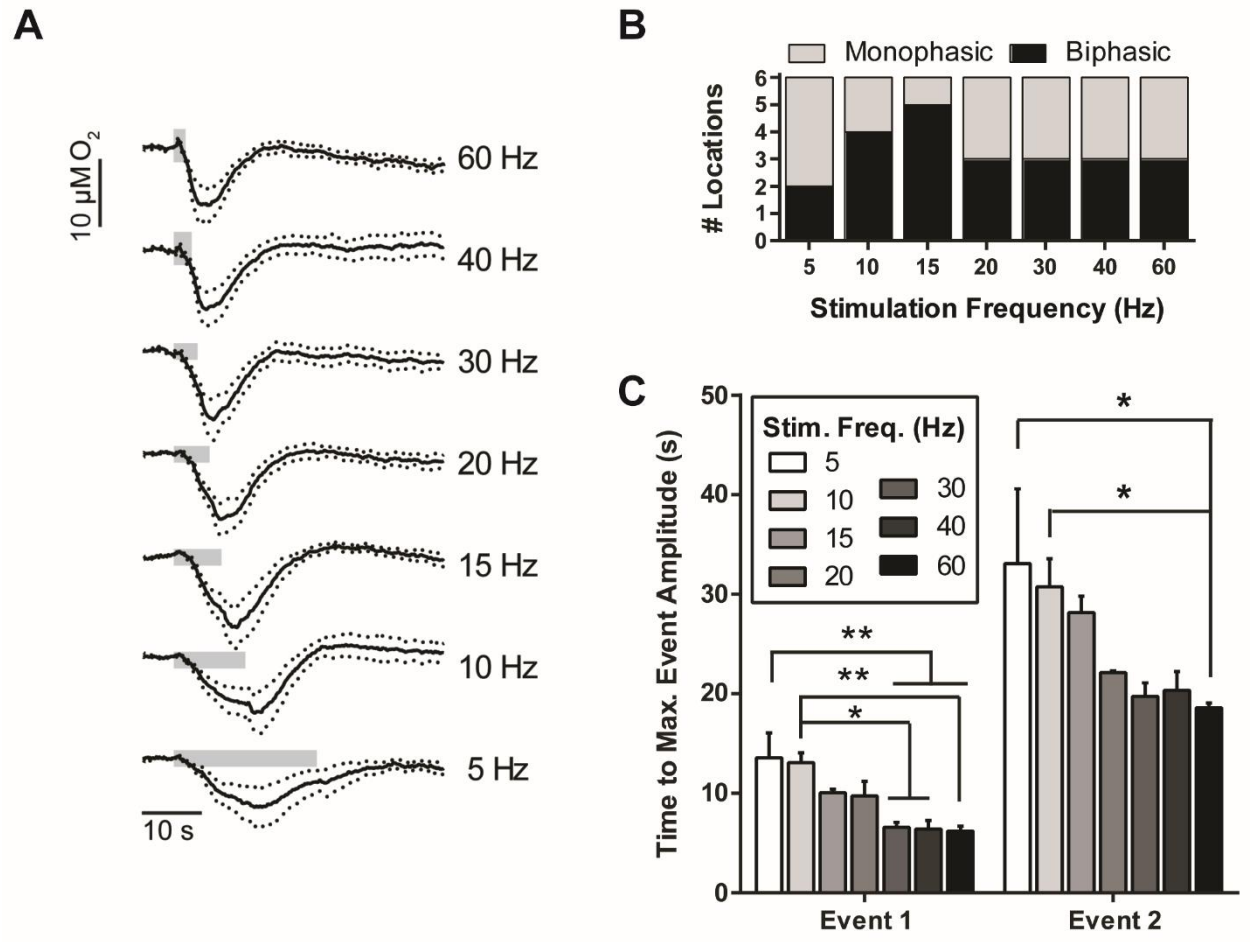

Figure 4.3. PFC stimulation frequencies affected the time to reach minimal O_2 decreases (i.e., Event 1) and subsequent maximal O_2 increases (i.e., Event 2) in the dorsal striatum. (A) Current traces taken at the O_2 reduction potential were averaged (n = 6), with their respective stimulation frequencies indicated to the right. The number of biphasic pulses applied and their amplitudes were kept constant (80 pulses and 300 µA, respectively). Grey bars indicate stimulation durations. Dotted lines indicate ± SEM. (B) Stimulus frequency did not affect whether or not the responses were biphasic. (C) The stimulus frequency affected the time to reach maximum Event 1 O_2 decreases and the subsequent Event 2 O_2 increases. Monophasic O_2 responses were excluded from Event 2 statistics. Error bars indicate ± SEM. Significance was determined with repeated measures one-way ANOVA and Bonferroni's post-hoc test. **P*<0.05, ***P*<0.01

responses can be elicited at the same location, identified that the response type depends on a pulse-dependent stimulus threshold, and showed a strong linear relationship between the number of stimulation pulses and the resulting O_2 event amplitudes.

To ensure that the pulse-dependent stimulus effects were not caused by an increase in total stimulation length, we kept pulse numbers and amplitude constant (120 pulses and 300 μA, respectively) and tested 5 – 60 Hz frequencies. These frequencies did not affect either Event 1 or Event 2 (when applicable) amplitudes (repeated measures one-way ANOVA, Bonferroni's post-hoc, $P>0.05$), or influence whether responses were mono- or biphasic (Figure 4.3A-B). However, longer stimulation times significantly increased the time differences between stimulation and maximum O_2 changes for each event, relative to faster stimulations (one-way ANOVA, Event 1: $F_{(6,53)}=6.26$, $P=0.0002$; Event 2: $F_{(6,35)}=5.47$, $P=0.003$; Figure 4.3C). Bonferroni post-hoc analysis revealed significant differences in Event 1 minima times between both 5 Hz and 10 Hz stimulations as compared to higher stimulation frequencies (5 Hz: 13.6 ± 2.5 s; 10 Hz: 13.1 ± 1.0 s; 30 Hz: 6.5 ± 0.5 s; 40 Hz: 6.4 ± 0.8 s; and 60 Hz: 6.2 ± 0.5 s; 5 Hz versus 30, 40 and 60 Hz: $P<0.01$ each, n=6 each; 10 Hz versus 30 and 40 Hz: $P<0.05$ each; 10 Hz versus 60 Hz: $P<0.01$, n=6 each, Figure 4.3C). Time differences between stimulation and Event 2 maxima (when present) also increased from 5 Hz and 10 Hz stimulation frequencies to 60 Hz (5 Hz: 33.1 ± 7.5 s, n=2; 10 Hz: 30.8 ± 2.8 s, n=4; 60 Hz: 18.6 ± 0.5 s; 5 Hz and 10 Hz versus 60 Hz: $P<0.05$ each, Figure 4.3C). These findings indicated that longer stimulus frequencies increased the timespan between electrical stimulus and both Event 1 minima and Event 2 maxima, without affecting event magnitudes.

Glutamate Iontophoresis Provokes Local Single-Cell Firing and O_2 Consumption

To exclude the confounding effects of non-specific neurotransmitters released from electrical stimulation, we next delivered glutamate directly to the recording locations.

Experiments started in the somatosensory cortex as proof of principle, then extended deeper within the brain through the striatum. We ejected glutamate from an iontophoresis barrel in 2 s pulses as the electrode lowered, until electrophysiology could resolve single-unit firing from background noise at the carbon fiber (Figure 4.4A and 4.4C). Cortical cells required >100 nA cathodic current to respond, and were most often found at or below 0.9 mm D-V, corresponding to the most densely populated layers IV – VIb. These observations were consistent with published observations (Krnjević and Phillis, 1963, Dykes and Lamour, 1988, Lamour et al., 1988), which validated our approach to locally excite cells with iontophoresed glutamate.

Next, we advanced our experiments into the striatum to investigate differences between the role of glutamate between superficial and deep brain environments. Striatal cells were denser in the ventral striatum as compared to the dorsal striatum (Meitzen et al., 2011) and responded using <80 nA ejection currents, less than the ejection currents required for cortical cells (Krnjević and Phillis, 1963) and consistent with previous reports (Kiyatkin and Rebec, 1996). Cells required different glutamate ejection currents between and within both brain regions, either due to differences in barrel characteristics, distance of the cell to the drug barrel, cell sensitivity to glutamate, or the available excitatory receptor populations (Lamour et al., 1988). However, the consistent difference between the ejection currents required to elicit cell firing established that glutamate sensitivities differed between the cortex and striatum.

We used FSCV to record O_2 changes during glutamate iontophoresis and simultaneous single-unit activity recording. In contrast to electrical stimulations, we observed one of two effects in recorded environments following glutamate iontophoresis: either an exclusive monophasic O_2 decrease (i.e., Event 1 not followed by Event 2) or negligible O_2 changes (Figure 4.4). The monophasic O_2 decreases returned to baseline within 20 s (Figure 4.4A-B). This contradicted a previous study that found a robust O_2 increase following local glutamate pressure ejection (Lourenço et al., 2014), despite that they delivered 0.5 nmol over 1 s versus

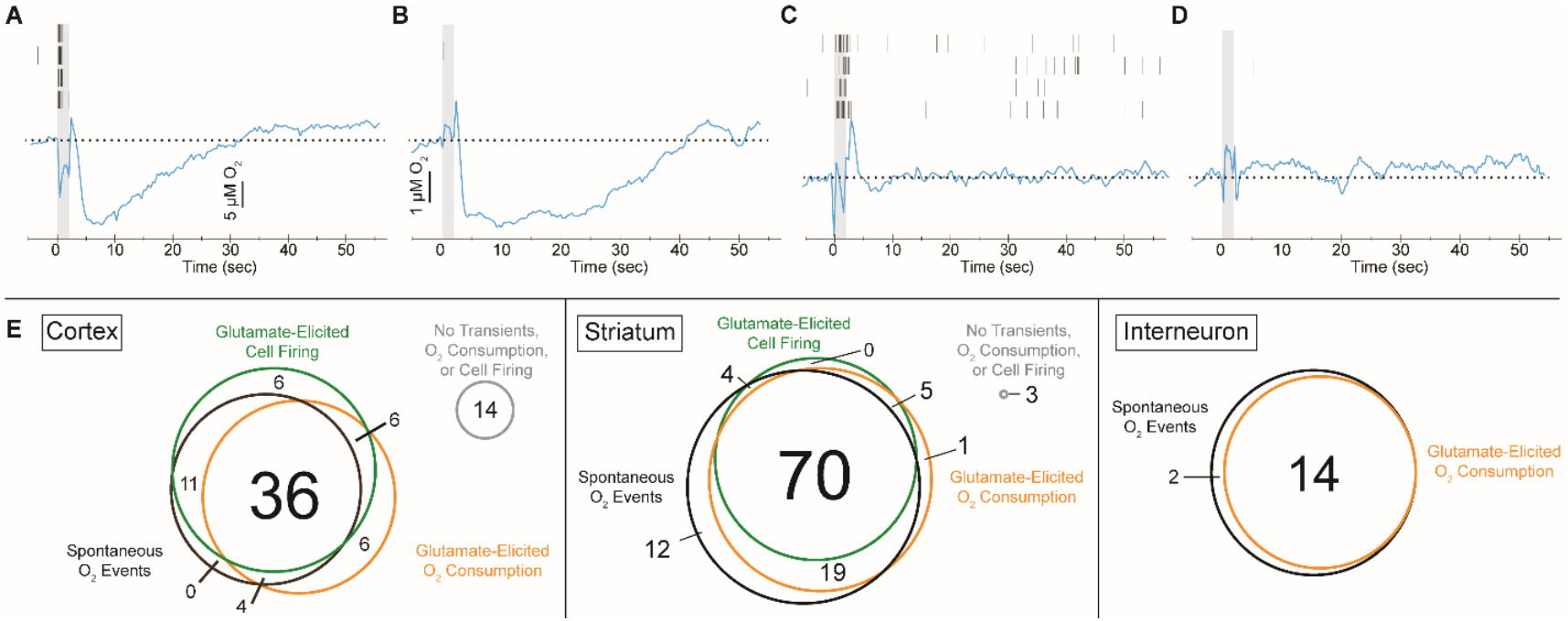

Figure 4.4. Carbon fiber electrodes detected a variety of microenvironments that respond differently to glutamatergic excitation. (A-D) Recording locations fell into one of two broad categories: those that responded to glutamate with excitatory single-unit activity (A, C) and those that did not (B, D). Within each group, glutamate ejections were either succeeded by an O_2 decrease (A, B) or experienced no change in O_2 relative to baseline (C, D). Black tics indicate action potentials for each of the four collected trials shown. Grey boxes indicate the glutamate ejection duration. O_2 traces were taken at the O_2 reduction potential. B, C, and D share the same scale bar. (E) Differences existed between overlapping spontaneous O_2 events, neuronal sensitivity to glutamate, and provoked O_2 changes in the cortex, striatum (excluding interneurons), and interneuron locations.

an estimated value on the order of picomoles delivered via iontophoresis ejection over 2 s at our chosen ejection currents (Kirkpatrick et al., 2014). Overall, our sensor recorded one of four responses to glutamate at any given location, either with or without cell firing and succeeded by either O_2 consumption or no O_2 changes (Figure 4.4), depending on natural heterogeneity.

Glutamate Inhibits Interneuron Activity

While characterizing glutamate responsive neurons in the striatum, we serendipitously observed interneurons in ventral locations, offering us the unique opportunity to study them *in vivo*. These cells represent only 1-3% of striatal neurons (Zhou et al., 2002), and were confirmed as interneurons by their high spontaneous firing rate and single-unit waveform. Our carbon-fiber microelectrodes recorded 1-3 interneurons per recording location (Figure 4.5A-B), consistent with clusters observed by others (Alcantara et al., 2003). They spontaneously fired between 10-25 Hz in deeply anesthetized subjects, higher than in previously reported studies (Zhou et al., 2002, Witten et al., 2010). Locally ejecting glutamate significantly inhibited, rather than augmented, single-unit firing rates (35.8 ± 5.5% of baseline single-unit activity, $t_{(2,24)}$=11.5, P<0.0001, Figure 4.5B-C), and fully extinguished firing with extended ejection times (Figure 4.5B). Basal firing rates recovered after glutamate ejections ceased (Figure 4.5B). To our knowledge, we are the first to show this explicit chemical relationship between interneurons and glutamate *in vivo*.

Transient O_2 Events

Finally, while characterizing glutamate responses in both cortical and striatal environments, we also observed spontaneous, discrete O_2 changes throughout both regions (Figure 4.6). These transient O_2 events occurred without concurrent cell activity, presented during baseline recordings in absence of glutamate, and persisted throughout data collections

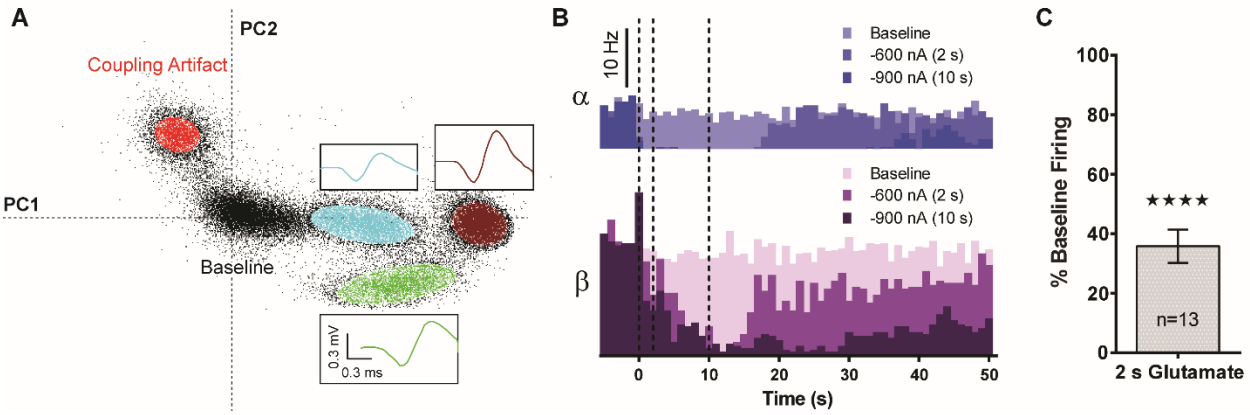

Figure 4.5. Interneurons observed in the ventral striatum. (A) A 2D waveform density plot distinguished a cluster of three interneurons firing at a single carbon fiber in one location, each resolved from the background. Typical interneuron firing rates (>10 Hz) produced large, dense clusters. Color-coded average action potential waveforms, with outliers >4 σ removed, are shown above their respective cluster. (B) Firing rate histograms for two interneurons (α and β as blue and purple, respectively), recorded at a different location than shown in A. The firing rate of both cells attenuated during glutamate ejections and recovered after the ejections ended. The dashed lines from left to right represent the start of ejection, end of the 2 s ejection, and end of the 10 s ejection. (C) A 2 s glutamate ejection, normalized to the spontaneous firing exhibited by these cells, had a powerful inhibitory effect on interneurons in the ventral striatum (Student's t-test: $t_{(2,12)} = 11.51$, $P < 0.0001$).

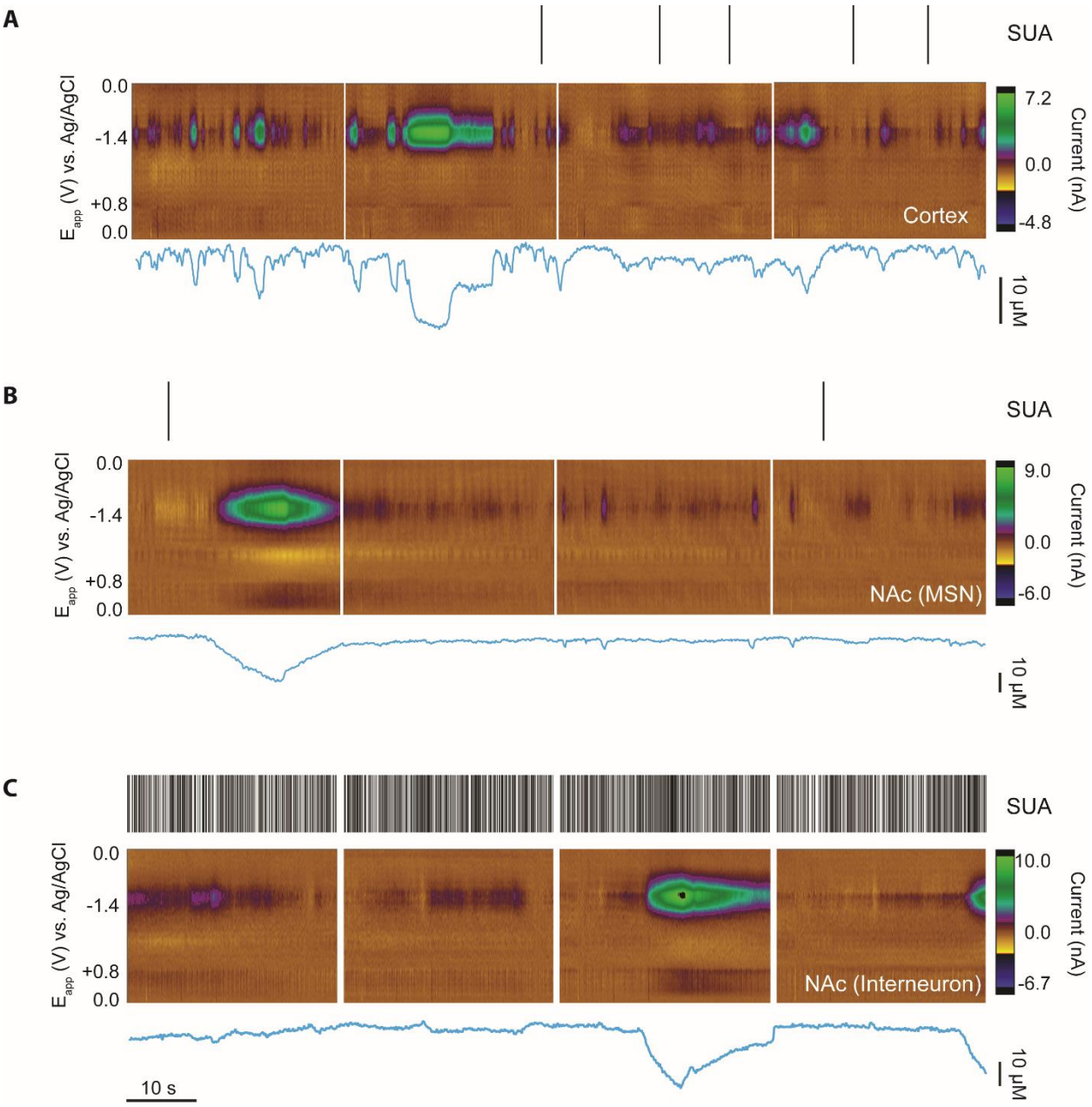

Figure 4.6. Recording locations exhibited spontaneous O_2 transients. (A) A layer Vb cortical cell. (B) An MSN in the striatum. (C) An interneuron in the ventral striatum. Each black hash (top) indicates a single recorded action potential. Discrete O_2 events presented alone, devoid of other electrochemical signals (color plots, middle). Current traces (bottom) were obtained by setting the background current such that all events were O_2 consumption / positive current deflection events for consistency. Both cortical and striatal recording locations presented with either short, punctuated transients (i.e., A), large, extended transients (i.e., C), or a mixture of both (i.e., B).

unaffected by glutamate ejections. The overlapping relationships between these transients and glutamate-stimulated O_2 decreases and single-unit activity between cortical and striatal environments are summarized in Figure 4.4E. Interestingly, 90.0% of all recorded locations with glutamate-sensitive cells presented with spontaneous O_2 transients. These transients appeared in 93.7% of striatal, glutamate-sensitive recording locations (excluding interneurons) and 88.6% of locations insensitive to glutamate (Figure 4.4E). Spontaneous O_2 transients presented at 80.8% of glutamate-sensitive cortical cell locations, but only 54.8% of glutamate-insensitive locations (Figure 4.4E). These data revealed a high probability of observing spontaneous O_2 fluctuations in close proximity to glutamate-sensitive neurons, especially in subcortical brain matter, but further studies are needed to determine their significance.

Discussion

In this study, we extended the use of an existing multimodal sensor to investigate the relationship between neuronal activity and O_2 consumption in highly-localized environments. We assessed the differences between stimulated (non-specific) and iontophoresed (specific) glutamate responses. Endogenous glutamate release via electrical PFC stimulation elicited a biphasic O_2 pattern in the striatum, first decreasing and then increasing above baseline levels, consistent with the idea that O_2 is first locally consumed (Event 1) following neurotransmission before being replenished via CBF increases (Event 2) (Ances et al., 2001, Offenhauser et al., 2005, Hillman, 2014). Interestingly, we did not observe dopamine release at the sensor, though this has been reported in the ventral striatum (Murase et al., 1993). Activation of striatal iGluRs was responsible for the magnitude of O_2 consumption, but did not affect O_2 compensation (i.e., CBF). Local O_2 responses to glutamate iontophoresis resembled those from weak electrical stimulations, monophasic O_2 decreases that were insufficient to provoke CBF-driven increases in O_2. Taken together, it is clear that our improved multimodal sensor provides a chemically and

spatially selective method of studying glutamatergic influence on single-unit activity and local O_2 coupling throughout the brain *in vivo*.

Here, we stimulated glutamatergic cell bodies in the PFC to measure O_2 changes at terminals in the dorsal striatum. Typical electrical stimulation paradigms use biphasic pulses and optimize stimulation parameters through tuning curves (Mathiesen et al., 1998, Nielsen and Lauritzen, 2001, Offenhauser et al., 2005, Hoffmeyer et al., 2007). Studies have reported that below a threshold stimulation "strength," both O_2 decreases and cell firing occurred without evoking CBF changes (Nielsen and Lauritzen, 2001, Offenhauser et al., 2005). We reproduced this phenomenon using glutamatergic PFC projections to the striatum and identified "strength" related to the number of stimulating pulses. The event amplitudes grew linearly with the number of stimulation pulses, as did the likelihood of the location responding with a biphasic O_2 pattern (i.e., first consuming O_2, then receiving O_2 increases above baseline). Together, these results support current functional hyperemia dogma that increasing neuronal activity leads to increases in energy consumption and subsequent CBF increases to deliver overcompensating amounts of O_2.Thus, we verified that a stimulation threshold must be exceeded to elicit hyperemic O_2 responses, and identified that the threshold directly depends upon the number of stimulus pulses.

In contrast to previous studies that show both CBF and neuronal activity as dependent upon stimulation frequency (Mathiesen et al., 1998, Nielsen and Lauritzen, 2001, Offenhauser et al., 2005, Hoffmeyer et al., 2007), we found no relationship between faster stimulation frequencies and whether or not the locations expressed biphasic behavior. It is important to note that each of these studies kept the stimulation duration constant while modulating the frequency, which would confound the effects of frequency with that of the pulse numbers per stimulus. Further, we found no relationship between the event amplitudes and frequency, which we attribute to using the same number of pulses. Slowing the stimulation frequency only lengthened the amount of time between the stimulation and the maximal O_2 event responses,

which again supported our conclusion that it is the number of pulses that ultimately controls the magnitude of O_2 responses. Thus, we conclude that frequency has no influence over hyperemia as it relates to PFC stimulations recorded in the striatum.

Event 2 was insensitive to localized iGluR blockade at the cell terminals (Figure 4.1C), consistent with studies that related neurovascular coupling to postsynaptic receptor activity (Nielsen and Lauritzen, 2001, Iordanova et al., 2015). This suggests that O_2 overcompensation (i.e., CBF) at striatal terminals stems from activity-dependent, PFC neurotransmission. As a sufficient quantity of stimulation pulses was necessary to provoke Event 2, the species responsible either required robust, accumulative stimulations to activate or recruited a larger population of excited cells. However, the lack of specificity offered by electrical stimulation precluded any conclusions about whether this hyperemic relationship depended more on neuronal consumption of energy or the release of specific neurotransmitters.

It is well known that electrical stimulations excite spatially-extensive cell populations, so we adapted an existing multimodal sensor to excite local neuronal populations, record action potentials, and observe subsequent O_2 changes. Delivering glutamate through iontophoresis at a carbon-fiber microelectrode evoked single-unit activity in highly-localized cell populations, in agreement with previous studies (Krnjević and Phillis, 1963, Lamour et al., 1988). Nearly all recorded locations (100+) showed either no O_2 changes following a brief (2 s) glutamate ejection or a monophasic O_2 decrease that returned to baseline (Figure 4.4). The exclusive presence of Event 1 following local excitation mirrored a “weak” electrical stimulus, but could not elicit biphasic responses even with ejection currents >500 nA (data not shown). Previous work in our lab established how to both quantify the amount of ejected drug and track its spatial diffusion (Kirkpatrick et al., 2014, Kirkpatrick and Wightman, 2016), which we used to confirm that a 2 s ejection released glutamate on the order of pmol despite the 200 mM barrel concentration. This quantity is unlikely to be excitotoxic (Choi, 1988), which establishes glutamate iontophoresis as a safe method of investigating local stimulation dynamics. However,

this concentration is likely too low to diffuse to a sufficient number of neurons to match the stimulation strength necessary to elicit a biphasic response, especially with the efficiency of glutamate uptake through neuronal and astrocytic transporters (Rothstein et al., 1996).

Cell firing is normally inhibited in deeply anaesthetized animals; however, we observed highly-active interneurons in the ventral striatum. We could not characterize whether these interneurons were cholinergic or GABAergic based on electrophysiological recordings alone (Kawaguchi, 1993). Through iontophoresis, we discovered that glutamate significantly and reversibly inhibited, rather than excited, interneuron firing rates. Other studies have shown contrary relationships between MSN and cholinergic interneuron activity *in vivo* (Zhou et al., 2002, Witten et al., 2010). The specific glutamatergic inhibition of these interneurons adds to the growing body of literature investigating the complex interactivity between glutamate, dopamine, and acetylcholine through striatal MSNs and interneurons (Gras et al., 2002, Alcantara et al., 2003, Surmeier et al., 2007).

Spontaneous O_2 events, found here in both the cortex and striatum, were observed *in vivo* as early as 1957 (Davies and Bronk, 1957). One study reported that adenosine, a vasoactive neurotransmitter, synchronized with a percentage of O_2 transients in the dorsal striatum (Wang and Venton, 2016). Studies attributed these spontaneous events to factors ranging from the type of anesthetic used (Hudetz et al., 1998) to spontaneous astrocytic excitation (Volterra and Meldolesi, 2005, Khakh and Sofroniew, 2015), among other possibilities. Studies detecting O_2 using amperometry showed baseline current fluctuations, (Lowry et al., 2010) and other works by Lowry et al., but the unique cyclic voltammogram shape allowed us to confirm what may be mistaken for noise as O_2 (examples shown in Figure 4.1B). Though some transients were large (>20 μM), the short (<60 s) durations, continued sensitivity to glutamate excitation, and lack of concomitant ionic signals precluded these from representing spreading depolarization events (Ayata and Lauritzen, 2015). The larger percentage of transients observed in deeper brain regions indicated an environmental factor to their presence,

though we did not investigate any underlying chemical or physical source(s). When glutamate was ejected during a transient event, we observed augmented O_2 decreases that relaxed on the same time scale as those not confounded by transients, indicating that the spontaneous events throughout the brain are unlikely to be competing with glutamate-receptor-dependent O_2 consumption. Our measurements indicated that spontaneous O_2 events did not correspond with single-unit firing, but the large overlap between the presence of transients and glutamate sensitive neurons could make multi-unit cellular recording a future topic of exploration.

Conclusions

As technology progresses to stimulate the brain more selectively and specifically, increasing evidence suggests that disconnects between cerebrovascular coupling relationships exist in healthy subjects. Here, we elicited a hyperemic response from electrically stimulated glutamate release in the striatum, but targeted exogenous glutamate excitation produced only decreases in recorded O_2. Modifying an existing multimodal sensor that pairs iontophoresis with electrophysiology and FSCV permitted the simultaneous detection of highly localized O_2 and cell firing responses to selective glutamatergic stimuli in an intact animal. This technique serves as a starting point for investigating spatially-targeted cerebrovascular coupling as it relates to glutamate-elicited neuronal spiking and O_2 consumption.

REFERENCES

Alcantara AA, Chen V, Herring BE, Mendenhall JM, Berlanga ML (2003) Localization of dopamine D2 receptors on cholinergic interneurons of the dorsal striatum and nucleus accumbens of the rat. *Brain Res* **986**:22-29.

Ances BM, Buerk DG, Greenberg JH, Detre JA (2001) Temporal dynamics of the partial pressure of brain tissue oxygen during functional forepaw stimulation in rats. *Neurosci Lett* **306**:106-110.

Ayata C, Lauritzen M (2015) Spreading depression, spreading depolarizations, and the cerebral vasculature. *Physiol Rev* **95**:953-993.

Belle AM, Owesson-White C, Herr NR, Carelli RM, Wightman RM (2013) Controlled iontophoresis coupled with fast-scan cyclic voltammetry/electrophysiology in awake, freely moving animals. *ACS Chem Neurosci* **4**:761-771.

Bucher ES, Fox ME, Kim L, Kirkpatrick DC, Rodeberg NT, Belle AM, Wightman RM (2014) Medullary norepinephrine neurons modulate local oxygen concentrations in the bed nucleus of the stria terminalis. *J Cereb Blood Flow Metab* **34**:1128-1137.

Choi DW (1988) Glutamate neurotoxicity and diseases of the nervous system. *Neuron* **1**:623-634.

Davies P, Bronk D (1957) Oxygen tension in mammalian brain. In: Fed Proc, vol. 16, p 689.

Drake CT, Iadecola C (2007) The role of neuronal signaling in controlling cerebral blood flow. *Brain Lang* **102**:141-152.

Dykes R, Lamour Y (1988) An electrophysiological study of single somatosensory neurons in rat granular cortex serving the limbs: a laminar analysis. *J Neurophysiol* **60**:703-724.

Gras C, Herzog E, Bellenchi GC, Bernard V, Ravassard P, Pohl M, Gasnier B, Giros B, El Mestikawy S (2002) A third vesicular glutamate transporter expressed by cholinergic and serotoninergic neurons. *J Neurosci* **22**:5442-5451.

Hillman EM (2014) Coupling mechanism and significance of the BOLD signal: a status report. *Annu Rev Neurosci* **37**:161.

Hoffmeyer HW, Enager P, Thomsen KJ, Lauritzen MJ (2007) Nonlinear neurovascular coupling in rat sensory cortex by activation of transcallosal fibers. *J Cereb Blood Flow Metab* **27**:575-587.

Hudetz A, Biswal B, Shen H, Lauer K, Kampine J (1998) Spontaneous fluctuations in cerebral oxygen supply. In: Oxygen Transport to Tissue XX, pp 551-559: Springer.

Iordanova B, Vazquez AL, Poplawsky AJ, Fukuda M, Kim S-G (2015) Neural and hemodynamic responses to optogenetic and sensory stimulation in the rat somatosensory cortex. *J Cereb Blood Flow Metab* **35**:922-932.

Kawaguchi Y (1993) Physiological, morphological, and histochemical characterization of three classes of interneurons in rat neostriatum. *J Neurosci* **13**:4908-4923.

Khakh BS, Sofroniew MV (2015) Diversity of astrocyte functions and phenotypes in neural circuits. *Nat Neurosci* **18**:942-952.

Kirkpatrick DC, Edwards MA, Flowers PA, Wightman RM (2014) Characterization of solute distribution following iontophoresis from a micropipet. *Anal Chem* **86**:9909-9916.

Kirkpatrick DC, Wightman RM (2016) Evaluation of Drug Concentrations Delivered by Microiontophoresis. *Anal Chem*.

Kiyatkin EA, Rebec GV (1996) Dopaminergic modulation of glutamate-induced excitations of neurons in the neostriatum and nucleus accumbens of awake, unrestrained rats. *J Neurophysiol* **75**:142-153.

Krnjević K, Phillis J (1963) Iontophoretic studies of neurones in the mammalian cerebral cortex. *J Physiol* **165**:274.

Lamour Y, Dutar P, Jobert A, Dykes R (1988) An iontophoretic study of single somatosensory neurons in rat granular cortex serving the limbs: a laminar analysis of glutamate and acetylcholine effects on receptive-field properties. *J Neurophysiol* **60**:725-750.

Lourenço CF, Santos RM, Barbosa RM, Cadenas E, Radi R, Laranjinha J (2014) Neurovascular coupling in hippocampus is mediated via diffusion by neuronal-derived nitric oxide. *Free Radical Biol Med* **73**:421-429.

Lowry JP, Griffin K, McHugh SB, Lowe AS, Tricklebank M, Sibson NR (2010) Real-time electrochemical monitoring of brain tissue oxygen: a surrogate for functional magnetic resonance imaging in rodents. *NeuroImage* **52**:549-555.

Mathiesen C, Caesar K, Akgören N, Lauritzen M (1998) Modification of activity-dependent increases of cerebral blood flow by excitatory synaptic activity and spikes in rat cerebellar cortex. *J Physiol* **512**:555-566.

Meitzen J, Pflepsen KR, Stern CM, Meisel RL, Mermelstein PG (2011) Measurements of neuron soma size and density in rat dorsal striatum, nucleus accumbens core and nucleus accumbens shell: differences between striatal region and brain hemisphere, but not sex. *Neurosci Lett* **487**:177-181.

Mintun M, Shulman G, Snyder A, Raichle M (2000) Cerebral blood flow during regional activation is not regulated to maintain oxygen delivery. *J Neurosci* **26**:645.611.

Murase S, Grenhoff J, Chouvet G, Gonon FG, Svensson TH (1993) Prefrontal cortex regulates burst firing and transmitter release in rat mesolimbic dopamine neurons studied in vivo. *Neurosci Lett* **157**:53-56.

Nicola SM, Surmeier DJ, Malenka RC (2000) Dopaminergic modulation of neuronal excitability in the striatum and nucleus accumbens. *Annu Rev Neurosci* **23**:185-215.

Nielsen AN, Lauritzen M (2001) Coupling and uncoupling of activity-dependent increases of neuronal activity and blood flow in rat somatosensory cortex. *J Physiol* **533**:773-785.

Offenhauser N, Thomsen K, Caesar K, Lauritzen M (2005) Activity-induced tissue oxygenation changes in rat cerebellar cortex: interplay of postsynaptic activation and blood flow. *J Physiol* **565**:279-294.

Ogawa S, Lee T-M, Kay AR, Tank DW (1990) Brain magnetic resonance imaging with contrast dependent on blood oxygenation. *Proc Natl Acad Sci U S A* **87**:9868-9872.

Parent A, Hazrati L-N (1995) Functional anatomy of the basal ganglia. I. The cortico-basal ganglia-thalamo-cortical loop. *Brain Res Rev* **20**:91-127.

Powers WJ, Hirsch IB, Cryer PE (1996) Effect of stepped hypoglycemia on regional cerebral blood flow response to physiological brain activation. *Am J Physiol Heart Circ Physiol* **270**:H554-H559.

Rothstein JD, Dykes-Hoberg M, Pardo CA, Bristol LA, Jin L, Kuncl RW, Kanai Y, Hediger MA, Wang Y, Schielke JP (1996) Knockout of glutamate transporters reveals a major role for astroglial transport in excitotoxicity and clearance of glutamate. *Neuron* **16**:675-686.

Roy CS, Sherrington CS (1890) On the regulation of the blood-supply of the brain. *J Physiol* **11**:85.

Sokoloff L (1989) Circulation and energy metabolism of the brain.

Surmeier DJ, Ding J, Day M, Wang Z, Shen W (2007) D1 and D2 dopamine-receptor modulation of striatal glutamatergic signaling in striatal medium spiny neurons. *Trends Neurosci* **30**:228-235.

Takmakov P, McKinney CJ, Carelli RM, Wightman RM (2011) Instrumentation for fast-scan cyclic voltammetry combined with electrophysiology for behavioral experiments in freely moving animals. *Rev Sci Instrum* **82**:074302.

Thompson JK, Peterson MR, Freeman RD (2003) Single-neuron activity and tissue oxygenation in the cerebral cortex. *Science* **299**:1070-1072.

Volterra A, Meldolesi J (2005) Astrocytes, from brain glue to communication elements: the revolution continues. *Nat Rev Neurosci* **6**:626-640.

Wang Y, Venton BJ (2016) Correlation of transient adenosine release and oxygen changes in the caudate-putamen. *J Neurochem*.

Witten IB, Lin S-C, Brodsky M, Prakash R, Diester I, Anikeeva P, Gradinaru V, Ramakrishnan C, Deisseroth K (2010) Cholinergic interneurons control local circuit activity and cocaine conditioning. *Science* **330**:1677-1681.

Zhou FM, Wilson CJ, Dani JA (2002) Cholinergic interneuron characteristics and nicotinic properties in the striatum. *J Neurobiol* **53**:590-605.

Zimmerman JB, Wightman RM (1991) Simultaneous electrochemical measurements of oxygen and dopamine in vivo. *Anal Chem* **63**:24-28.

CHAPTER 5: GLUTAMATE RECEPTOR ROLES IN LOCALIZED COUPLED AND DECOUPLED SINGLE-UNIT FIRING AND O_2 RELATIONSHIPS BETWEEN THE CORTEX AND NUCLEUS ACCUMBENS

Introduction

Regional increases in cerebral blood flow (CBF) maintain energetic homeostasis during neuronal activity in a process known as neurovascular coupling (Attwell et al., 2010). Glutamate is ubiquitous throughout the brain and is the primary excitatory neurotransmitter responsible for synaptic neurotransmission. Glutamate receptors are present on glial cells and both pre- and post-synaptic neurons, providing multiple pathways through which glutamate can influence neurovascular coupling. Dysregulated glutamatergic receptor function has been implicated in numerous pathologies including Huntington's (Cowan and Raymond, 2006), schizophrenia (Olney and Farber, 1995), and many others (Meldrum, 2000, Niswender and Conn, 2010, Paoletti et al., 2013). Interestingly, these same disease states are associated with dysregulated CBF (Zlokovic, 2011). Although glutamate is known to contribute to neurovascular coupling through its different receptors (Attwell et al., 2010), the precise mechanisms of this influence are poorly understood.

A growing number of brain functionality studies use blood oxygen level dependent (BOLD) functional magnetic resonance imaging (fMRI), which measures shifts in oxygenated and deoxygenated blood that depend on CBF changes (Ogawa et al., 1990). However, data interpretation is the subject of much debate since fMRI infers neuronal activity based on hemodynamic signals. Although this is valid when neurovascular coupling is conserved, it may not apply to comparisons between brain regions where coupling is modulated differently (Ances et al., 2008, Sloan et al., 2010). Additionally, the poor spatial resolution (~1-2 mm) homogenizes

signals within brain regions that differ locally. Glutamate receptors express differentially throughout the brain at a local level (Petralia et al., 1996), and signal averaging at this scale may not be appropriate for studying the influence of these receptors in neurovascular coupling. Finally, these studies are “functional” studies by definition, meaning that they differentiate brain activity during task performance, or following peripheral or electrical stimulations. These stimuli are not selective, and off-target effects may confound data interpretation. Therefore, to study glutamatergic influence on neurovascular coupling requires a technique that can eliminate the off-target effects of nonselective stimuli as well as address the differential distribution of receptor types within and between brain regions.

Herein we expound upon previous work using a multimodal sensor to reveal definitively that glutamate, acting through specific receptors, affects coupling between single-unit activity and O_2 consumption in the somatosensory cortex and the nucleus accumbens (NAc). First, we antagonized ionotropic glutamate receptors (iGluRs) and found that in both regions, α-amino-3-hydroxy-5-methylisoxazole-4-propionic acid and kainate receptor (AMPARs collectively) antagonism decoupled neuronal activity and O_2, whereas N-methyl-D-aspartic acid receptor (NMDAR) antagonism maintained this relationship. Next, we assessed the impact of metabotropic glutamate receptors (mGluRs), comparing the use of iGluR antagonists and an mGluR agonist. Both the cortex and NAc had coupled and decoupled responses between these two treatments. Furthermore, we inhibited nitric oxide synthase (NOS), which diminished responses and maintained coupling in the cortex but showed nNOS-specific decoupled responses in the NAc. Taken together, our data show that activated glutamate receptors exert differential effects on single-unit activity and O_2 changes between and within different brain regions at high spatial resolutions, which is an important consideration in the interpretation of fMRI data.

Experimental

Animal Care

All animal protocols were approved by the Institutional Animal Care and Use Committee of the University of North Carolina at Chapel Hill (UNC). Sprague-Dawley rats (adult males, 300 – 450 g, Charles River, Wilmington, MA, USA) were pair-housed in UNC animal facilities on a 12 hour light/dark cycle and given food and water *ad libitum*. Care was taken to reduce the number of animals used and minimize their suffering. A total of 50 animals were used (35 for cortical measurements overlapping with 28 for NAc), with each animal providing 1-6 location data sets.

Surgery

Animals were anesthetized with urethane (1.5 g/kg i.p.) and placed in a stereotaxic frame (Kopf, Tujunga, CA, USA). Holes were drilled for recording electrodes in the NAc (+2.2 mm A-P, +1.7 mm M-L, -6.4 to -7.8 mm D-V) or somatosensory cortex (+0.6 mm A-P, +2.8 mm M-L; +2.0 mm A-P, +2.6 mm M-L, -0.9 to -2.0 mm D-V for each) (Hall and Lindholm, 1974, Hoffmeyer et al., 2007). Coordinates are referenced from bregma according to the atlas of Paxinos and Watson (2007). A Ag/AgCl wire placed in the contralateral hemisphere served as an iontophoresis ground and reference electrode.

Drugs and Solutions

NMDA, AMPA, 1,2,3,4-tetrahydro-7-nitro-2,3-dioxoquinoxaline-6-carbonitrile disodium salt (CNQX, AMPAR antagonist), DL-2-amino-5-phosphonopentanoic acid sodium salt (AP5, NMDAR antagonist), N^{ω}-propyl-L-arginine hydrochloride (L-ARG, neuronal nitric oxide synthase [nNOS] inhibitor), 3-[(2-methyl-1,3-thiazol-4-yl)ethynyl]pyridine hydrochloride (MTEP, mGluR5 antagonist), and dihydrokainic acid (DHK, GLT-1 glutamate transporter blocker) were purchased

from Abcam (Cambridge, MA, USA). NG-Nitro-L-arginine methyl ester hydrochloride (L-NAME, nitric oxide synthase [NOS] inhibitor) and (±)-1-aminocyclopenate-*trans*-1,3-dicarboxylic acid (ACPD, group I/II mGluR agonist) were acquired from Tocris Bioscience (Ellisville, MO, USA). All other chemicals were purchased from Sigma Aldrich (St. Louis, MO, USA).

All drugs were dissolved in 5 mM NaCl. All solutions except L-NAME, L-ARG, and MTEP incorporated 0.5 mM uric acid as an inert, electroactive tracer and were ejected with cathodic currents (-25 to -400 nA). Drugs ejected with anodic current (+30 to +150 nA; L-NAME, L-ARG, and MTEP) were adjusted to pH 6-7 using 0.1 M NaOH and used 4-methylcatechol as an inert tracer with concentrations matching that of the drug (Bucher et al., 2014).

Voltammetric O_2 Measurements and Iontophoresis

Mutimodal sensors were fabricated as described previously (Belle et al., 2013). A 5 µm diameter carbon fiber, pulled into a glass capillary, was inserted into a 4-barrel capillary and cut under a light microscope to an exposed length between 80 - 120 µm. The three remaining barrels were filled with drug solutions.

Fast-scan cyclic voltammetry (FSCV) measurements were controlled using High-Definition Cyclic Voltammetry (HDCV) software (Bucher et al., 2013). The cyclic voltammetry waveform scanned from a holding potential of 0.0 V to +0.8 V, then to -1.4 V, and finally back to the holding potential (all vs. Ag/AgCl reference electrode) over an 11 ms time span. The voltammetric scan rate was 400 V s^{-1}. Carbon-fiber surfaces were conditioned in the brain by cycling the waveform at 60 Hz, then 10 Hz, for 15 minutes each. Data were collected at 5 Hz during simultaneous electrochemical and electrophysiological measurements as described previously (Takmakov et al., 2011). Custom instrumentation controlled the connection of the carbon fiber alternately between a current transducer (for cyclic voltammetry) and a voltage follower (single-unit activity measurements) (Takmakov et al., 2011).

Iontophoretic ejections were performed by applying constant current (NeuroPhore BH-2 System, Harvard Apparatus, Holliston, MA, USA). A data acquisition program controlled ejection timing (HDCV, UNC Chapel Hill, Chapel Hill, NC). Iontophoresis barrels were primed at least 400 µm dorsal to the measurement region (-0.5 mm D-V cortex, -5 to -6 mm D-V NAc) to ensure reproducible ejections. Baseline experiments collected voltammetry data in absence of chemical or electrical stimulation.

Single-Unit Activity Electrophysiology

Single-unit activity was measured for 179 ms between each cyclic voltammetric scan. The data were amplified (x5,000), fed through a bandpass filter (300 – 3,000 Hz, Krohn-Hite Corp., Brockton, MA), and digitized using commercially available software (Digitizer, Plexon, Dallas, TX, USA).

Data Analysis

Cyclic voltammetry data were background subtracted and filtered using a 4^{th} order low pass Bessel filter with a 2 kHz cutoff frequency. Data are summarized in color plots that show current magnitude in false color, voltages from the waveform along the ordinate, and time along the abscissa. A calibration factor of -0.35 nA μM^{-1} for O_2 was obtained from a calibration curve as shown previously (Bucher et al., 2014). Concentration data were normalized to the glutamate response in absence of drug ("control") prior to statistical analysis. Principal component regression (PCR) was utilized to confirm that faradaic currents resulted only from O_2 or drug (Rodeberg et al., 2015). O_2 PCR training sets for every electrode were built from naturally occurring transients (Walton et al., 2016). Glutamate PCR training sets were built from ejections, and drug PCR training sets were built from drug only ejections during times when O_2 transients were not present as determined by background subtraction.

Single units were analyzed using Offline Sorter, which uses principle component analysis to sort different events (Plexon, Dallas, TX, USA). Firing rate statistics from perievent event histograms were exported from NeuroExplorer (NexTechologies, Madison, AL).

Probing Local Glutamatergic Mechanisms with a Multimodal Sensor

A multimodal sensor, described in previous work (Walton et al., 2016), was placed in either the cortex or the NAc. One barrel contained glutamate (200 mM) and one or both of the remaining two barrels contained drugs of interest. Each electrode was used for 1-6 locations if background currents remained stable, both to avoid damaging tissue and minimize the number of rats. Recording locations were acquired at least 300 µm apart (Belle et al., 2013).

We ejected glutamate (2 s) while lowering the multimodal sensor to locate cells. Only locations exhibiting reproducible single-unit activity time-locked to glutamate ejections were defined as cells. A full data set included 3-6 replicates each of the following: 1.) A 2 s glutamate ejection (control); 2.) A 120 s drug ejection; 3.) A 120 s drug ejection with co-ejection of glutamate from 60-62 s; and 4.) A recovery set of 2 s glutamate ejections taken 10 minutes after the last drug ejection file (Figure 5.1A). The order of 2 and 3 was randomized. Time between glutamate ejections was 120 s in control and recovery files. Time between drug files was 200-300 s to allow for drug clearance.

Glutamate Receptor Pharmacology in the Somatosensory Cortex

NMDARs were antagonized using AP5 (50 mM). AMPARs were antagonized with CNQX (10 mM). Whenever the third iontophoresis barrel was available, either agonist NMDA (100 µM) or AMPA (200 µM) were used to qualitatively confirm excitatory effects.

To raise endogenous extracellular glutamate and investigate the effect of tonic mGluR activation, we iontophoresed an iGluR antagonist cocktail of AP5 (35 mM) and CNQX (18 mM),

with a glutamate transporter GLT-1 blocker (DHK, 10 mM). In a parallel experiment, we agonized group I and II mGluRs with ACPD (6 mM). To examine the influence of downstream nitric oxide (NO) synthesis on glutamate-induced O_2 consumption, we inhibited NOS activity with L-NAME (5 mM).

Glutamate Receptor Pharmacology in the Nucleus Accumbens

We used similar pharmacological manipulations in the NAc as in the cortex. In addition, we investigated the neuronal contributions to NO production using L-ARG (5 mM) to inhibit nNOS over endothelial and inducible NOS (eNOS and iNOS, respectively). We then used MTEP (10 mM) to antagonize mGluR5, as it is most prevalent mGluR in the NAc (D'Ascenzo et al., 2007).

Histology

Following data collection, the last electrode location was marked by cyclically applying a ramp of 0 – 10 V DC potential manually three times over 20 s to generate a lesion. Animals were sacrificed with urethane cardiac puncture. Brains were removed and fixed in 10% formalin for >7 days. Brains were then cryoprotected in 30% sucrose for >48 hr, before coronal sections (50 µm) were taken with a freezing microtome (Leica, Germany). Slices were mounted on microscope slides and viewed under a light microscope to confirm lesion locations.

Statistical Analyses

Statistical analysis was performed using GraphPad Prism 6 (GraphPad Software, San Diego, CA, USA). The average single-unit activity during 2 s glutamate ejections served as the 100% cell firing control. The apex of O_2 consumption within 15 s of the glutamate ejection served as the 100% O_2 control. Significance between glutamate excitation before, during, and

after drug application was evaluated using a repeated measures one-way analysis of variance (ANOVA) with a Geisser-Greenhouse (G-G) correction and a post-hoc Dunnett's multiple comparisons test versus control (100%). Data are presented as the mean ± SEM and *n* values representing the number of unique recording locations. Any locations that lacked O_2 responses were excluded from O_2 analysis, though the single-unit activity data was included if present. A Student's t-test was used to evaluate significance between split cell populations. *P* values <0.05 were considered significant.

Results

Glutamate Iontophoresis Evokes Changes in Single-Unit Activity and O_2 Consumption

First, we chose to validate our previous approach for assessing concomitant single-unit activity and O_2 concentration changes using a multimodal sensor (Walton et al., 2016). We measured single-unit activity and O_2 concentration changes evoked by local glutamate ejection (example in Figure 5.1B-C). As before, we confirmed that glutamate ejections were not excitotoxic (Figure 5.2). Using the same ejection current, we recorded three sequential trials each of 5, 10, and 20 s glutamate ejections (200 mM) and spaced the ejections 120 s apart (Figure 5.2). These stimuli elicited single-unit firing, but did not injure or desensitize cells, even during the longest (20 s) ejection time (Figure 5.2C), consistent with previous studies that used near-saturated glutamate concentrations (Krnjević and Phillis, 1963). We used PCR training sets to separate O_2 currents from glutamate ejection currents (Figure 5.2, *top*). Though these traces appeared noisy due to natural, spontaneous O_2 transients (Walton et al., 2016), residual plots (Figure 5.2, *bottom*) confirmed that the current due to noise was below a training set specific predicted threshold value (Q_α) and thus validated the PCR analysis (Rodeberg et al., 2015). We found that, regardless of ejection duration, locations continued to respond with O_2 decreases (Figure 5.2). These observations were consistent with our previous report, and

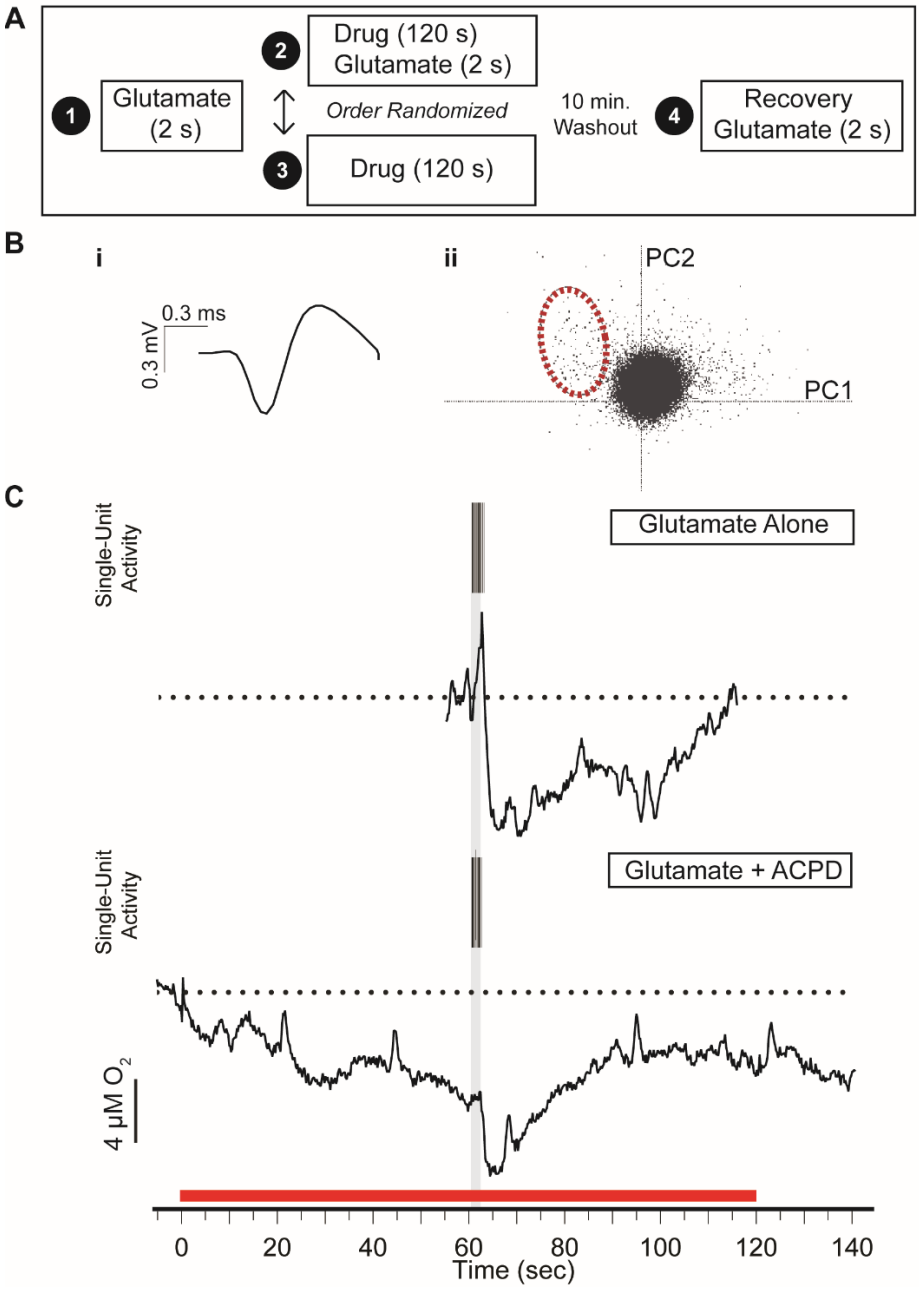

Figure 5.1. Experimental paradigm to assess the differences between single-unit activity and O_2 responses to glutamate excitation with and without pharmacological manipulation. (A) Protocol schematic. (B) (i) A single-unit waveform recorded in the NAc. (ii). PCR extracted neuronal activity from background noise, visualized in 2-D waveform density plots. The central black cluster represents noise waveforms, while the cluster outlined in red represents the single unit from (i) resolved from background. (C) Glutamate ejections evoked single-unit firing and O_2 decreases. *(Top)* The cell in A, exposed to a 2 s glutamate ejection. (*Bottom*) The same cell as above exposed to the drug and glutamate paradigm. The drug example shown is ACPD (mGluR agonist). Black tics indicate single-unit action potentials. Below them are PCR extracted O_2 traces from cyclic voltammetry currents. Dashed lines indicate baseline current. The grey box indicates glutamate ejection time, and the red box indicates drug ejection time.

confirmed that glutamate iontophoresis at our chosen barrel concentration would evoke reliable single-unit activity and O_2 changes without excitotoxic effects.

Single-Unit Activity and O_2 Consumption Couple and Scale with Glutamate Ejection Currents across Sensors

Previous work established that drug quantities ejected using the same ejection currents are inconsistent between iontophoresis barrels (Herr et al., 2008). To ensure that we could average data collected across many of our multimodal sensors, we next ejected glutamate using 5-300 nA currents at multiple (n=6) electrodes in both cortex and NAc locations. When we normalized single-unit activity and O_2 concentrations to the maximum ejection current, we found a linear relationship between ejection current and single-unit activity (R^2=0.71, Figure 5.3), and between ejection current and O_2 consumption (R^2=0.75, Figure 5.3) across multiple electrodes. Additionally, the O_2 consumed and single-unit responses correlated (Pearson's correlation, P<0.0001). Therefore, normalizing cell firing and O_2 data provided a meaningful way to compare data between these multimodal sensors.

Neuronal Activity and O_2 Remain Coupled in the Somatosensory Cortex During NMDAR, but Not AMPAR, Antagonism

We determined in a previous study that iGluRs influenced glutamate-induced O_2 consumption, which couples to single-unit activity (Walton et al., 2016). To investigate the individual contributions of iGluRs to coupled single-unit activity and O_2 concentration changes, we used our multimodal sensor to eject antagonists and compare pre-drug responses to glutamate excitation against responses during drug delivery (example in Figure 5.1C). We used AP5 to antagonize NMDARs and CNQX to antagonize AMPARs. Both AP5 and CNQX significantly reduced glutamate-elicited cell firing in the cortex, (AP5: F=4.4, P=0.053; 45.0 ±

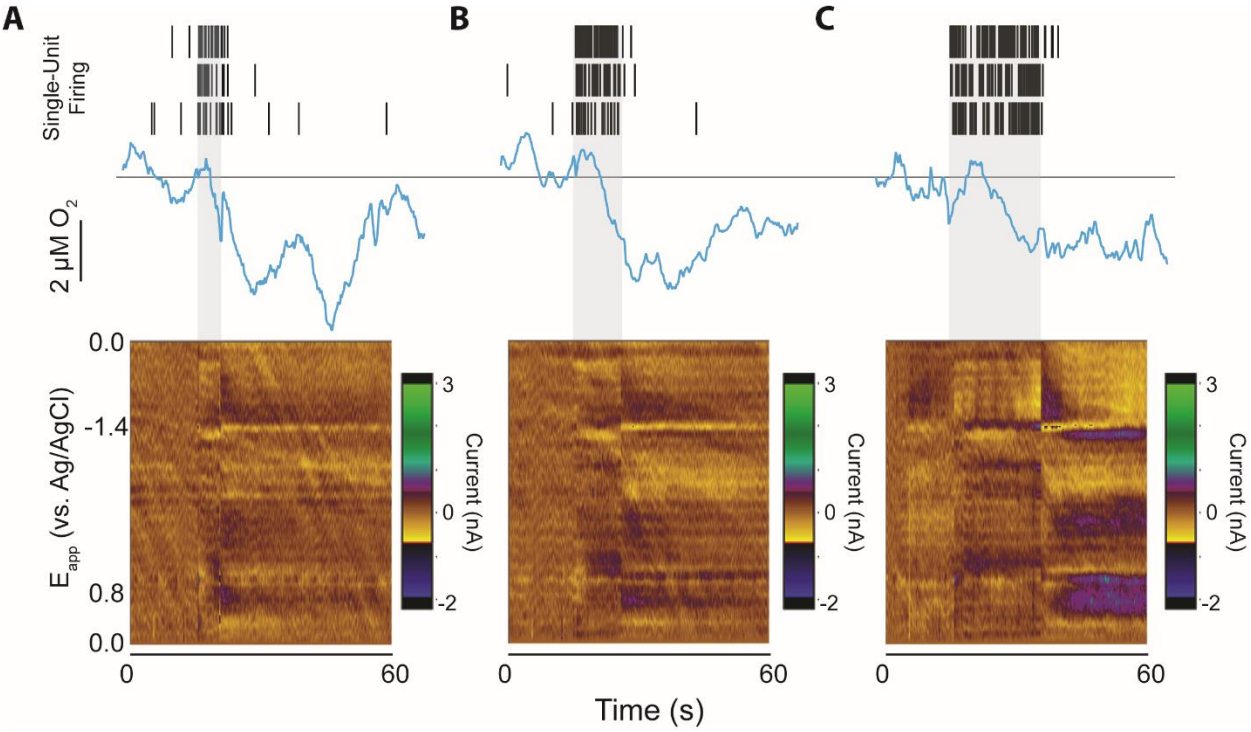

Figure 5.2. Extended glutamate iontophoresis (200 mM) was not excitotoxic. (*Top*) PCR extracted O_2 current traces for 5 s (A), 10 s (B), and 20 s (C) glutamate ejection times, each represented by grey boxes. Black tics represent single-unit action potentials. Dashed lines indicate baseline current. (*Bottom*) Corresponding PCR residual currents are below the anticipated noise threshold, and do not contain signals that indicate the presence of other analytes. The data shown are from a NAc location.

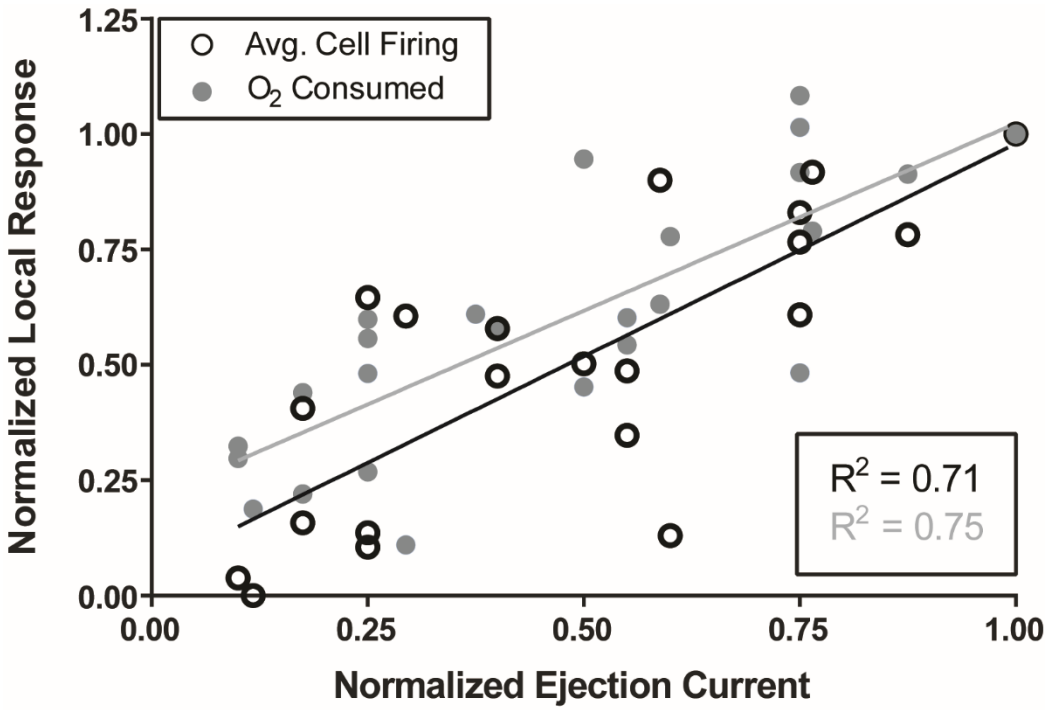

Figure 5.3. Single-unit activity and local O_2 consumption responded linearly with increasing ejection currents. All data are normalized to the values obtained at the highest ejection current used with each sensor. Each point represents an average of three repeated trials using the same current (n=6 locations). Error bars are omitted for clarity.

9.6%, *n*=10, Dunnett's post-hoc *P*<0.001; CNQX: *F*=20.1, *P*<0.0001; 53.0 ± 6.7%, *n*=9, Dunnett's post-hoc *P*<0.001; Figure 5.4A); however, cells exposed to CNQX did not recover to pre-drug firing rates (69.7 ± 7.4% of control, *n*=9, Dunnett's post-hoc *P*<0.01; Figure 5.5A).

Surprisingly, NMDAR and AMPAR antagonism exerted differential effects on glutamate-elicited O_2 consumption. NMDAR antagonism with AP5 significantly reduced both the magnitude of O_2 consumption in the cortex (*F*=14.6, *P*=0.0007; 48.5 ± 6.6%, n=10, Dunnett's post-hoc *P*<0.0001; Figure 5.4A), and the time to reach maximum O_2 consumption (9.8 ± 0.96 s before drug vs. 6.7 ± 0.77 s during drug; $t_{(2,20)}$=2.5, *P*=0.022; Figure 5.6). In contrast, O_2 consumption during AMPAR antagonism with CNQX did not decrease (Dunnett's post-hoc *P*>0.05, Figure 5.4A), despite reduced single-unit activity. These data indicated that glutamatergic excitation conserved neuronal activity and O_2 consumption coupling in the cortex and NAc with antagonized NMDARs, whereas glutamate unilaterally diminished neuronal firing without altering O_2 responses in the case of AMPAR antagonism.

Single-Unit Activity and O_2 Consumption in the Somatosensory Cortex Decrease During iGluR and GLT-1 Blockade, but Decouple with Exclusive mGluR Agonism

Because mGluRs are known to exert influence over vasculature through astrocytes (Zonta et al., 2003, Petzold et al., 2008, Carmignoto and Gómez-Gonzalo, 2010), we investigated whether agonizing these receptors would affect O_2 responses. First, we ejected a cocktail consisting of AP5, CNQX, and the glutamate transporter inhibitor DHK to raise endogenous glutamate concentrations while blocking iGluR activation. During ejection of this cocktail, glutamate-induced firing significantly decreased (*F*=20.9, *P*=0.002; 7.3 ± 4.0%, *n*=7, Dunnett's post-hoc *P*<0.0001; Figure 5.4B), as did O_2 consumption (*F*=17.2, *P*=0.019; 41.2 ± 4.3%, *n*=4, Dunnett's post-hoc *P*<0.01; Figure 5.4B). We applied the group I/II mGluR agonist, ACPD, to isolate mGluR agonism without the confounding factor of the iGluR blockade. The result was a significant decrease in firing (*F*=3.1, *P*=0.12; 43.7 ± 10.0% of control, *n*=8,

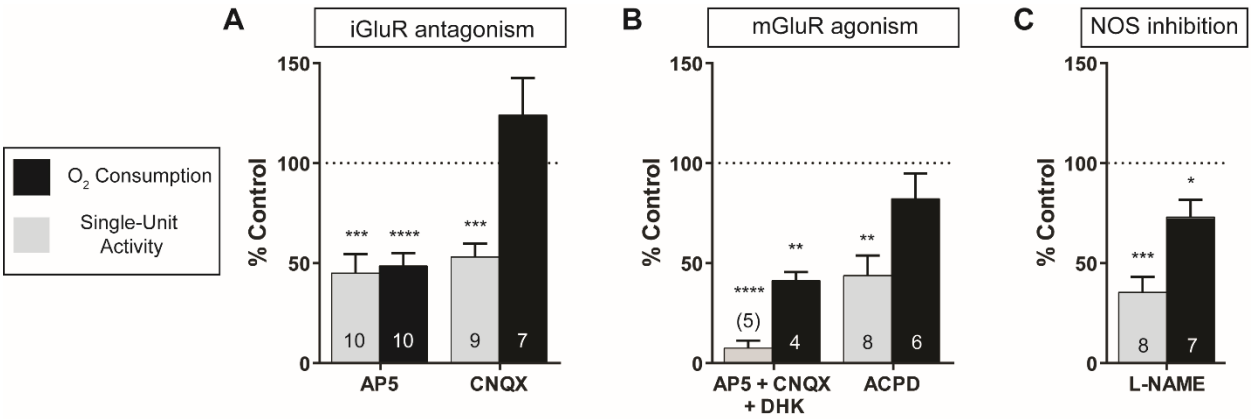

Figure 5.4. Single-unit activity and O_2 coupling in the cortex was conserved through pharmacological manipulations. (A) iGluR antagonism. (B) Direct and indirect mGluR agonism. (C) NOS inhibition. Values are percentages of the corresponding control values, defined as the single-unit activity firing and O_2 consumption following a 2 s ejection of glutamate (200 mM). Values in each bar indicate the number of locations. Error bars indicate SEM. Dotted line represents 100% control values. Drug targets are as follows: AP5, NMDAR antagonist; CNQX, AMPAR antagonist; DHK, GLT-1 transporter blocker; ACPD, group I/II mGluR agonist; L-NAME, NOS inhibitor. Significance was established using a one-way, repeated measures ANOVA. Dunnett's post-hoc significance versus control: *P<0.05, **P<0.01, ***P<0.001, ****P<0.0001

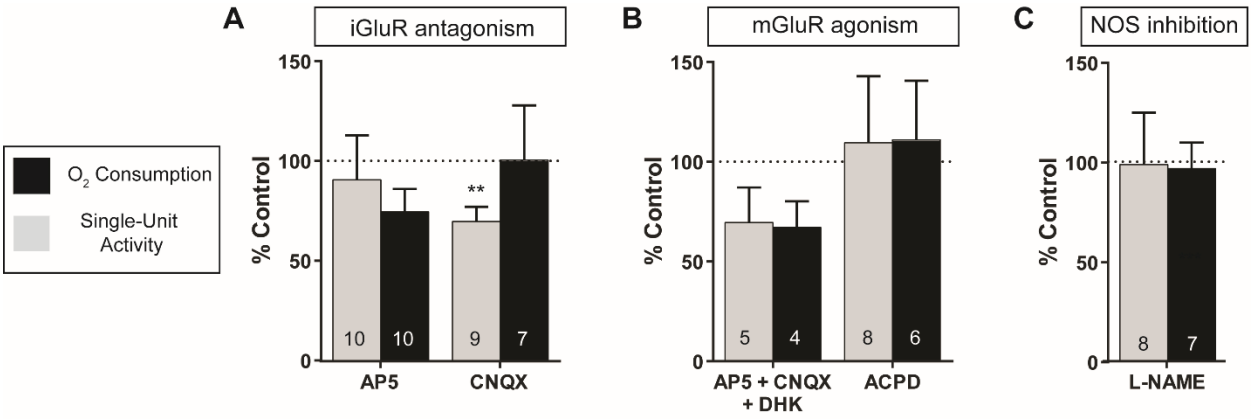

Figure 5.5. With the single exception of single-unit activity under AMPAR antagonism, all cortical cells recovered to control (i.e., pre-drug glutamate) levels following a drug washout period. (A) iGluR antagonism. (B) Direct and indirect mGluR agonism. (C) NOS inhibition. Values are percentages of the corresponding control values, defined as the single-unit activity firing and O_2 consumption following a 2 s ejection of glutamate (200 mM). Error bars indicate ± SEM. Dotted line represents 100% control values. Drug targets are as follows: AP5, NMDAR antagonist; CNQX, AMPAR antagonist; DHK, GLT-1 transporter blocker; ACPD, group I/II mGluR agonist; L-NAME, NOS inhibitor. Significance was established using a one-way, repeated measures ANOVA. Dunnett's post-hoc significance versus control: ***P*<0.01

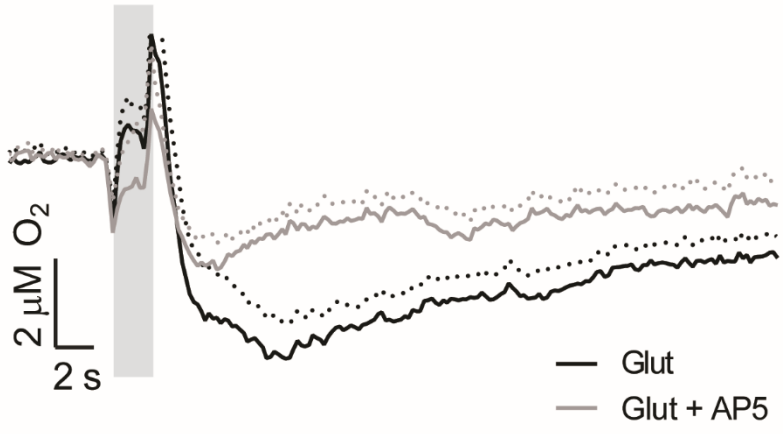

Figure 5.6. NMDAR antagonism using AP5 significantly reduced the amplitude of O_2 consumption and the time to maximum O_2 consumption via glutamate stimulation ($t_{(2,20)}$=2.5, P=0.022). Solid lines indicate current traces from cyclic voltammetry data taken from the O_2 reduction potential. Dotted lines represent SEM. Grey box indicates time of glutamate iontophoresis.

Dunnett's post-hoc $P<0.01$; Figure 5.4B) without significant changes to O_2 consumption (Dunnett's post-hoc $P>0.05$, Figure 5.4B). Together, these data indicated that blocking glutamatergic influence through iGluRs produced coupled decreases in evoked single-unit firing and O_2 consumption, but that extended periods of mGluR activation attenuated cell firing without affecting O_2 changes.

NOS Inhibition in the Somatosensory Cortex Diminishes Single-Unit Activity and O_2 Responses

Activation of NMDARs results in the downstream synthesis of the vasodilative neurotransmitter NO (Faraci and Brian, 1994). To test if the synthesis of this vasoactive molecule affected O_2 consumption, we locally inhibited nitric oxide synthase (NOS) using L-NAME. Surprisingly, NOS inhibition significantly attenuated cell firing (F=4.7, P=0.063; 35 ± 7.7%, n=8, Dunnett's post-hoc $P<0.001$; Figure 5.4C) and decreased the magnitude of O_2 consumption (F=3.8, P=0.065; 73.1 ± 8.8%, n=7, Dunnett's post-hoc $P<0.05$; Figure 5.4C). This indicated that NOS inhibition reduces the amount of O_2 consumed following glutamatergic excitation, however this effect might be attributed to NOS suppression of local single-unit firing.

iGluR Antagonism Exerts Similar Control over Single-Unit Activity in Both the Cortex and NAc

The NAc is a subcortical region with basal glutamate concentrations similar to the somatosensory cortex (Baker et al., 2003, Homola et al., 2006), although it differs in its neuronal architecture. This similarity prompted us to study whether glutamate exerted the same neurovascular influence in the NAc as compared to the cortex. First, we antagonized iGluRs to see whether local NAc environments would respond the same way as in the cortex. Both antagonizing NMDARs with AP5 and AMPARs with CNQX significantly attenuated single-unit firing (AP5: F=9.7, P=0.006; 38.7 ± 9.5%, n=8, Dunnett's post-hoc $P<0.001$; CNQX: F=5.9, P=0.019; 56.2 ± 11.4%, n=9, Dunnett's post-hoc $P<0.01$; Figure 5.7A). Glutamate stimulations

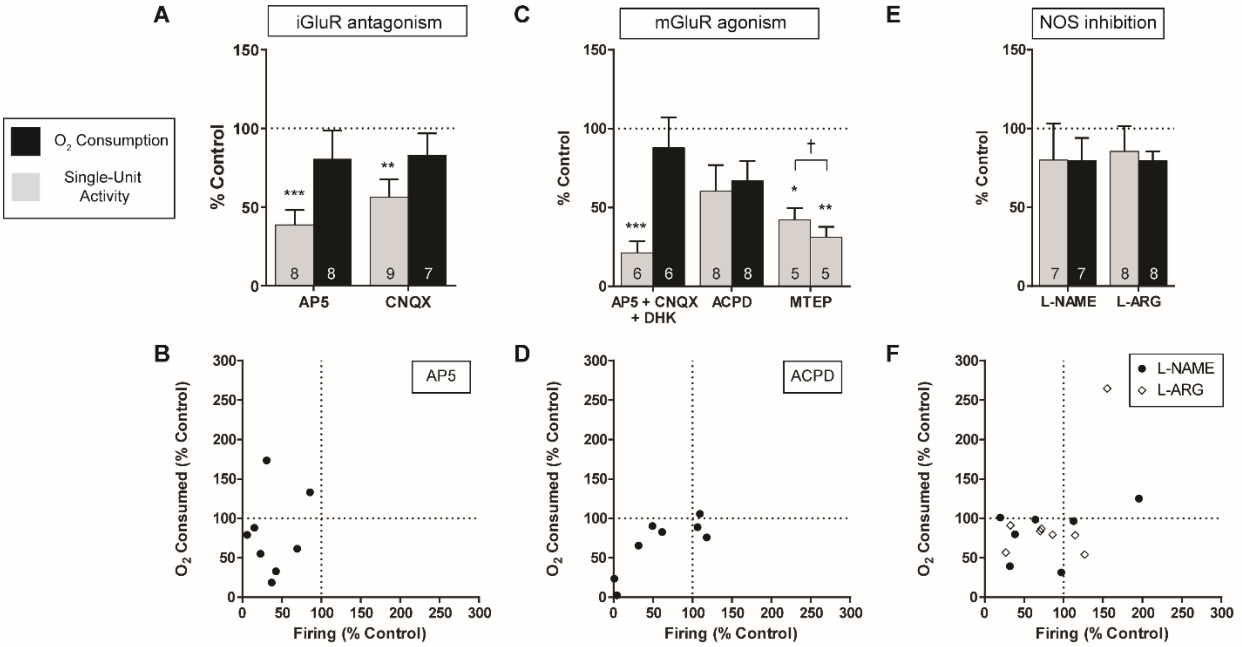

Figure 5.7. Single-unit activity and O_2 coupling in the NAc was not always conserved during pharmacological manipulations of iGluRs, mGluRs, and NOS. (A) Overall results of iGluR antagonism. (B) Correlation plot relating single-unit activity and O_2 consumption for AP5 results. (C) Overall direct and indirect mGluR agonism responses. (D) Correlation plot relating single-unit activity and O_2 consumption for ACPD results. (E) Overall NOS inhibition responses. (F) Correlation plot relating single-unit activity and O_2 consumption responses to specific nNOS inhibition (L-ARG) and non-specific NOS inhibition (L-NAME). Values are percentages of the corresponding control values, defined as the single-unit activity firing and O_2 consumption following a 2 s ejection of glutamate (200 mM). Error bars indicate SEM. Dotted lines represent 100% control values. Drug targets are as follows: AP5, NMDAR antagonist; CNQX, AMPAR antagonist; DHK, GLT-1 transporter blocker; ACPD, group I/II mGluR agonist; MTEP, mGluR5 antagonist; L-NAME, NOS inhibitor, L-ARG, nNOS inhibitor. Significance between control and drug effects was established using a one-way, repeated measures ANOVA and Dunnett's post-hoc versus control: $*P < 0.05$, $**P < 0.01$, and $***P < 0.001$. Significant differences between multiple responses to a drug were established using an unpaired, 2-tailed t-test: $^{\dagger}P < 0.05$.

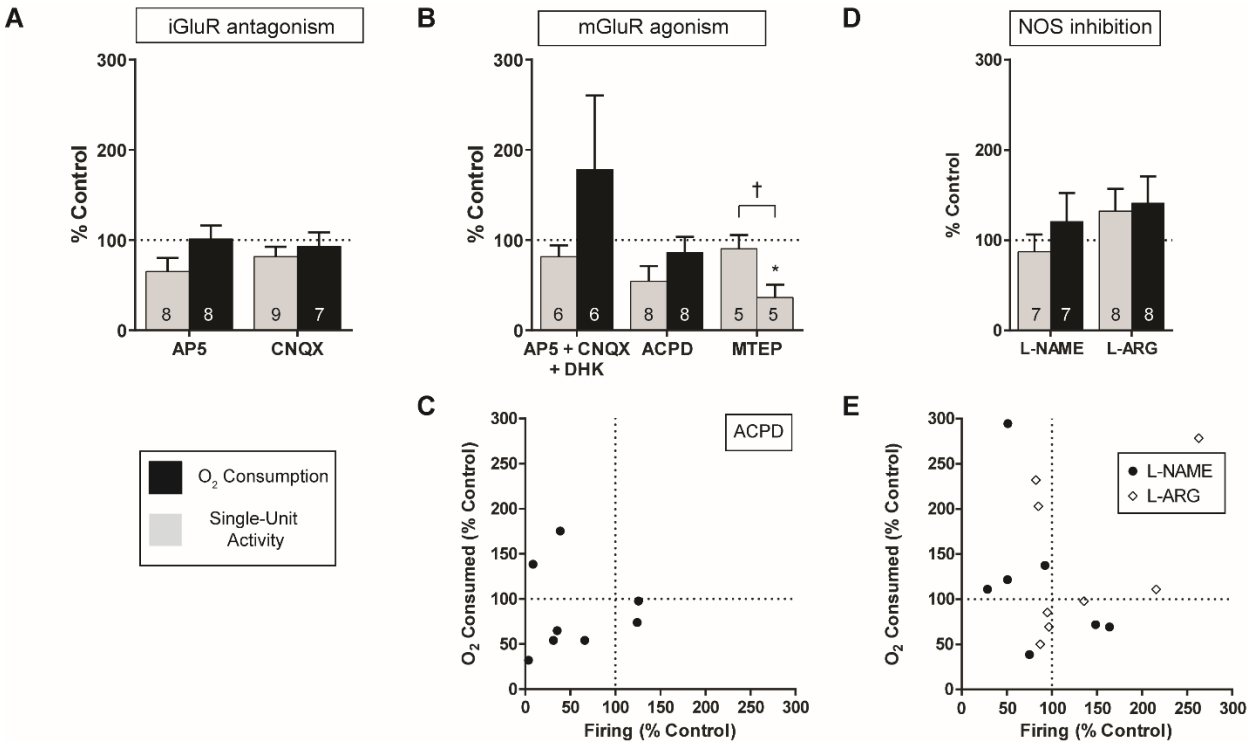

Figure 5.8. Cells in the NAc recovered from iGluR antagonists and nNOS inhibition, but other drugs continued to diminish single-unit activity after a drug washout period. (A) Overall results of iGluR antagonism recovery. (B) Overall direct and indirect mGluR agonism recovery responses. (C) Correlation plot relating single-unit activity and O_2 consumption for partial ACPD recovery. (D) Overall NOS inhibition responses. (E) Correlation plot relating single-unit activity and O_2 consumption recovery responses from specific nNOS inhibition (L-ARG) and non-specific NOS inhibition (L-NAME). Values are percentages of the corresponding control values, defined as the single-unit activity firing and O_2 consumption following a 2 s ejection of glutamate (200 mM). Error bars indicate SEM. Dotted line represents 100% control values. Drug targets are as follows: AP5, NMDAR antagonist; CNQX, AMPAR antagonist; DHK, GLT-1 transporter blocker; ACPD, group I/II mGluR agonist; MTEP, mGluR5 antagonist; L-NAME, NOS inhibitor, L-ARG, nNOS inhibitor. Significance was established using a one-way, repeated measures ANOVA. Dunnett's post-hoc significance versus control: $^{*}P<0.05$. Significant differences between multiple responses to a drug were established using an unpaired, 2-tailed t-test: $^{\dagger}P<0.05$.

under both NMDAR and AMPAR antagonism showed no O_2 changes relative to control (Dunnett's post-hoc *P*>0.05, Figure 5.7A). However, NMDAR antagonism with AP5 reduced both cell firing and O_2 consumption in the majority of locations with two distinct O_2 consumption outliers, which may indicate either partial decoupling as a result of this drug, or two discrete neuron populations that respond differently (Figure 5.7B). There was no significant correlation between single-unit activity and O_2 consumption (Pearson's *P*>0.05, Figure 5.7B). Each location fully recovered from both drugs (Figure 5.8A). With few exceptions, glutamate acting through iGluRs exhibited similar control over single-unit firing and O_2 consumption changes in the NAc as in the somatosensory cortex.

Neuronal Activity and O_2 Consumption in the NAc Decouple During iGluR and GLT-1 Blockade, but Partially Decouple During mGluR Agonism

Due to the similarities in iGluR regulation of single-unit firing and O_2 consumption between the cortex and NAc, we next asked if mGluR agonism was similar between the two brain regions. First, a cocktail of AP5, CNQX, and DHK blocked extracellular glutamate uptake and antagonized iGluRs, resulting in significant attenuation of single-unit activity (*F*=23.1, *P*=0.0014; 21.3 ± 7.3%, *n*=6, Dunnett's post-hoc *P*<0.001; Figure 5.7C). Surprisingly, this did not affect O_2 consumption (Dunnett's post-hoc *P*>0.05, Figure 5.7C). We then ejected ACPD to agonize mGluR groups I/II without the iGluR blockade. The results differed from both the cocktail in the NAc and the effects of ACPD in the cortex, with a slight decrease in cell firing (*F*=5.7, *P*=0.03; 60.2 ± 16.6%, *n*=8, Dunnett's post-hoc *P*=0.08; Figure 5.7C) and no decrease in O_2 consumption (*F*=1.8, *P*=2.1; 66.9 ± 12.6%, *n*=8, Dunnett's post-hoc *P*>0.05; Figure 5.7C). Interestingly, mGluR group I/II agonism with ACPD also produced disparate responses in NAc locations: five locations showed decreased cell firing and three locations remained unaffected in terms of cell firing, with a difference in variance between subjects in addition to drug treatment (*F*=3.2, *P*=0.03; Figure 5.7D). It is worth noting that both responses were found in the same

subject with the same probe in two different subjects, and thus experimental error is not likely a source of these dissimilarities. Further, these data showed a significant correlation (Pearson's $R^2 = 0.64$, P=0.02; Figure 5.7D), indicating that ACPD either partially decouples single-unit firing and O_2, or that the drug effects differed depending on the location within the NAc. Finally, the locations treated with ACPD that did show slight decreases in cell firing and O_2 consumption did not recover to pre-drug metrics and no longer correlated after the recovery epoch (Pearson's P>0.05; Figure 5.8C). These responses indicated that mGluR agonism affected O_2 consumption differently between the NAc and the cortex in the presence of an iGluR blockade. Additionally, the responses in the NAc showed partial decoupling of cell firing and O_2 consumption in response to mGluR agonism that corresponded with whether or not these metrics recovered after drug washout.

mGluR5 Antagonism Affects Neuronal Firing in the NAc in Two Different Ways

The majority of NAc mGluRs are located pre-synaptically (mGluR3), post-synaptically (mGluR1), or both perisynaptically and on astrocytes (mGluR5) (D'Ascenzo et al., 2007, Mitrano et al., 2010). To investigate the split results of extended mGluR activation with ACPD, we used an mGluR5-specific antagonist, MTEP, to see whether modulating the activities of this specific mGluR also produced a split population of cell responses. Though all cells collectively responded with decreased single-unit activity under mGluR5 antagonism, we made the interesting observation that MTEP increased basal firing rates at some locations (Figure 5.9). We separated locations where cells responded to the drug itself from those that did not change baseline firing, and found a significant split between the cell firing values ($t_{(2,8)}$=2.6,P=0.029; Figure 5.7C). These populations further differed in their ability to recover sensitivity to glutamate after drug washout. Cells excited by MTEP showed significantly diminished single-unit activity responses to glutamate ejections during MTEP (F=16.8, P=0.0051; 42.0 ± 7.6% n=5, Dunnett's

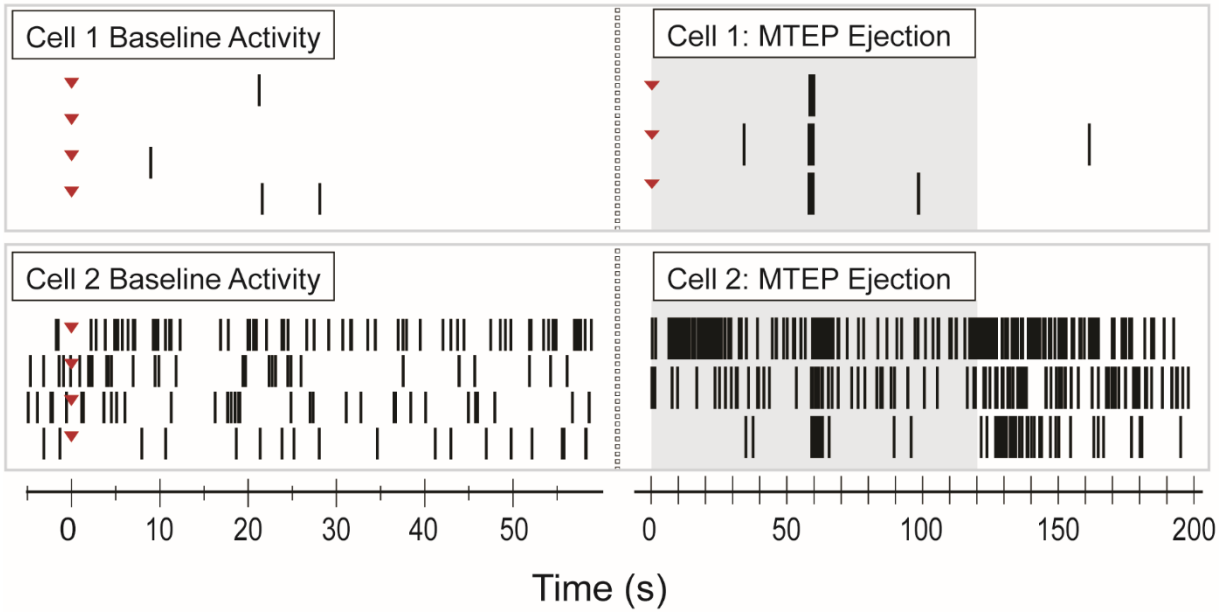

Figure 5.9. MTEP (mGluR5 antagonist) ejections in the NAc affected single-unit activity in one of two ways. Shown is a raster plot where tic marks indicate action potentials. (*Left*) Baseline firing activity in absence of drug or glutamate. (*Right*) Firing activity during MTEP ejection (0-120 s) and glutamate (60-62 s). Cell 1 represents the cell type that did not increase baseline firing with MTEP. Cell 2 is an example of a cell that increased baseline firing during MTEP ejection. Grey box indicates the duration of MTEP ejection. Blue triangles indicate time=0 s, and are included to clarify the multiple single-unit files taken for baseline.

post-hoc P<0.01; Figure 5.7C) that lasted through the recovery period (36.2 ± 14.2%, n=5, Dunnett's post-hoc P<0.05; Figure 5.8B). In contrast, single-unit firing in the other population significantly decreased (69.0 ± 6.8%, n=5, Dunnett's post-hoc P<0.05; Figure 5.7C), but recovered (Dunnett's post-hoc P>0.05, Figure 5.8B). The two populations also split based on their response to glutamate recovery ejections ($t_{(2,8)}$=2.6, P=0.032; Figure 5.8B). PCR could not isolate reliable O_2 signals during the ejection of this drug, so the effect on O_2 consumption was not addressed. Together, these data indicated mGluR modulation does not uniformly alter neuronal sensitivity to glutamate throughout the NAc; what differentiates these cell responses requires further investigation.

Dissimilarities between NOS Control over Neuronal Activity and O_2 Consumption in the NAc and Cortex Partially Depend on nNOS Specific Pathways

Since NOS inhibition produced a coupled decrease in single-unit firing and O_2 consumption in the cortex, we next ascertained the influence of NO synthesis on coupled responses in the NAc. We inhibited NOS using L-NAME and, as observed previously, the rate of single-unit firing did not change from pre-drug to drug treatment (Dunnett's post-hoc P>0.05; Figure 5.7E), though significant variance differences existed between subjects (F=3.4, n=7, P=0.03; Figure 5.7E). This reflected as an apparent split between NAc locations either diminishing or sustaining cell firing responses as a result of L-NAME NOS inhibition, but without a correlation (Pearson's P>0.05; Figure 5.7F). Both a diminished and sustained response occurred in one subject at two different locations, suggesting that the differences were not due to experimental error. Overall, no O_2 consumption changes occurred, though two locations showed decreases below 50% of pre-drug values (Dunnett's post-hoc P>0.05, Figure 5.7E-F). Following L-NAME washout, four of the seven locations failed to recover to pre-drug neuronal activity, corresponding to those locations with diminished firing during drug, again without any correlation between firing and O_2 consumption (Pearson's P>0.05; Figure 5.8E). This indicated

that NOS inhibition in the NAc affects neuronal sensitivity to glutamate, but not uniformly across all locations.

The microvascular environment could account for the different responses to L-NAME, a non-specific NOS inhibitor, which could act differently depending on the relative availabilities of eNOS and nNOS. Thus, we used L-ARG to selectively inhibit nNOS and remove the contribution of NO synthesized from NMDAR activation. As with L-NAME NOS inhibition, L-ARG NOS inhibition showed no significant changes to cell firing overall (Dunnett's post-hoc $P>0.05$, $n=8$; Figure 5.7E), though several locations showed modest decreases without any O_2 consumption correlation (Pearson's $P>0.05$; Figure 5.7F). As observed with L-NAME, two locations showed modest decreases in O_2 consumption with no significant decreases overall (Dunnett's post-hoc $P>0.05$; Figure 5.7E). However, contrary to the L-NAME responses, all locations fully recovered to baseline firing after L-ARG cleared (Dunnett's post-hoc $P>0.05$; Figure 5.8D-E). The continued split between neuronal sensitivity to glutamate during L-NAME and L-ARG indicated that NOS inhibition has varied effects at different locations within the NAc. Additionally, the ability of neurons to recover to pre-drug levels of glutamatergic excitation is related to the specific inhibition of nNOS.

Discussion

In this study, we compared how local glutamate receptor antagonism and NOS inhibition affect neurovascular coupling between the cortex and the NAc. We used iontophoresis to limit glutamatergic excitation and drug effects to highly localized environments. In both the cortex and NAc, we found that iGluRs subtypes exerted different control over neurovascular coupling. Single-unit activity and O_2 remained coupled during NMDAR, but not AMPAR antagonism. However, mGluR manipulations and NOS inhibition affected local coupling differently between the cortex and NAc. Additionally, mGluR and NOS pharmacological manipulations identified

multiple cell populations within the NAc with dissimilar responses to a given drug. Taken together, we concluded that glutamatergic mechanisms affect coupling between single-unit activity and O_2 consumption at a local level in ways that differ across different brain regions.

Here, we ejected both glutamate and pharmacological agents with iontophoresis to stimulate discrete environments and study local receptor modulation of neurovascular coupling. Importantly, glutamate iontophoresis is a selective stimulation that excludes the contributions of vasoactive agents released from either electrical or peripheral stimuli. Further, local drug ejections are advantageous over systemic drug administration in that they circumvent off target effects (e.g., changes in blood pressure), allow the use of drugs that cannot pass through the blood brain barrier (Herr et al., 2008, Belle et al., 2013, Kirkpatrick and Wightman, 2016), and exhibit different effects depending on whether they were administered locally or systemically (Bucher et al., 2014). Additionally, microenvironments in the brain are dissimilar. This technique can probe the heterogeneity both within and between diverse brain regions by providing a highly localized, chemically selective method of activating local neuronal environments with glutamate.

Glutamate exerts the majority of its synaptic transmission influence through iGluRs (Traynelis et al., 2010). We confirmed that iGluR antagonism led to cell firing decreases in the cortex and NAc; however, glutamate evoked O_2 consumption did not diminish with AMPAR blockade in either location. Attenuated neuronal activity during AMPAR blockade with CNQX agrees with electrical stimulation studies (Mathiesen et al., 1998, Nielsen and Lauritzen, 2001, Offenhauser et al., 2005, Hoffmeyer et al., 2007). These studies showed that CNQX inhibited CBF (Mathiesen et al., 1998, Nielsen and Lauritzen, 2001, Offenhauser et al., 2005, Hoffmeyer et al., 2007) and O_2 consumption (Offenhauser et al., 2005). CBF increases O_2 by delivering oxygenated blood, thus opposing O_2 consumption. Therefore, if neuronal activity is attenuated, O_2 consumption can appear disproportionately great for the decreased energetic demand when CBF is also impeded. This interpretation agrees with the O_2 data obtained with CNQX in both brain regions and the reported studies; however, our data did not agree with the study that

observed decreased O_2 consumption. This may reflect differences in glutamatergic versus electrical stimulations. Further, NMDAR antagonist effects diverged between studies. NMDAR antagonist MK-801 decreased CBF and neuronal activity (local field potentials) in one study (Nielsen and Lauritzen, 2001), but only attenuated CBF in another (Hoffmeyer et al., 2007). Neither MK-801 nor 2-amino-5-phosphoheptanoic acid (APH) affected CBF in third study (Mathiesen et al., 1998). Our data show that NMDAR antagonism decreases neuronal activity in both brain regions, but that the interplay of CBF and O_2 differed. Without simultaneously measuring CBF, we cannot discern whether O_2 consumption attenuated from decreased energetic demands or decreased energy demands coincident with unimpeded CBF, as both are reported possibilities.

A number of studies report vascular responses without postsynaptic iGluR activation that result from enhanced astrocytic mGluR activity (Chaigneau et al., 2007, Petzold et al., 2008, Scott and Murphy, 2012). Multiple mGluR subtypes are located perisynaptically and activated only during intense activity from synaptic glutamate spillover (Cartmell and Schoepp, 2000). To investigate mGluR agonism under these conditions, we antagonized iGluRs to exclude their contribution to coupling and blocked the primary astrocytic glutamate transporter, GLT-1, to increase extracellular glutamate concentrations. Single-unit activity diminished further than from NMDAR or AMPAR antagonism alone, in agreement with other studies (Pettit et al., 1997, Frick et al., 2001, Nielsen and Lauritzen, 2001, Hoffmeyer et al., 2007). The difference in O_2 usage following local glutamate stimulations between the NAc and cortex during drug delivery (i.e., decoupling from single-unit activity and remaining coupled, respectively) may indicate a difference in how the NAc neuronal architecture responds to increased extracellular glutamate. Indeed, the greater average density of astrocytes in the neostriatum as compared to the cortex would provide additional GLT-1 transporters to clear excess glutamate (Savchenko et al., 2000).

Neurovascular effects from downstream mGluR activation usually are studied using specific ligand agonism. Group I/II mGluR agonist ACPD causes vasodilation (Fergus and Lee,

1997, Zonta et al., 2003, Stobart et al., 2013), which may be responsible for the steady O_2 decrease that accompanied ACPD ejections (example shown in Figure 5.1C). It is worth noting that the evoked O_2 consumption in the NAc attenuated only slightly with ACPD relative to control despite the steady vasodilative O_2 decline (Dunnett's post-hoc: P=0.059, Figure 5.7B), but these data were pooled between cell populations exhibiting different levels of firing attenuation and, by extension, energetic demands (Figure 5.7D). Additionally, mGluR activation can lead to a host of responses through astrocytes that lead to either vasoconstriction or vasodilation depending on the predominating downstream process (Attwell et al., 2010). Ultimately, our results indicated that in the cortex, and a subset of NAc cells, mGluR agonism led to decoupled responses between single-unit activity and local O_2 consumption.

Several physical differences between the cortex and NAc can account for the dissimilar responses to mGluR agonism. ACPD has agonistic effects at all three mGluR groups (Cartmell and Schoepp, 2000), though most strongly at groups I and II, and therefore differential effects could result from the relative quantities of these mGluR types in the discrete recording areas. This is especially important to consider with high resolution techniques, as mGluR subtypes express in different relative ratios throughout the brain and across subcellular structures (e.g., axon, terminals) (Testa et al., 1994, Petralia et al., 1996, Mitrano and Smith, 2007). Of particular interest is mGluR2, which has been shown to depress synaptic transmission via presynaptic inhibition in both cortex and NAc (Burke and Hablitz, 1994, Xi et al., 2002). This is consistent with our results in the cortex, where this mGluR is more prevalent (Testa et al., 1994). Thus, the high spatial resolution of our multimodal sensor is likely detecting physically heterogeneous environments where neurovascular coupling is modulated differentially through mGluRs.

An important difference between the somatosensory cortex and the NAc is the existence of dopaminergic terminals in the latter brain region. The influence of mGluRs extends to mediating dopaminergic function in the NAc (Verma and Moghaddam, 1998, Bruton et al., 1999). Specifically, mGluR agonism raises basal striatal dopamine levels, which can augment or

diminish neuronal excitability (Surmeier et al., 2007, Cachope and Cheer, 2014). We observed extended (>30 s) catechol-like signals concomitant with ACPD ejections in some NAc locations but no cortical locations (data not shown). We were unable to definitively identify whether the signal was dopamine through our protocol. Though our multimodal sensor is capable of probing the relationship between mGluRs, dopamine, and O_2, it was outside the scope of this work.

We also considered whether the different cell responses with ACPD were from use of different ejection currents and thus inconsistent absolute concentrations of drug delivery. Studies have reported concentration-dependent effects from ACPD use (Lovinger, 1991, Taber and Fibiger, 1995, Verma and Moghaddam, 1998), but these effects compared µM – mM concentration ranges, which far exceeds concentrations delivered through iontophoresis (Kirkpatrick et al., 2014). Therefore, we do not believe that ejecting ACPD at different currents is responsible for the dissimilar responses observed in neuronal activity and O_2 consumption.

To address the disparate NAc responses with mGluR agonism, we investigated the most highly expressed mGluR in this region, mGluR5 (Testa et al., 1994, Romano et al., 1995). Antagonized mGluR5 attenuated neuronal firing, which supports the suppression of glial mGluR5-mediated NMDAR activation (D'Ascenzo et al., 2007). Cell firing attenuated regardless of whether or not MTEP elicited an increase in spontaneous basal firing rates (Figure 5.9). In both mGluR agonist and mGluR5 antagonist cohorts, we observed recording locations that did not recover from attenuated single-unit activity, contrasting with studies indicating that mGluR5 activation is required for long-term depression (Huber et al., 2001, Brebner et al., 2005); however, these studies evoked activity through electrical afferent stimulations as opposed to our localized approach. A more thorough investigation of local mGluR pharmacology in the NAc would elucidate whether the observed differences are due to heterogeneous recording environments or drug specificity.

We did not expect NOS to affect neuronal firing, as electrical stimulation studies showed that NOS inhibition does not alter synaptic activity (Offenhauser et al., 2005, Hoffmeyer et al.,

2007). This agreed with data in the NAc during both nonspecific NOS and specific nNOS inhibition, but not in all locations (Figure 5.7F). However, a study using L-NAME iontophoresis observed both excitatory and inhibitory effects on cell firing within the subthalamic nucleus (Sardo et al., 2006), which may indicate that observed single-unit activity suppression in both the cortex and NAc may result from local environmental factors. Interestingly, neuronal activity suppression persisted through a recovery epoch with nonspecific NOS inhibition and recovered with nNOS inhibition, indicating that eNOS may assist recovery from NO-based neuronal inhibition in the NAc. Taken together, these results indicate that local NOS inhibition likely affects neuronal sensitivity to glutamate differently depending on the surrounding environment.

In our previous work, L-NAME iontophoresis exclusively diminished events of local O_2 increases attributed to blood flow (Bucher et al., 2014). In the NAc, where NOS inhibition did not significantly alter neuronal firing or O_2 consumption, these data agreed. In the cortex, however, O_2 consumption decreased. This may result from either the attenuated cell firing in combination with attenuated CBF, as observed with CNQX, or because of the known modulatory role of NO in the somatosensory cortex (Lindauer et al., 1999). Briefly, increases in NO promotes quantified increases in vasodilation when NO acts as a modulator rather than requiring a threshold NO concentration to elicit vasoactivity. Therefore, inhibiting NO synthesis in the cortex leads to diminished O_2 consumption as blood vessels become constricted.

The capability to selectively excite and pharmacologically manipulate local neuronal populations enables the study of neurovascular coupling without off-target effects. However, it is important to recognize the weaknesses of this methodology. Local glutamate stimulation is less powerful than electrical stimulation, thus evoked O_2 changes are modest and can be obscured by natural O_2 transients (Figure 5.2, *top*)(Walton et al., 2016). Combined with the high spatial resolution and natural heterogeneity of neurovascular environments, these measurements can suffer in statistical power. G-G corrections in our ANOVA analysis indicated populations that reached significance in post-hoc testing without achieving significant variance between

treatments (e.g., cortical NOS inhibition effects). Therefore, our sensors require more recording locations to achieve statistical confidence.

The pharmacological agents introduce further complexities. Not all drugs dissolve in inert solvents at appropriate concentrations or eject with low ionic strength (Herr et al., 2008, Kirkpatrick and Wightman, 2016). Unique to our coupling of iontophoresis to FSCV, some drug ejection profiles obscure color plot data beyond that which PCR can extract (MTEP, *vide supra*). An alternative is to using higher solubility drugs, which may be inferior with respect to potency or specificity.

Despite these disadvantages, we used iontophoresis to study differences in glutamate evoked neurovascular coupling by exciting local neuronal populations and locally administering pharmacological agents. Glutamate exerts similar effects through iGluRs between the cortex and NAc, but we identified disparate mechanisms of action between these two areas with respect to manipulating mGluRs and NOS. These data provide evidence that compromising the functionality of glutamate receptors can disrupt the coupling between neuronal activity and O_2. Further, they illustrate location dependent heterogeneity in these responses that techniques like fMRI might overlook during interpretations of neurovascular coupling.

REFERENCES

Ances BM, Leontiev O, Perthen JE, Liang C, Lansing AE, Buxton RB (2008) Regional differences in the coupling of cerebral blood flow and oxygen metabolism changes in response to activation: implications for BOLD-fMRI. *NeuroImage* **39**:1510-1521.

Attwell D, Buchan AM, Charpak S, Lauritzen M, MacVicar BA, Newman EA (2010) Glial and neuronal control of brain blood flow. *Nature* **468**:232-243.

Baker DA, McFarland K, Lake RW, Shen H, Tang X-C, Toda S, Kalivas PW (2003) Neuroadaptations in cystine-glutamate exchange underlie cocaine relapse. *Nat Neurosci* **6**:743-749.

Belle AM, Owesson-White C, Herr NR, Carelli RM, Wightman RM (2013) Controlled iontophoresis coupled with fast-scan cyclic voltammetry/electrophysiology in awake, freely moving animals. *ACS Chem Neurosci* **4**:761-771.

Brebner K, Wong TP, Liu L, Liu Y, Campsall P, Gray S, Phelps L, Phillips AG, Wang YT (2005) Nucleus accumbens long-term depression and the expression of behavioral sensitization. *Science* **310**:1340-1343.

Bruton RK, Ge J, Barnes NM (1999) Group I mGlu receptor modulation of dopamine release in the rat striatum in vivo. *Eur J Pharmacol* **369**:175-181.

Bucher ES, Brooks K, Verber MD, Keithley RB, Owesson-White C, Carroll S, Takmakov P, McKinney CJ, Wightman RM (2013) Flexible software platform for fast-scan cyclic voltammetry data acquisition and analysis. *Anal Chem* **85**:10344-10353.

Bucher ES, Fox ME, Kim L, Kirkpatrick DC, Rodeberg NT, Belle AM, Wightman RM (2014) Medullary norepinephrine neurons modulate local oxygen concentrations in the bed nucleus of the stria terminalis. *J Cereb Blood Flow Metab* **34**:1128-1137.

Burke JP, Hablitz JJ (1994) Presynaptic depression of synaptic transmission mediated by activation of metabotropic glutamate receptors in rat neocortex. *J Neurosci* **14**:5120-5130.

Cachope R, Cheer JF (2014) Local control of striatal dopamine release. *Front Behav Neurosci* **8**.

Carmignoto G, Gómez-Gonzalo M (2010) The contribution of astrocyte signalling to neurovascular coupling. *Brain Res Rev* **63**:138-148.

Cartmell J, Schoepp DD (2000) Regulation of neurotransmitter release by metabotropic glutamate receptors. *J Neurochem* **75**:889-907.

Chaigneau E, Tiret P, Lecoq J, Ducros M, Knöpfel T, Charpak S (2007) The relationship between blood flow and neuronal activity in the rodent olfactory bulb. *J Neurosci* **27**:6452-6460.

Cowan CM, Raymond LA (2006) Selective neuronal degeneration in Huntington's disease. *Curr Top Dev Biol* **75**:25-71.

D'Ascenzo M, Fellin T, Terunuma M, Revilla-Sanchez R, Meaney DF, Auberson YP, Moss SJ, Haydon PG (2007) mGluR5 stimulates gliotransmission in the nucleus accumbens. *Proc Natl Acad Sci U S A* **104**:1995-2000.

Faraci FM, Brian J (1994) Nitric oxide and the cerebral circulation. *Stroke* **25**:692-703.

Fergus A, Lee KS (1997) Regulation of cerebral microvessels by glutamatergic mechanisms. *Brain Res* **754**:35-45.

Frick A, Zieglgänsberger W, Dodt H-U (2001) Glutamate receptors form hot spots on apical dendrites of neocortical pyramidal neurons. *J Neurophysiol* **86**:1412-1421.

Hall RD, Lindholm EP (1974) Organization of motor and somatosensory neocortex in the albino rat. *Brain Res* **66**:23-38.

Herr NR, Kile BM, Carelli RM, Wightman RM (2008) Electroosmotic flow and its contribution to iontophoretic delivery. *Anal Chem* **80**:8635-8641.

Hoffmeyer HW, Enager P, Thomsen KJ, Lauritzen MJ (2007) Nonlinear neurovascular coupling in rat sensory cortex by activation of transcallosal fibers. *J Cereb Blood Flow Metab* **27**:575-587.

Homola A, Zoremba N, Šlais K, Kuhlen R, Syková E (2006) Changes in diffusion parameters, energy-related metabolites and glutamate in the rat cortex after transient hypoxia/ischemia. *Neurosci Lett* **404**:137-142.

Huber KM, Roder JC, Bear MF (2001) Chemical induction of mGluR5-and protein synthesis–dependent long-term depression in hippocampal area CA1. *J Neurophysiol* **86**:321-325.

Kirkpatrick DC, Edwards MA, Flowers PA, Wightman RM (2014) Characterization of solute distribution following iontophoresis from a micropipet. *Anal Chem* **86**:9909-9916.

Kirkpatrick DC, Wightman RM (2016) Evaluation of Drug Concentrations Delivered by Microiontophoresis. *Anal Chem*.

Krnjević K, Phillis J (1963) Iontophoretic studies of neurones in the mammalian cerebral cortex. *J Physiol* **165**:274.

Lindauer U, Megow D, Matsuda H, Dirnagl U (1999) Nitric oxide: a modulator, but not a mediator, of neurovascular coupling in rat somatosensory cortex. *Am J Physiol Heart Circ Physiol* **277**:H799-H811.

Lovinger DM (1991) Trans-1-aminocyclopentane-1, 3-dicarboxylic acid (t-ACPD) decreases synaptic excitation in rat striatal slices through a presynaptic action. *Neurosci Lett* **129**:17-21.

Mathiesen C, Caesar K, Akgören N, Lauritzen M (1998) Modification of activity-dependent increases of cerebral blood flow by excitatory synaptic activity and spikes in rat cerebellar cortex. *J Physiol* **512**:555-566.

Meldrum BS (2000) Glutamate as a neurotransmitter in the brain: review of physiology and pathology. *J Nutr* **130**:1007S-1015S.

Mitrano D, Pare JF, Smith Y (2010) Ultrastructural relationships between cortical, thalamic, and amygdala glutamatergic inputs and group I metabotropic glutamate receptors in the rat accumbens. *J Comp Neurol* **518**:1315-1329.

Mitrano DA, Smith Y (2007) Comparative analysis of the subcellular and subsynaptic localization of mGluR1a and mGluR5 metabotropic glutamate receptors in the shell and core of the nucleus accumbens in rat and monkey. *J Comp Neurol* **500**:788-806.

Nielsen AN, Lauritzen M (2001) Coupling and uncoupling of activity-dependent increases of neuronal activity and blood flow in rat somatosensory cortex. *J Physiol* **533**:773-785.

Niswender CM, Conn PJ (2010) Metabotropic glutamate receptors: physiology, pharmacology, and disease. *Annu Rev Pharmacol Toxicol* **50**:295.

Offenhauser N, Thomsen K, Caesar K, Lauritzen M (2005) Activity-induced tissue oxygenation changes in rat cerebellar cortex: interplay of postsynaptic activation and blood flow. *J Physiol* **565**:279-294.

Ogawa S, Lee T-M, Kay AR, Tank DW (1990) Brain magnetic resonance imaging with contrast dependent on blood oxygenation. *Proc Natl Acad Sci U S A* **87**:9868-9872.

Olney JW, Farber NB (1995) Glutamate receptor dysfunction and schizophrenia. *Arch Gen Psychiatry* **52**:998-1007.

Paoletti P, Bellone C, Zhou Q (2013) NMDA receptor subunit diversity: impact on receptor properties, synaptic plasticity and disease. *Nat Rev Neurosci* **14**:383-400.

Petralia R, Wang Y-X, Niedzielski A, Wenthold R (1996) The metabotropic glutamate receptors, mGluR2 and mGluR3, show unique postsynaptic, presynaptic and glial localizations. *Neuroscience* **71**:949-976.

Pettit DL, Wang SS-H, Gee KR, Augustine GJ (1997) Chemical two-photon uncaging: a novel approach to mapping glutamate receptors. *Neuron* **19**:465-471.

Petzold GC, Albeanu DF, Sato TF, Murthy VN (2008) Coupling of neural activity to blood flow in olfactory glomeruli is mediated by astrocytic pathways. *Neuron* **58**:897-910.

Rodeberg NT, Johnson JA, Cameron CM, Saddoris MP, Carelli RM, Wightman RM (2015) Construction of training sets for valid calibration of in vivo cyclic voltammetric data by principal component analysis. *Anal Chem* **87**:11484-11491.

Romano C, Sesma MA, McDonald CT, O'malley K, van den Pol AN, Olney JW (1995) Distribution of metabotropic glutamate receptor mGluR5 immunoreactivity in rat brain. *J Comp Neurol* **355**:455-469.

Sardo P, Ferraro G, Carletti F, D'Agostino S, La Grutta V (2006) The discharge of subthalamic neurons is modulated by inhibiting the nitric oxide synthase in the rat. *Neurosci Lett* **396**:252-256.

Savchenko V, McKanna J, Nikonenko I, Skibo G (2000) Microglia and astrocytes in the adult rat brain: comparative immunocytochemical analysis demonstrates the efficacy of lipocortin 1 immunoreactivity. *Neuroscience* **96**:195-203.

Scott NA, Murphy TH (2012) Hemodynamic responses evoked by neuronal stimulation via channelrhodopsin-2 can be independent of intracortical glutamatergic synaptic transmission. *PLoS One* **7**:e29859.

Sloan H, Austin V, Blamire A, Schnupp JW, Lowe AS, Allers K, Matthews PM, Sibson NR (2010) Regional differences in neurovascular coupling in rat brain as determined by fMRI and electrophysiology. *NeuroImage* **53**:399-411.

Stobart JLL, Lu L, Anderson HD, Mori H, Anderson CM (2013) Astrocyte-induced cortical vasodilation is mediated by D-serine and endothelial nitric oxide synthase. *Proc Natl Acad Sci U S A* **110**:3149-3154.

Surmeier DJ, Ding J, Day M, Wang Z, Shen W (2007) D1 and D2 dopamine-receptor modulation of striatal glutamatergic signaling in striatal medium spiny neurons. *Trends Neurosci* **30**:228-235.

Taber MT, Fibiger HC (1995) Electrical stimulation of the prefrontal cortex increases dopamine release in the nucleus accumbens of the rat: modulation by metabotropic glutamate receptors. *J Neurosci* **15**:3896-3904.

Takmakov P, McKinney CJ, Carelli RM, Wightman RM (2011) Instrumentation for fast-scan cyclic voltammetry combined with electrophysiology for behavioral experiments in freely moving animals. *Rev Sci Instrum* **82**:074302.

Testa C, Standaert D, Young A, Penney J (1994) Metabotropic glutamate receptor mRNA expression in the basal ganglia of the rat. *J Neurosci* **14**:3005-3018.

Traynelis SF, Wollmuth LP, McBain CJ, Menniti FS, Vance KM, Ogden KK, Hansen KB, Yuan H, Myers SJ, Dingledine R (2010) Glutamate receptor ion channels: structure, regulation, and function. *Pharmacol Rev* **62**:405-496.

Verma A, Moghaddam B (1998) Regulation of striatal dopamine release by metabotropic glutamate receptors. *Synapse* **28**:220-226.

Walton L, Boustead N, Carroll S, Wightman RM (2016) Chemically Selective, Local Glutamate Stimulation Using a Multimodal Sensor.

Xi Z-X, Baker DA, Shen H, Carson DS, Kalivas PW (2002) Group II metabotropic glutamate receptors modulate extracellular glutamate in the nucleus accumbens. *J Pharmacol Exp Ther* **300**:162-171.

Zlokovic BV (2011) Neurovascular pathways to neurodegeneration in Alzheimer's disease and other disorders. *Nat Rev Neurosci* **12**:723-738.

Zonta M, Angulo MC, Gobbo S, Rosengarten B, Hossmann K-A, Pozzan T, Carmignoto G (2003) Neuron-to-astrocyte signaling is central to the dynamic control of brain microcirculation. *Nat Neurosci* **6**:43-50.